Travail de fin d'études et stage[BR]- Travail de fin d'études : DEVELOPMENT AND EVALUATION OF THE POWDERS MIX LOW ALLOYED STEEL+SIC FOR LASER POWDER BED FUSION[BR]- Stage d'insertion professionnelle

Auteur : Seidou, Abdul Herrim
Promoteur(s) : Mertens, Anne
Faculté : Faculté des Sciences appliquées
Diplôme : Cours supplémentaires destinés aux étudiants d'échange (Erasmus, ...)
Année académique : 2021-2022
URI/URL : http://hdl.handle.net/2268.2/15724

UNIVERSITÉ DE LIÈGE - UNIVERSITÀ DEGLI STUDI DI PADOVA

FACULTÉ DE SCIENCES APPLIQUÉS-DIPARTIMENTO DI INGEGNERIA INDUSTRIALE

Master Thesis in Materials Engineering

DEVELOPMENT AND EVALUATION OF THE POWDERS MIX LOW ALLOYED STEEL + SIC FOR SELECTIVE LASER MELTING

Promoters: Prof. Anne Mertens

Prof. Irene Calliari (Università di Padova)

Conducted by: ABDUL HERRIM BIO SEIDOU

Academic Year: 2021-2022

Abstract

For this work, the evaluation of the S2 tool steel + Silicon carbide (SiC) powders was provided in terms of the microstructural characterization after a thermal cycle and of the rheological properties of the mixtures. SiC powder was added at 5%, 10%, 15% and 20% in volume to S2 Tool Steel.

The aim of this study is to forecast the microstructures that can be obtained in the Metal Matrix Composites printed through Selective Laser Melting (SLM) after heat treatments, and to determine the proper method to prepare the powders mixture for the feedstock of the SLM.

The microstructures were characterized after Differential Thermal Analysis (DTA) in different conditions. The rheological properties were evaluated on three batches of S2 + 15% (in volume) of SiC powder prepared with different mixing methods which include Ball Milling and Manual mixing. The amount of SiC influence the microstructure obtained, passing from a fully pearlitic matrix for the lowest amount to a fully ferritic matrix with several types of graphite increasing the SiC amount.

The characterization was provided using Optical Microscope (OM), Scanning Electron Microscope (SEM), and chemical analysis such as Energy Dispersive Spectroscopy (EDS) that allow the evaluation and comparison of morphology and composition of the different phases of the different microstructures. For the comparison between the mixing methods, the same tools were used in addition to the technologies for the evaluation of rheological properties such as tap density, cohesive index, granulometry thank to the collaboration with Granutools and Greenmat. This characterization revealed that the manual mixing of S2 powder with pre-milled SiC is the best mixing method between the tried ones.

Acknowledgments

TABLE OF CONTENTS

List of figures

List of tables

1. INTRODUCTION

Additive manufacturing, or three-dimensional (3D) printing, one of the recent technologies of PM, emerged a few decades ago and has been in the research and development spotlight ever since [1]. It offers a unique solution for fabricating complex geometries with high tolerances. In response to the requirements for material properties improvement, metal matrix composites have been developed as a new type of material. These composites have improved the performance of traditional metal materials and prolonged their service life. Through technologies such as Selective Laser Melting (SLM), the field of Metal Matrix Composite (MMCs) is in continuous growth. Since the industrial development of Selective Laser Melting, research has been conducted to identify optimal powder characteristics [2]. Powder controls, together with the melting mechanisms, the microstructure and quality of your finished product.

This Thesis is part of a PhD thesis whose purpose is to use a powder's mixture to fabricate innovative alloys through SLM technology. AISI S2 tool steel has been selected and different percentage of silicon carbide (SiC) powder is added. Preliminary evaluation of this new powders' mixture is necessary to understand its development through SLM.

Differential Thermal Analysis (DTA) was used to study the behaviour of the powders mix in order to have deeper insights about the microstructure formed in equilibrium conditions. The different microstructures obtained, varying the amount of SiC, were characterized and compared by several characterization techniques that include Optical Microscope (OM) and Scanning Electron Microscope (SEM). The effects of silicon amount and cooling rate on microstructure have been investigated. Furthermore, SLM technology has strict demand to its powder materials which is needed to be spread evenly and conducted laser sintering layer by layer. Therefore, the uniformity and flatness of powder bed are the basic conditions for processing [3]. The powder preparation method for SLM is a critical point to ensure a good SLM processing. Therefore, several mixing methods such as ball milling and manual mixing were performed and analysed in order to determine the best method for the preparation of the powder feedstock for SLM technology.

2. STATE OF THE ART

2.1 Powder Metallurgy

Powder Metallurgy (PM) is a method of manufacturing in continuous and rapid evolution that embraces most metallic and alloy materials. The annual worldwide metal powder production reach over one million tonnes, and the European market has an annual turnover of at least six billion euros [4].

In the 1920s, Schroter and Skaupy, the first innovators of PM, started with the combination of tungsten carbide (WC) with iron-base alloys. About a decade later, a manufacture of sintered materials with controlled porosity began [5]. During the second World War, production through PM increased, involving a wide range of ferrous and non-ferrous materials. In that period, in Germany, the PM was used for firearms production, adapting compacting techniques known for ceramic components to metallic powders. After the war, due to the higher requirements for properties and performances, mostly for the automotive applications, special alloyed grades such as Ni-Cu-Mo steels obtained by the diffusion and bonding of the powders were introduced [6]. This expansion was due mainly to the rapidity and the affordability of this process. The application varies from oxygen getters in food packaging to the advanced application like the nickel-cobalt superalloys gas turbine discs [7].

The powder manufacturing techniques make a consistent growth during the last years in terms of types of powders that can be produced. Nowadays, it is possible to produce a wider type of powders and to have a better control of the microstructure of the alloy's particles [8]. In many cases, the properties of a material manufactured using PM technology surpasses an adequate material produced using a different technology [5]. What makes PM innovative is the capacity to process dense alloys with high performance properties such as strength and wear resistance, with a uniform microstructure. Compared to casting, stamping, or machining, PM is more competitive. One of the reasons is that it satisfies the high operating temperatures that exceed the capabilities of the die casting alloys and eliminate the finishing operations. Moreover, PM reaches a greater precision, and it avoids the common defects that can be obtained with other processes such as shrinkage, bow holes and inclusions [8].

The conventional PM processes include Metal Injection Moulding (MIM), Powder Forging, i.e., Hot Isostatic Pressing (HIP). These processes are press and sinter-based methods to obtain semi-dense and full dense components [9].The newest PM production route is Additive Manufacturing, earlier

also known as "rapid prototyping", i.e., the production of complex shaped specimens from powders by local joining.

2.1.1 Powder production

The significant manufacturing methods may be classed as chemical methods, physical methods, and mechanical methods. The choice of the suitable method depends on the type of application of the final product, and of the desired properties. The main manufacturing atomisation processes are Gas Atomisation (GA), Induction Melted Bar Atomisation (EIGA), Plasma Atomized Wire (PAW) and Plasma Rotating Electrode Atomisation (PREP). These methods have advantages and disadvantages that lead the choice of the appropriate process. Most of these are reported in Table 1. Other methods include atomisation and granulation processes; chemical methods such as reduction and electrochemical methods and mechanical crushing and grinding [7]. More details are given on the atomisation processes. The atomisation is an integral element of the spray-drying process. It is a method by which a liquid or slurry is converted to a dry powder by atomisation into a flowing stream of hot gas. Air is generally the heated gas, although if the liquid contains flammable solvents such as ethanol or toxic solvents such as methylene chloride, nitrogen, an inert gas, is generally used as the drying gas [10].

Table 1: Advantages and disadvantages of the leading metal powder manufacturing methods for metal AM [7]

Process	Advantages	Disadvantages
Gas Atomisation (GA)	• Excellent metallurgical quality • High powder flow rates • Wide selection of alloys • New and modified alloys can easily be made • Scalable technology: very high volumes available and can easily support AM growth • Large supply base • Relatively low cost, especially when AM increases quantities	• Variability in powder properties between suppliers • Large number of suppliers and atomising technologies can be confusing • Reactive and high melting point alloys not available • Few companies currently atomising titanium
Induction Melted Bar Atomisation (EIGA)	• Excellent metallurgical quality • High flow rates • Reactive and high melting point alloys can be made • Titanium alloys available • High production rates, but restricted by yield considerations	• Limited supply base - but growing • Only alloys available as bar can be made • High cost
Plasma Atomised Wire Process (PAW)	• Excellent metallurgical quality • Very high flow rates – near perfect spheres • Reactive and high melting point alloys can be made • Titanium alloys available	• Limited supply base: only a few suppliers, and new patents may lock out additional suppliers • Only alloys available as wire can be made • High cost
Plasma Rotating Electrode Process (PREP)	• Excellent metallurgical quality • Very high flow rates – perfect spheres • Reactive and high melting point alloys can be made • Titanium alloys available	• Limited supply base but growing • High quality bar needed as starting material • High cost
Water Atomisation (WA)	• Low cost • Scalable atomising technology	• Metallurgical quality lower than gas atomisation • Powder not natively spherical • Not yet established for powder bed applications

- Gas Atomisation

The Gas Atomisation (GA) process consists into the dispersion of liquid metal by high-velocity jet air, nitrogen, argon or helium. The commercial production includes materials such as powders of copper, copper alloys, aluminium and its alloys, magnesium, zinc, titanium and alloys, nickel-base alloys, cobalt-base alloys, lead, tin, solder, precious metals, refractory metals, and beryllium [11].

The particles size depends on the gas-to-metal ratio, an important factor to control the process. The pressure of the gas is increased above 0.1 MPa to reach sonic velocity. This pressure is extremely low compared to other processes like water atomisation, where a pressure above 40 MPa is required. To produce copper, brass and zinc powders, air atomisation is used. In contrast, inert gas is used for

processes that require a low content of oxygen or atomizing metals that are highly reactive such as superalloys [11].

Professor Hall, founder of the Metals Disintegrating Co, was the first worker in this field. In the late 1920s, he patented a close-coupled atomizer for aluminium atomisation, whose design is still in use with several improvements. The first GA process was performed with the steam done by Marriott of Huddersfield in 1872. The process consists in letting a metal stream fall onto a horizontal gas jet to produce zinc powders. VAMI developed a similar unit that delivers the atomizing gas through an annular orifice around the nozzle at the converging angle (Figure 1). A sort of ejection effect is created by the gas flow at the tip of the nozzle that draws the molten metal into the nozzle.
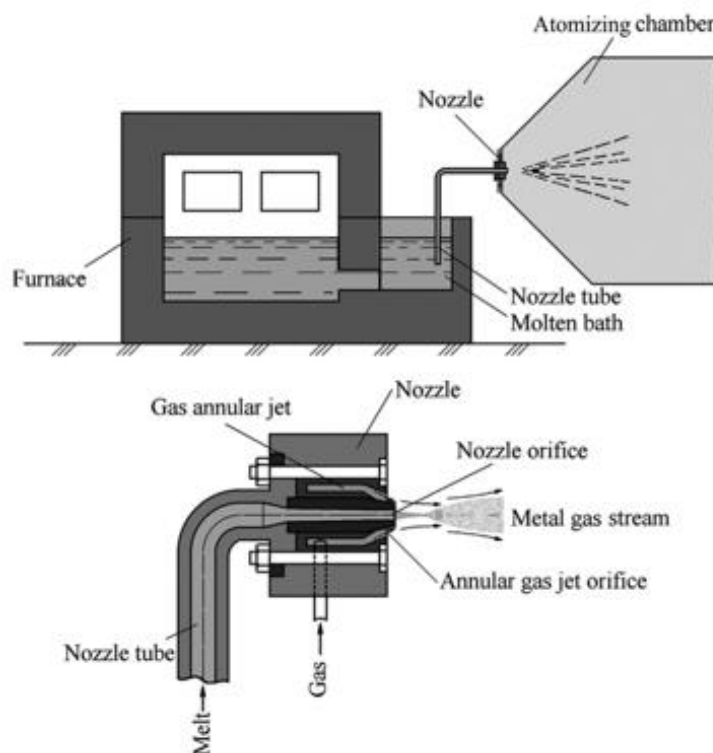
Figure 1: VAMI ejection nozzle design with horizontal molten metal stream [11]

Some parameters such as the size of the air gap, the temperature, and the pressure of the gas determine the amount of gas delivered, while the rate of metal flow and powder particle size is determined by the aspirating force, the nozzle metal orifice diameter and the vertical distance between the nozzle and the molten metal [11].

The idea behind the design is to contact the liquid metal stream with the gas at or close to the gas jet exit plane where there are the highest jet velocities. That is important to reach an efficient break-up of the liquid, resulting in finer powders. This method is preferred for aluminium and other low melting point metals. The operation can be done vertically upward or downward, or in the

4

horizontal position. The design should also guarantee the non-freezing of the metal by the gas jet, which can lead to solidification at the nozzle tip. The gas atomizer designs are classified as free fall, confined or closed nozzles, and internal mixing (Figure 2). The closed nozzle designs are also called close-coupled nozzle designs [11].
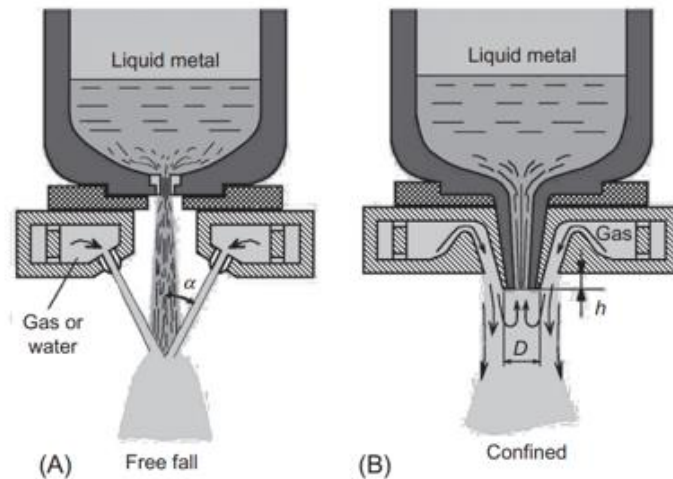
Figure 2: Atomizer designs of two types: (A)free-fall design (gas or water) and (B) confined-nozzle design (only gas). Design parameters: α, angle formed by free-falling molten metal and atomizing medium jet; D, diameter of confined molten metal nozzle end; h, protrusion length of metal nozzle[11]

Considering the shape, gas atomized particles are relatively spherical but may exhibit any of the feature (Figure 3). Satellited particles are a problem, not only for flowability and packing, but because the satellite particles are so small and can become an airborne health and safety risk. More spherical particles can be produced by plasma atomisation or the Plasma Rotating Electrode Process (PREP), but at a higher price [12].
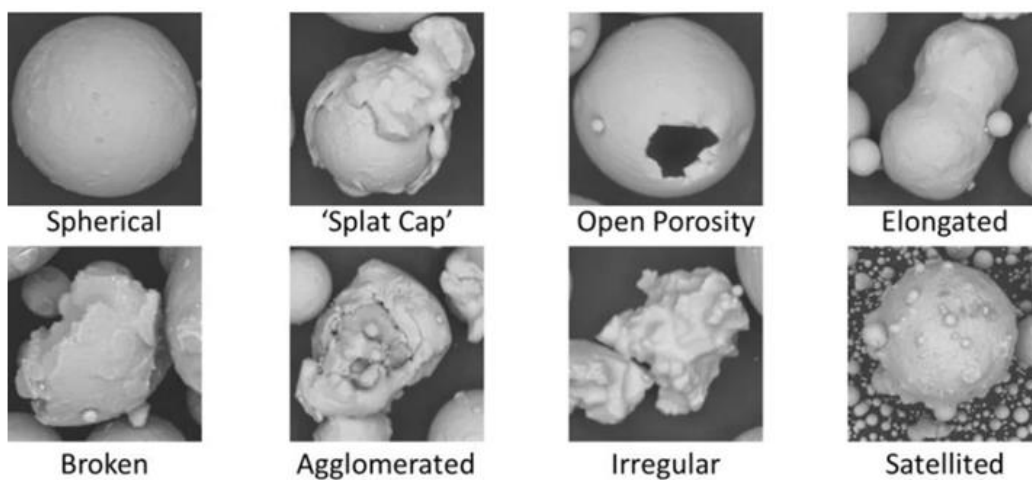
Figure 3: Different shapes of particles that may results from GA

- Water Atomisation

The process of Water Atomisation (WA) consists into an impingement of a falling stream of molten metal with jets of water which induces the solidification of the metal into granules (size over 1mm) or powders (under 1mm). The range of particles size obtained by atomisation processes compared to the other methods can be resumed as shown in Figure 4.
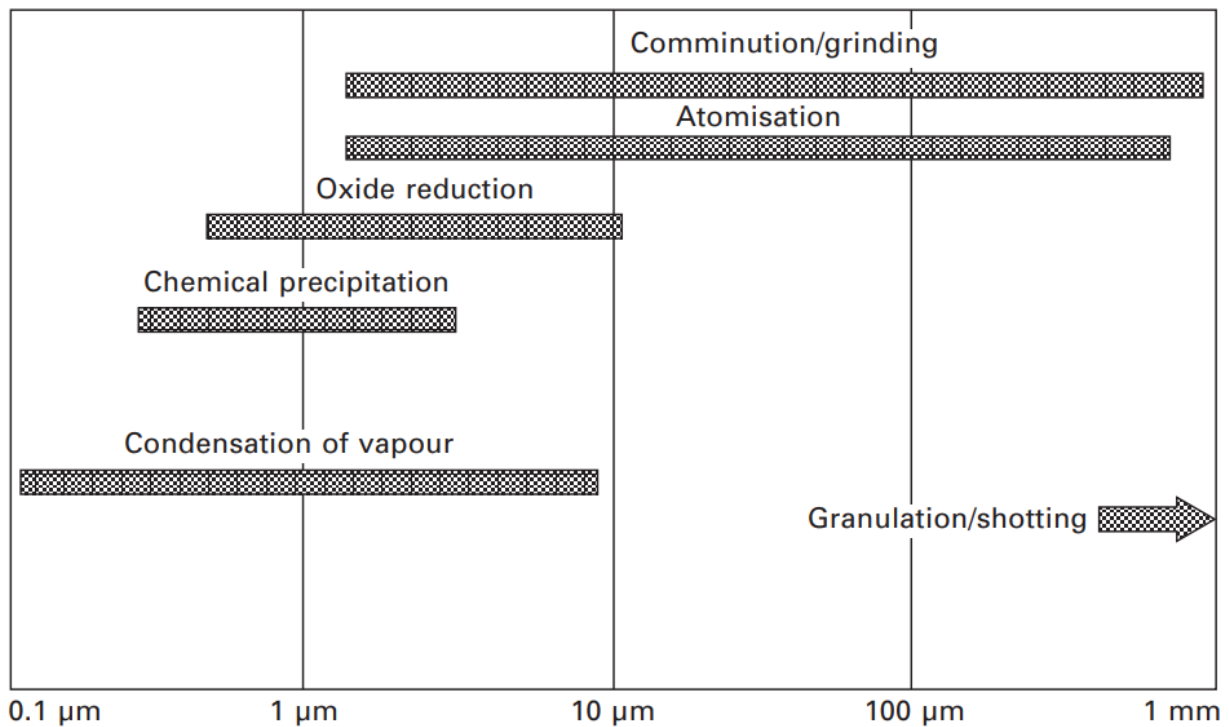
Figure 4: Approximate size ranges produced by different techniques

WA is less expensive than other methods of atomisation, but the main limitation of this process is powder purity, especially for metals and alloys inclined to oxidation. However, owing to the higher cooling rate of the melt by WA, the average thickness of surface oxides, which may affect the particles shape, is similar to GA powders. Moreover, the morphology of the particles obtained by WA is more irregular in shape and less spherical compared to GA.

The commercial production using WA includes copper, copper alloys, nickel-base alloys, and zinc powders [13].
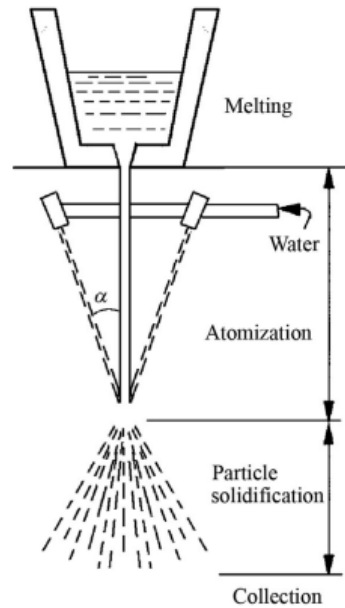
Figure 5: Stages in water atomisation[11]

WA system is composed by a melting unit, a tundish, an atomizing chamber, a water pumping and recycling system, and the dewatering and drying units. The pressure of the water jets is between 5-20 MPa or 50-150 MPa depending on the size of the particle to produce. Usually, the powders produced by WA are used in injection moulding process, as binders in diamond tools, for sintering bearings, paints, coatings, and pastes. The variables associated to the atomisation stages shown in Figure 5 are related to the design of the atomizer such as nozzle diameter, jet geometry and apex angle, to the operating conditions such as metal stream length, water pressure and to the material properties such as density, surface tension of the melt and viscosity of the melt [11].

- Mechanical alloying by Ball milling

Mechanical alloying (MA) is the generic term for solid-state powder processing in high energy mills that involves repeated cold welding, fracturing and rewelding. The process consists in milling together mixtures of powders of different metals or alloys/compounds. Mechanical alloying was originally developed about 70 years ago to produce oxide-dispersion-strengthened Ni/Fe-based superalloys for aerospace and high temperature applications [14]. MA is a process referred to powders of pure metals A and B that are milled together to produce a solid solution, intermetallic or amorphous phase to obtain a homogeneous alloy (Figure 6) [15]. The characteristics of MA are shown in Table 2 [14].
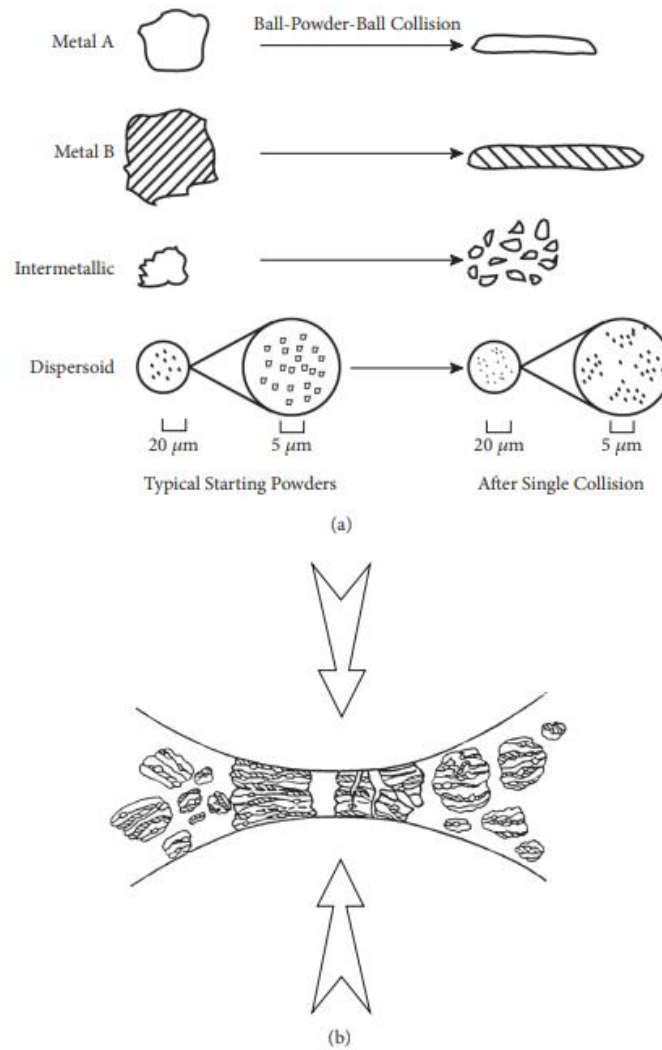
Figure 6: (a). Deformation characteristics of starting powders in mechanical alloying (MA). The ductile metal powder (metal A and B) gets flattened, while the brittle intermetallic and dispersoid particles get fragmented into smaller particles. (b). Ball-powder-ball collision of powder mixture during mechanical alloying [14]

If the process takes place without material transfer for the homogenization, the process is called Mechanical Milling (MM). It includes processes that reduce the particle or the grain size and increase the surface area. The phenomena that take place depend on the nature of the materials. Brittle materials are more responsive to disintegration, while ductile materials are subjected to cold welding. To break down brittle materials, the process takes place in ball mills where the material is stressed by the impact, compression and shearing of the hard balls to be finally disintegrated into smaller particles. Most metals produced by milling have an average particle size over 100 μm [15].

(1)	Production of fine dispersion of second phase (usually oxide) particles
(2)	Extension of solid solubility limits
(3)	Refinement of grain sizes down to nanometer range
(4)	Synthesis of novel crystalline and quasicrystalline phases
(5)	Development of amorphous (glassy) phases
(6)	Disordering of ordered intermetallics
(7)	Possibility of alloying of difficult to alloy elements/metals
(8)	Inducement of chemical (displacement) reactions at low temperatures for (a) Mineral and Waste processing, (b) Metals refining, (c) Combustion reactions, and (d) Production of discrete ultrafine particles
(9)	Scaleable process

2.1.2 Additive Manufacturing

Additive Manufacturing (AM), also known as 3D printing, from ASTM 52900-15, is a process of joining materials to make objects from 3D model data, usually layer upon layer, as opposed to subtractive manufacturing methodologies [16]. AM attracts the attention of many, due to the benefits it brings. In AM, half of the applications are dedicated to make prototypes. The last years shows an increase of the quality of the parts produced, even in term of complexity of the part, freedom in design and functions of the end-use products, and number of materials printed through AM such as polymers, metals, concrete or in future human tissues for aircraft, medical implants, architecture, and automotives [17]. The advantages of AM derive from its high flexibility due to the product produced directly from a CAD model without the need of tooling [8]. Recently, lot of studies focus on the impact on sustainability, considering a life cycle analysis [[18][19][20][21]]. This life cycle analysis considers all the life cycle's phases from the design to the use and end of life [22].

Until the early 1990s, the AM processes did not consider the fabrication of metals. The first attempts used a metal powder as a feedstock and a CO_2 laser for consolidation. These first trials highlight problems related to the full densification and consolidation of the metal powders making the products unsuitable for industrial use. The Fraunhofer Institute ILT, in Aachen, and Hans Langer, the founder of Electro Optical Systems were the pioneers of this process. The first one becomes the forerunner of the Selective Laser Melting (SLM) solutions and the Renishaw Additive Manufacturing. The second one brought a metal system to market in 1994 [6].

AM processes usually operates with "fixed" parameters for a specific application, with current machines offering little opportunity for any form of responsive control. As consequence, an

inconsistent input material property will translate directly into inconsistent finished component properties. Defects in the end part such as pores, cracks, inclusions, residual stresses and suboptimal surface roughness, as well as compromising throughput can be generated by a poor quality of powders. The correlations between material properties, processing performance and end component properties are essential to select the best powder for an application and to ensure the consistency of that powder from build-to-build and layer-to-layer, as well as through recycling [12].

2.1.2.1 Additive Manufacturing Technologies

The AM processes can be classified by the energy source used, the type of raw material such as powder, wire, sheets or liquids, and by the way the particles are joined such as bonding or melting [6]. Some specifications and equipment are summarized in Table 3. The metal AM technologies that use powders as raw material can be divided in powder bed and powder fed technologies as shown in Figure 7.

The powder-bed systems, also known as laser melting processes, group Selective Laser Melting (SLM), Direct Laser Melting (DLM) and Direct Metal Laser Sintering (DMLS). These systems consist into the application of a powder layer that is consolidated by melting the particles in the case of direct methods, or by bonding them together in indirect methods. The following layer is formed using the same process until the fully built part is obtained, embedded in the powder bed. Powder-bed technologies are suitable for building high precision and more complex parts such as hollow cooling passages not obtainable with powder-fed techniques. In direct methods, laser or electron beam selectively melt the powder layer. The biggest difference between laser and electron beam usage is the necessity of vacuum chamber (i.e., 10^5 hPa or lower in EBM) [6].

The indirect technologies produce a green part by printing a binder on a powder bed or by curing the binder locally that will be debinded and sintered, and sometimes infiltrated to obtain a completely dense material. The productivity of 3D printing is higher than laser or electron beam melting. In addition, the process takes place in room temperature and does not require support structures due to the support already offered by the powder bed during the printing [6].
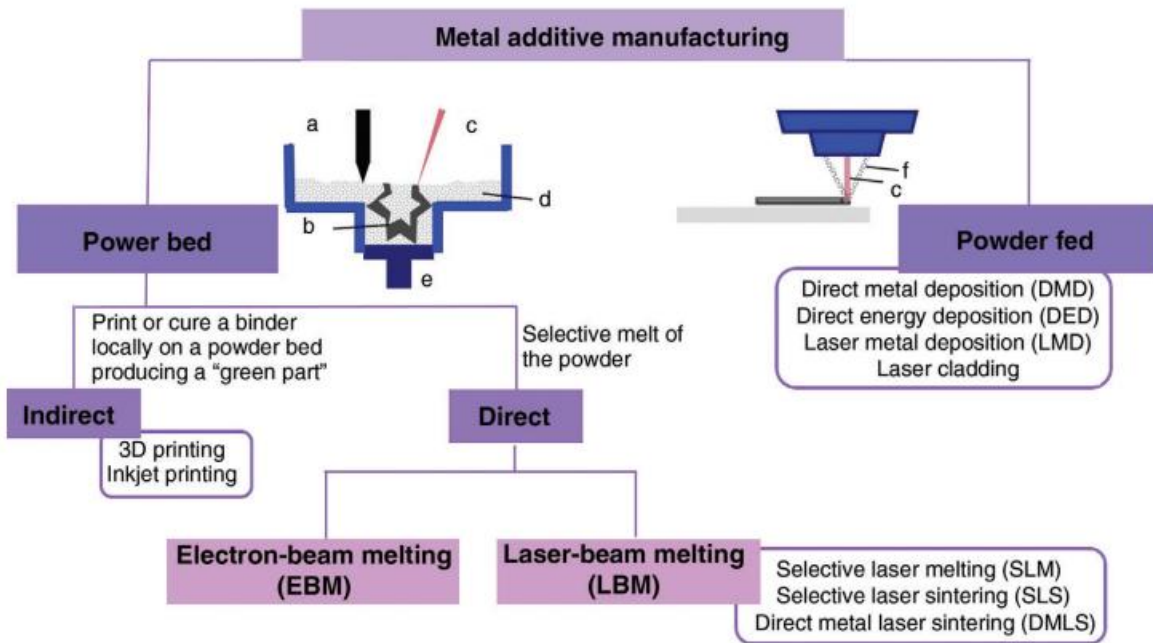
Figure 7: Additive Manufacturing technologies: a) Leveling system; b) Part; c) Beam; d) Powder bed; e) Platform; f) Powder [6]

The powder-fed systems use the same feedstock but differ in the way the material is printed. The requirements of the end user induce the choice of the right machine. With powder-fed systems, the powders flow through the nozzle and is melted with a beam exactly on the specified surface of the treated part where it solidifies. Some advantages of this system are the higher productivity due the high deposition rates and the ability to produce larger parts than with powder-bed systems [23].

The wire-fed systems use material in form of a wire. The energy source can either be an electron beam, a laser or even a plasma arc. The process consists in a single-track deposition followed by different sequentially passes until the 3D structure is built. This technique allows a high deposition rate of material, and it is well suited for the building of large volumes [23].

Table 3: Representative AM equipment sources and specifications [16]

System	Process	Build volume (mm)	Energy source
Powder bed			
ARCAM (A2)(a)	EBM	200 × 200 × 350	7 kW electron beam
EOS (M280)(b)	DMLS	250 × 250 × 325	200-400 W Yb-fiber laser
Concept laser cusing (M3)(b)	SLM	300 × 350 × 300	200 W fiber laser
MTT (SLM 250)(b)	SLM	250 × 250 × 300	100-400 W Yb-fiber laser
Phenix system group (PXL)(c)	SLM	250 × 250 × 300	500 W fiber laser
Renishaw (AM 250)(d)	SLM	245 × 245 × 360	200 or 400 W laser
Realizer (SLM 250)(b)	SLM	250 × 250 × 220	100, 200, or 400 W laser
Matsuura (Lumex Advanced 25)(e)	SLM	250 × 250 diameter	400 W Yb fiber laser; hybrid additive/subtractive system
Powder feed			
Optomec (LENS 850-R)(f)	LENS	900 × 1500 × 900	1 or 2 kW IPG fiber laser
POM DMD (66R)(f)	DMD	3,200° × 3°,670° × 360°	1-5 kW fiber diode or disk laser
Accufusion laser consolidation(g)	LC	1,000 × 1,000 × 1,000	Nd:YAG laser
Irepa laser (LF 6000)(c)	LD		Laser cladding
Trumpf(b)	LD	600 × 1,000 long	
Huffman (HC-205)(f)	LD		CO_2 laser clading
Wire feed			
Sciaky (NG1) EBFFF(f)	EBDM	762 × 483 × 508	>40 kW @ 60 kV welder
MER plasma transferred arc selected FFF(f)	PTAS FFF	610 × 610 × 5,182	Plasma transferred arc using 350A DC power supplies
Honeywell ion fusion formation(f)	IFF		Plasma arc-based welding

Country of Manufacturer: (a) Sweden, (b) Germany, (c) France, (d) United Kingdom, (e) Japan, (f) United States, and (g) Canada

- Selective Laser Melting (SLM)

During the layer processing in SLM, the powder bed drops while the powder feeder is spread with a layer of powder at the same time. To obtain a 3D net shape metal part, the process is repeated to gradually stack. The parts that can be obtain can have a macroscopic complex structures and unique microstructures [24].
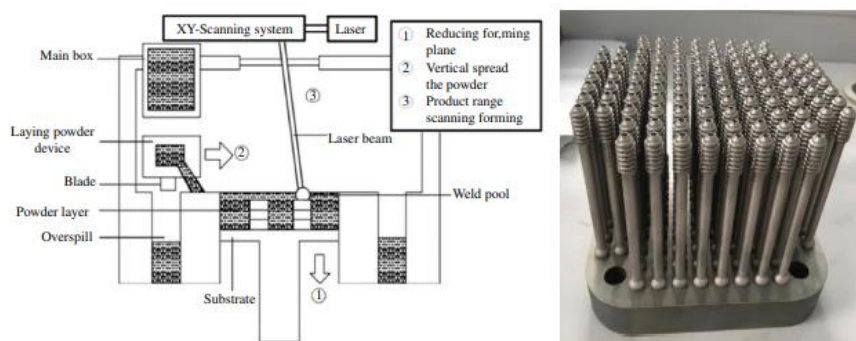
Figure 8: SLM schematic and parts [25]

Compared to conventional casting and forging processes, the molten pool has an extremely high cooling rate about 10^3-10^6 K/s. Thus, the solidification process is in non-equilibrium and is caused by the rapid cooling that facilitates the grain refinement and may form new sub crystal or

amorphous phases. Another characteristic of the SLM process is the gradient of temperature that forms in vertical and horizontal directions (horizontal gradient is negligible compared to vertical gradient). The microstructure of SLM depends on the laser power, scanning speed, scanning hatch distance, layer thickness, scanning strategy, and heat treatment process. The parts formed through SLM process are not without defects such as porosities, cracks, and internal stresses [24].

The powders used for SLM have a range of characteristics (Table 4) such as the particle size, powder type. An ultrafine powder around 30μm of particle size is used as raw material and is selectively melt layer by layer according to the contour data. Fluidity, laser absorption rate of the metal and oxygen content are also important characteristics [26].

Table 4: Types and characteristics of metal powders used in SLM technology [26]

Powder type	Iron-based (316L, 420, M2), titanium and titanium-based (Ti6Al4V, TiAl), aluminum-based (AlSi, AlCu, AlZn), nickel-based (Inconel 625, 718), copper, etc.
Preparation method	Water atomization, gas atomization, rotating electrode method
Particle size distribution/μm	20–50
Oxygen content/ppm	≤1000

- Recycled powders used in Selective Laser Melting

The advantages brought by reusing the powders in SLM are related to the cost of the entire process and the sustainability of the resources. The manufacturing cost is reduced, and the sustainability is promoted. The research in this area is limited, and the effect of the powder characteristics and the final part properties such as flowability, Particle Size Distribution (PSD), chemical composition, microstructure evolution, microhardness, and tensile properties are being studied. An advantage of the powder-bed AM processes is that the powder can be reused. As a result, the powder reuse times that are permitted carry a significant influence on the average cost of the additively manufactured products [27].

Researchers like Seyda et al. [28] try to understand the effect of reuse cycles on Ti-6Al-4V powders, finding that after 12 cycles, the powders tend to become coarser and the flowability increases, while Cordova et al. [29] explored different powders such as Inconel 718, AlSi10Mg, scalmalloy and the effect on the forming process. All these studies show a clear difference between the virgin and used state revealed by the characterization [29]. A study on the characteristics of Ti-6Al-4V powder in the AM process by SEBM was performed, resulting on an increase of the oxygen

content, a coarsening of the particles shape, an increase of the flowability and mechanical properties increasing the reuse time. The research concludes the absence of undesired influence of reused powder on the AM process of Ti-6Al-4V [30].

2.1.2.2 Powder characterization

AM is sensitive to powder variability when applying fine layers in a uniform manner, and to reach it, a high degree of consistency and repeatability in the feedstock is requested. Particle size is often used as a critical quality attribute (CQA), but this is not sufficient to fully qualify a feedstock. Indeed, it is inadequate to suggest that any parameter from a single test can fully describe a powder's characteristics [31]. The properties of the powders, which include apparent density, tap density, angle of repose, flow rate, compressibility, and green strength, depend on the granulometric composition, particle shape, particle morphology, specific surface, moisture content. The combination of the technological parameters with the physical properties plays a significant role in the evaluation of the behaviour of the powders during processing accomplished by their consolidation. The properties of powders are evaluated using standard monitoring methods based on the International Standards Organization (ISO), to which some refined specifications can be added [32]. The chemical composition and the structure are determined using the methods in Table 5.

Table 5: Powder properties and methods of measuring them [4]

Particle size and size distribution	Sieve analysis: Permeability: Sedimentation electrical resistance; Light obscuration; Light scattering; Microscopy; Surface area.
Particle shape [external]	SEM; Shape parameters; Morphological analysis; Fractals.
Particle shape [external and internal]	Stereology; Mercury Porosimetry; Gas absorption.
Particle density	Pycnometry; Mercury porosimetry.
Specific surface area	Gas absorption; Permeametry.
Surface chemistry	X-ray photoelectron spectroscopy (ESCA); Auger electron spectroscopy; Secondary ion mass spectroscopy; Ion scattering spectroscopy.
Alloy phases and phase distribution	Optical metallography; Stereology; Electron microscopy; EDAX; X-ray diffraction.
Quality of mixing [segregation]	Macroregion:Variability coefficient (by chem.anal.); Microregion: Variability coefficient (2nd comp. >5%); Homogeneity coefficient (2nd comp. <5%); by metallography

- Particle size and shape

A knowledge of the problems of powder movement plays an important part in powder processing. The classification process is used to determine particle size distribution or to separate certain particle sizes from a distribution. There are many powder classification techniques based on the movement of the suspended particles in a fluid under the action of a force field, which is created by gravitational, centrifugal, or inertial forces, in addition to sieve analysis and direct counting and sizing by microscopy. The fluid is usually air or water. The classifiers may be distinguished depending on the stream direction: counterflow equilibrium and crossflow separation [8].

The percentage of fractions obtained analysing the granulometric composition is conveniently presented in the form of histogram. Particle sizes are plotted (at a uniform or non-uniform scale) as abscissas and relative fraction contents, that is, percentages of each fraction, as ordinates. In practice, the ranges of separate fractions are usually taken to be nonequal without a strict adherence to this condition. Consequently, while constructing the histograms of weight distribution throughout particle sizes, the relative contents of fractions plotted on the ordinate are established by dividing the weight percentage of each fraction by its range. The histogram gives a presentation of powder disperse composition, and the correctness of the presentation increases with narrowing the range limits. This is caused by technical conditions of analysing as well as by the range of fractions that should be increased with an increase of particle size to obtain a complete characterization of the powders [8]. The polymodal distribution (Figure 9) consists in two or more narrow bands of particle sizes, each with a maximum, with virtually no particles having size between two bands. The broad band distribution represents a uniform concentration of particle sizes over a rather broad size interval with no particles with size outside the range. the last distribution type is the irregular one, and it represents a continuous and finite variation of the particle sizes within a broad range [8].

The dimensionality and the contour surface characterize the powder that can be very irregular in size and shape. The presence of porosity in particles differ these particles from irregular ones. That is the reason why the particle size distribution is used to accurately describe the powders, more than an average value or even maximum or minimum values of size. The different morphologies and the common process to obtain them are summarized in Figure 10 [8]. The powder morphology is important to ensure a smooth flow and high packing density on the build platform and can influence the recyclability of the powders [29].
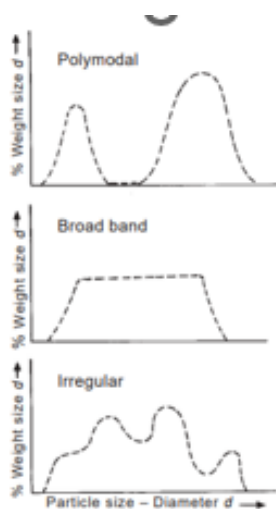
Figure 9: Schematic illustrations of some realistic particle size distributions [8]
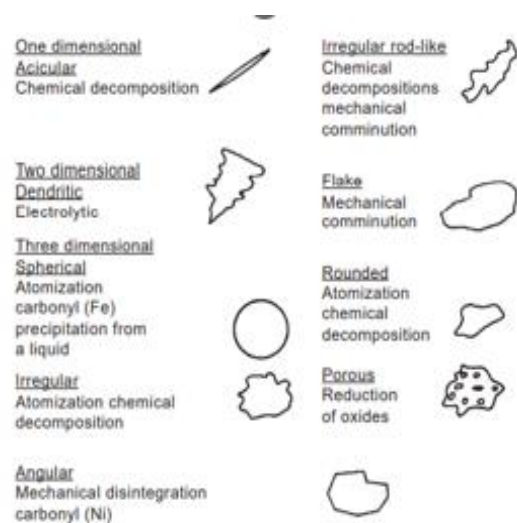
Figure 10: System of particles shape characterization [8]

A spherical particle may appear smooth, but on a closer examination at high magnifications, the surface may consist of many protuberances. Atomized metal powders have finer degree of surface roughness than reduced metal powders, which are of rounded type rather than sharp and irregular. Scanning electron microscope (SEM) is a powerful tool for examining surface topography, and it also allows the examination of the contamination on powders surface and the agglomeration of fine particles. The surface topography influences the frictional forces of the particles, which can be correlated to the flowability, settling and compaction properties of the bulk. In particular, the roughness of the particles surface affects the particle-to-particle contact during sintering and the chemical reactivity of the powder. [7].

To determine if the powders can be reused, the first step is to check the PSD of the powders and determine if it is in the correct range to be used for SLM (15–63 µm). Typically, reuse is associated with an increase of the PSD that could impact the flow behaviour [28].

- Bulk density (Apparent and Tap Density)

The term powder bulk density includes its apparent density and top density that differ from one another in their effect on the compressibility of powder samples.

The apparent density of metal powder is the weight of a unit volume of loose powder expressed in g/cm^3. The apparent density affects and determines the actual volume allocated to a mass of loose powder. Apparent density of a metal powder strongly depends on the particle size and, usually, decreases with decreasing the particle size. It decreases increasing the irregularity of the particle shape and surface roughness. In the case of powders with a wide range of particle sizes, the

16

apparent density increases because the space between coarse particles is filled with smaller particles. Apparent density is determined by the Hall flowmeter shown in Figure 11, where a container of known volume (25 ml) is filled by flowing metal powder through a Hall funnel [7].
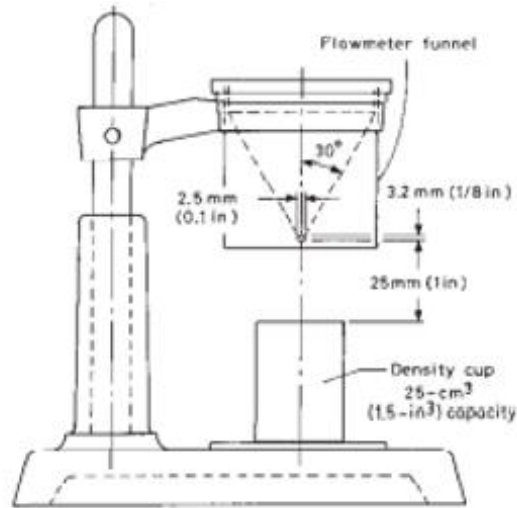
Figure 11: Hall flowmeter [7]

The method for the determination of tap density, which is defined as the density of a powder when the volume container is tapped or vibrated under specified conditions, is established by ISO 3953. The greatest variation of density occurs in the first tapping period before eventually becomes constant. The final stable density is the value reported as the tap density, and is a function of particle size distribution, particle shape, and surface roughness. The final density is always higher than the free-flow apparent density. Usually, the lower the apparent density, the higher the percentage increase in density on tapping [7].

A powder bed is characterized by an equilibrium between adhesion/cohesion of the particles packed and the gravitational forces. A minor shaking of the powder bed can mobilize the particles so that when the shaking stops, the particles will have a new arrangement characterized by a more packed particles that occupy a smaller volume than the initial one. The volume variation will result in changing the density of the powder. More is the packing of the powder and higher will be its resistance to flow, as more driving force is necessary to produce flow compared to loosely packed particles of the same powder [32].

The density obtained by dividing the mass of a powder (m) by the initial volume of the undisturbed powder bed (V_0) will produce the initial bulk density (ρ_0), also known as fluff or poured density. Diving the mass by the volume of the shaken or tapped powder bed (V_f) gives the final bulk density (ρ_n), also known as tapped or consolidated density [32].

Tapped density is an indicator of the flow properties of powders and is used to calculate Hausner ratio and Carr's index. Hausner's ratio is the ratio of the poured density to the tapped density. Hausner showed that free-flowing powders (with low interparticular friction) had a ratio of less than 1.2 compared to more cohesive powders, and thus less free flowing, had higher values (>1.5). By this he demonstrated that this ratio is a predictive of powder flow as it is related to the interparticulate [32].

It is worth noting the dependence of the values obtained for the compressibility index (Carr's index) and Hausner ratio on the experimental conditions such as cylinder diameter, number of times the powder was tapped, and the mass of the material used. Carr's index is calculated according to Equation 1 and it is a direct measure of the tendency of arch or bridge formation and its strength. It also represents an indirect measure of the flow properties of the powder. A free-flowing powder would have an index value less than 15, while a poorly flowing powder is characterized by an index value higher than 32. Bulk density affects the value of the compressibility index and factors such as particle size and shape, surface area and moisture content can influence its value, thus it can be used as a way to assess these properties [32].

Equation 1 $$\%Compressibility\ (Carr's\ index) = \frac{\rho_n - \rho_0}{\rho_n}\ x\ 100$$

The final density and porosity of a manufactured part is known to be affected by process parameters such as laser power, scanning rate and hatch space. For this reason, the final analysis in the decision diagram is the analysis of the tap density to determine if the powders can be reused. It is important that the packing ratio (g) is at least 0.6 (ρ_{tap}/ρ_{true}) to ensure a homogeneous powder bed and minimal porosity [28].

- Flow Rate

Flow rate is defined as the time required for a powder sample of a standard weight of 50 g to flow gravitationally under atmospheric conditions through the Hall funnel. ISO 4490 establishes the method of flow rate determination of metallic powders through the Hall funnel. A non-free-flowing powder is classified as a powder that does not flow through the 2.5mm orifice of a Hall funnel. Fine powders do not flow through a small orifice. That is caused by the drastic increase in the specific surface area as the size becomes exceedingly small. For a given metal powder, increasing the apparent density, the flow time decreases. In fact, when a fine size powder is mixed in a coarse powder, because of the increase in the apparent density, the flow time is decreased irrespective of whether the particles was irregular or spherical. However, in case of excessive amount of frictional surface area, obtainable with irregular powder additions, an amount is reached for which no flow behaviour is observed [7].

- Segregation of particles

A uniformity of the mixture is very important in achieving high-quality AM. The segregation results in the heterogeneity of the particle size distribution as well as of the physical-chemical properties when a particulate material is represented by both a polydisperse powder and a mixture of powders differing in these properties. Three phenomena have been identified as the primary causes of most segregation problems in metallic powders.

The first is the trajectory effect that happens while pouring the powder by the chute onto the pile, and consequently separate particles in size. The frictional drag on particles moving on a pile surface is higher for finer particles than for coarser ones. This results in a concentration of finer particles nearer to the end of the chute while coarser particles come to rest at a much greater distance to the base of the pile. Usually, particles greater than about 100µm in diameter are most subject to trajectory effect segregation. If most of the particles are smaller than 100mm, the segregation by fluidization and particle entrainment is more probable [31].
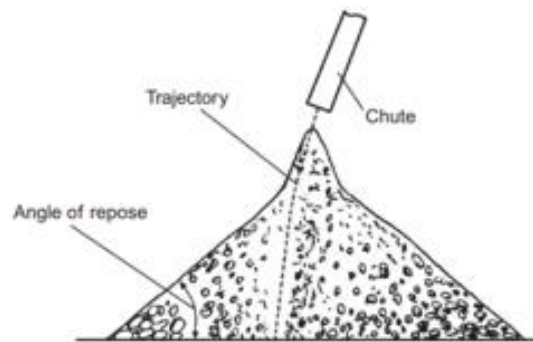
Figure 12: Trajectory effect segregation of particles [19]

The second phenomenon is the screening model, also called sifting phenomenon, and occurs when finer particles move through a matrix of coarser particles. The screening effect occurs in PM processes which are connected with filling of different volumes. In these processes, an impingement effect is also revealed when, under the impact of falling coarser particles, the pile of finer particles becomes denser and causes the slope angle of the upper part of the pile to become higher than the angle of repose [31].

The last phenomenon is the fluidization that is the ability of fine particles to remain in suspension for a long time whereas coarser particles settle first. As consequence, a vertical segregation of particles within the powder layer occurs. In the case where the powder is segregated by air entrainment, fine particles is located close to the top of the bottom-poured container. Air

currents can carry the airborne fine and light particles away from a fill point to certain parts of a bin, such as toward vents and dust collectors [31].

The characteristics of the powders have an influence on the Additive Manufacturing processes. These effects are summarized on the Table 6.

Table 6: Powder characteristics and their influence on the Additive Manufacturing process [20]

Powder Characteristics	Description	Influence on Process and Product
Particle size distribution	Maximum particle size determines optimal powder layer thickness [32] Balanced particle size distribution has a positive effect on packing density, due to small particles filling the small voids [33], and powder compactibility [34] Small particles are light and get easily thrown out of the process zone, furthermore due to their surface to volume ratio they are more likely to inflame or explode if making contact with reactive gas [32] Small particle size and narrow particle size distribution leads to uniformity in the melt pool, and results in a higher part density [32,33] Powder bed density influences the resulting heat transportation and thus the heat balance [32]	Process: Optimal powder layer thickness, heat balance of the powder bed, consistency in melt pool, packing density, compactibility, dispersing Product: Density
Flowability	Affects the layer deposition and layer quality (e.g., homogeneous layers) [35,36]	Process: Layer deposition
Reflectivity, absorptivity	Laser energy is absorbed (absorptivity) or reflected in the process chamber (reflectivity) by the powder bed [32] Absorptivity of a powder depends on the wavelength of the laser and the condition of the powder bed [32] High reflectivity of the powder bed (>91% for aluminum) requires an increase in laser power [37–39]	Process: Variations in energy input, required laser power, and wavelength
Thermal conductivity	High thermal conductivity increases the required laser power [38,39], which leads to a rapid dissipation of heat away from the melt pool [37]	Process: Required laser power, melt pool temperature
Oxidation	Oxides form during the process (oxygen level 0.1 to 0.2%) [37] Theory: most predominant factor controlling the flowability is the amount of surface oxides on particle surface Rupture of the oxide layer of small powder particles is more difficult [40]	Process: Obstacle for effective melting, adherent thin oxide films on molten aluminum reduce wettability Product: Involved oxide: region of weakening
Humidity, hydrogen	Single or multiple molecular layers can form on the particle surface, leading to hydrogen bonding [41] Increased interparticular forces lead to a decrease in flowability [33,41,42] and the metal microstructure of the part [5] On the particle surface and in the powder material can lead to hydrogen porosity [43,44]	Process: Powder flowability Product: Metal microstructure, hydrogen pores
Particle shape, morphology	Typical powder defects are irregular shapes e.g., elongated particles, satellites, hollow or porous particles [11,44] Affects flowability [33], spherical particle morphology is beneficial for powder flowability and helps to form uniform powder layers [43] Excessive amounts of large pores or pores with entrapped gas can affect material properties [44] Stacking density is a function of the powder morphology [32] Surface roughness affects the absorptivity [32]	Process: Powder flowability Product: Layer deposition, absorptivity
Surface oxide of powder particles	Nonuniform in thickness of particles surface oxide (from 30 to 40 up to three monolayers, in case water-atomized powder of aluminum alloys), therefore melting temperature increases [45]	Process: High temperature strengthening phase Product: Mechanical properties

Adapted from Dietrich S, Wunderer M, Huissel A, Zaeh MF. A new approach for a flexible powder production for additive manufacturing. Proc Manuf 2016;6:88–95.

2.2 Fe-C system: stable and metastable equilibrium diagrams

The knowledge of the thermodynamic principles and modern thermodynamic data now permits accurate calculations of the Fe-C diagram. This is useful for phase boundaries extrapolation and at low temperatures where the experimental equilibria are extremely slow to develop. The study of the steels and cast irons start with the Fe-C diagram. It reports the phases of the alloy in thermodynamic equilibrium conditions. The diagram in Figure 13 presents 3 horizontal lines that are not variable (Variance = 0), the peritectic at 1495°C, the eutectic transformation at 1148°C and the eutectoid transformation at 727°C.
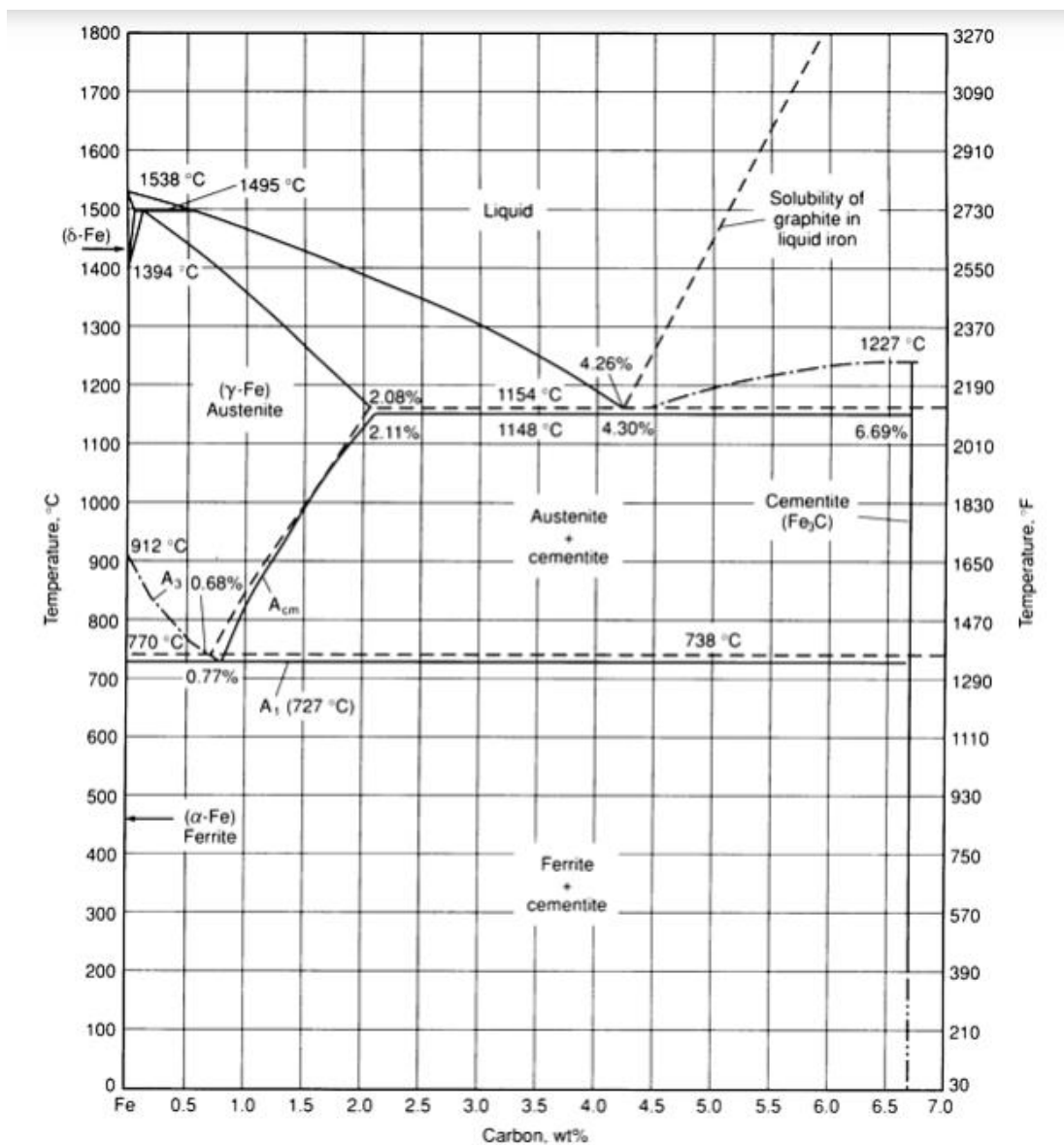
Figure 13: The Fe-C equilibrium diagram up to 6.67 wt.% C. Solid lines indicate iron-cementite diagram; dashed lines indicate iron-graphite diagram [33]

Figure 13 presents two diagrams: the stable iron-graphite diagram (dashed lines) and the metastable iron-cementite (Fe-Fe_3C) diagram. The stable condition is not reached at low temperature and low-carbon range and usually takes very long time to develop. The Fe-C diagram shows which phases are to be expected at equilibrium or metastable equilibrium for different combinations of carbon concentration and temperature. The important phases and microconstituents are summarized in Table 7. Most of the phases described can be seen in the Scanning Electron Microscope (SEM) micrographs in

Figure 14. At low carbon content, ferrite (α-iron) can be distinguished, which can at most dissolve 0.028 wt.% C at 727 °C and austenite (γ-iron), which can dissolve 2.11 wt.% C at 1148 °C (Figure 13). At the carbon-rich side there is cementite (Fe_3C) (

Figure 14). At the highest temperature, except for highly alloyed steels, the δ-ferrite is the equilibrium phase. Between the single-phase fields are found regions with mixtures of two phases, such as ferrite + cementite, austenite + cementite, and ferrite + austenite. At the highest temperatures, the liquid phase field can be found and below this are the two-phase fields liquid + austenite, liquid + cementite, and liquid + δ-ferrite. In heat treating of steels, the liquid phase is always avoided. Some important boundaries at single-phase fields have been given special names that facilitate the discussion such as A_1, the so-called eutectoid temperature, which is the minimum temperature for austenite, A_3, the lower-temperature boundary of the austenite region at low carbon contents, that is, the $\gamma/\gamma + \alpha$ boundary and A_{cm}, the counterpart boundary for high carbon contents, that is, the $\gamma/\gamma +$ Fe_3C boundary. The letters c, e, or r can be included. The eutectoid carbon content (0.77 wt.% C) is defined as the amount of carbon at which the minimum austenite temperature is attained. The ferrite-cementite phase mixture of this composition formed during cooling has a characteristic appearance and is called pearlite (

Figure 14) and can be treated as a microstructural entity or microconstituent. It is a phase formed by alternated ferrite and cementite with a lamellae form. The cementite of this phase can spherodize or coarsen into particles dispersed with a ferrite matrix after extended holding close to A_1 [34].
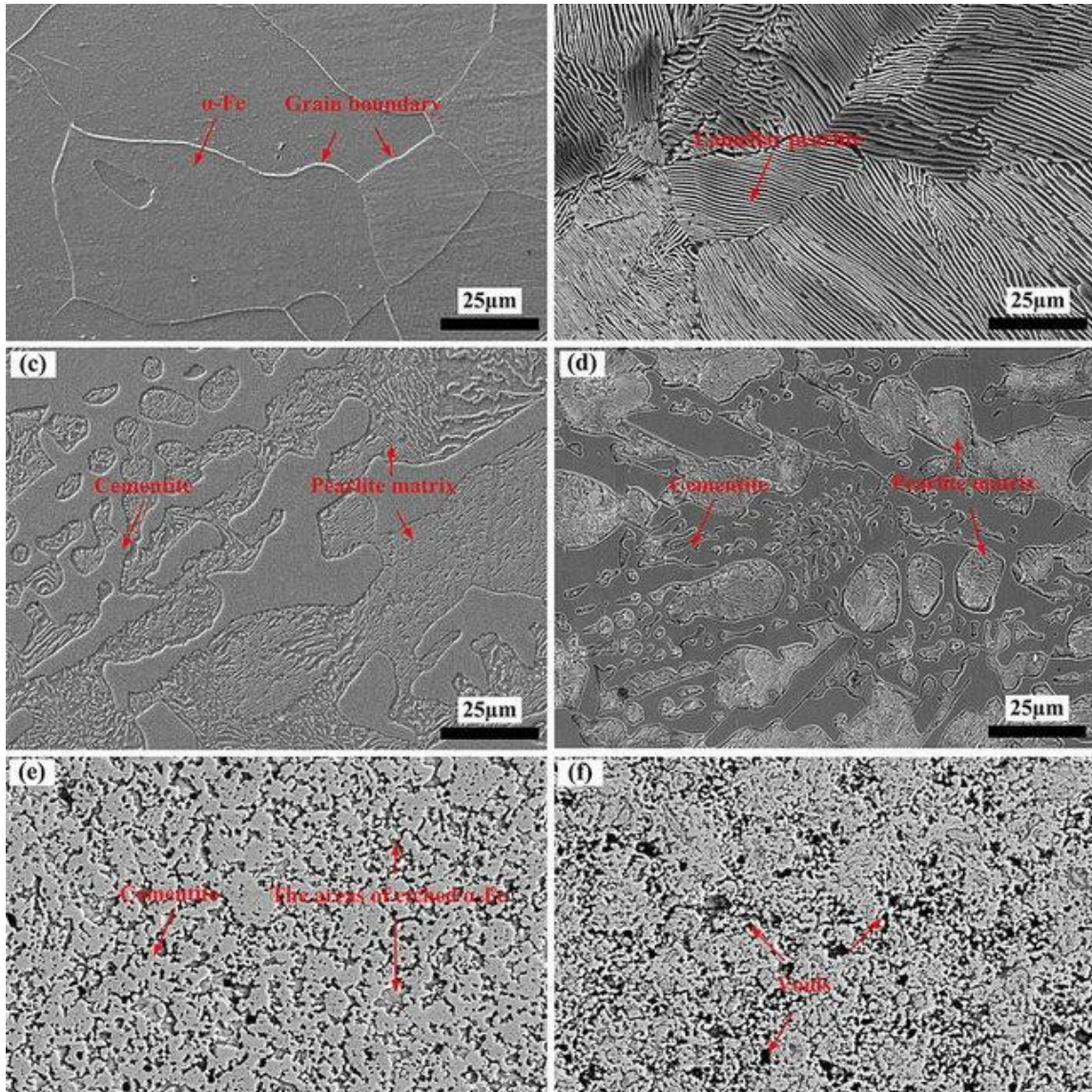
Figure 14: SEM microstructure of specimens with different volume fractions of cementite: a) pure iron, b) Fe-7.83 vol.% cementite, c) Fe-18.56 vol.% cementite, d) Fe- 49.21 vol.% cementite, e) Fe-81.75 vol.% cementite, and f) single cementite[35]

Table 7: Important metallurgical phases and microconstituents[34]

Phase (microconstituent)	Crystal structure of phases	Characteristics
Ferrite (α-iron)	bcc	Relatively soft low-temperature phase; stable equilibrium phase
δ-ferrite (δ-iron)	bcc	Isomorphous with α-iron; high-temperature phase; stable equilibrium phase
Austenite (γ-iron)	fcc	Relatively soft medium-temperature phase; stable equilibrium phase
Cementite (Fe_3C)	Complex orthorhombic	Hard metastable phase
Graphite	Hexagonal	Stable equilibrium phase
Pearlite		Metastable microconstituent; lamellar mixture of ferrite and cementite
Martensite	bct (supersaturated solution of carbon in ferrite)	Hard metastable phase; lath morphology when <0.6 wt% C; plate morphology when >1.0 wt% C and mixture of those in between
Bainite	. . .	Hard metastable microconstituent; nonlamellar mixture of ferrite and cementite on an extremely fine scale; upper bainite formed at higher temperatures has a feathery appearance; lower bainite formed at lower temperatures has an acicular appearance. The hardness of bainite increases with decreasing temperature of formation.

2.2.1 Physical Metallurgy of Fe-C-Si System

Numerous studies have been done in order to completely understand the phase diagram and the thermodynamic properties of the phases involved in the Fe-C-Si system due to the importance of this system for steelmaking processes and cast-iron foundry [36]. To describe the Fe-C-Si system, the Fe-Si system is combined with Fe-C and Si-C systems [37]. Patterson et al., using experimental methods, develops a diagram in composition plane [38] [39].
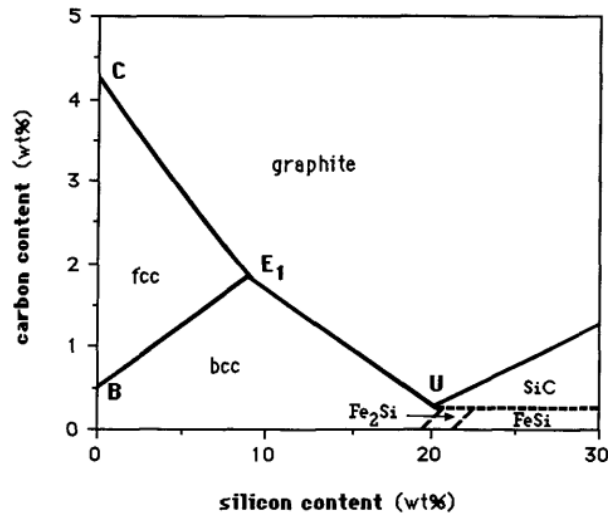
Figure 15: Projection on the composition plane of the liquidus surface of the stable Fe-C-Si diagram, Points B and C are respectively the peritectic and the eutectic point of the binarysystem. Points E₁ and U are ternary eutectic points[38]

As can be seen in Figure 15, the face-centered cubic (fcc) liquidus, falls below the body-centered cubic (bcc) liquidus surface when silicon is added at constant carbon content, and the temperature of the two liquidus surface is continuously decreased. This work has been developed and corrected by many researchers for stable and metastable diagrams [[40][41][42][43][44]]. Based on all the works done until theirs, Lacaze and Sundman [44] propose a ternary diagram of Fe-C-Si system obtained with ThermoCalc® at defined temperature of 1000°C and illustrated in Figure 16.
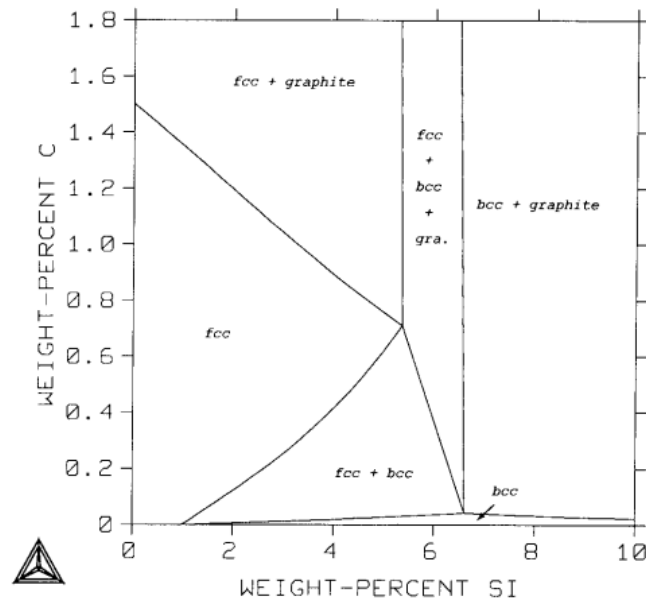
Figure 16: Calculated isothermal section (1000°C) of the iron-rich comer of the stable Fe-C-Si system

2.2.2 Metallurgy of cast irons

Up to now, the iron-carbon phase diagram has only been considered up to a carbon content of 2.11 wt.%. If this carbon content is exceeded, further phase transformations occur. This also results in other material properties and this difference is also reflected in the subdivision into *steels* and *cast iron*. Ferrous materials with a lower carbon content than 2.11% are referred to as steels and solidify as a solid solution, while ferrous materials over 2.11% are referred to as cast iron with crystal mixture solidification of iron-carbon compound. As consequence, the mechanical properties of steels and cast irons differ at room temperature [45].

Cast irons can be classified as white cast irons and grey cast irons according to the solidification. In this way, white cast iron can be obtained when the solidification follows the metastable diagram (iron-cementite), while grey cast iron is obtained following the stable equilibrium diagram (iron-graphite). In many industries, the metastable diagram (solid lines) is followed due to the cooling rates for which liquid formed by iron and 4.3% of carbon habitually solidifies at 1148°C as a kind of eutectic aggregated called ledeburite (Figure 17). Ledeburite is formed by austenite (of 2.11%C) and cementite (of 6.67%C), and its weight percentage in austenite and cementite are respectively 51.9% and 48.1%. In case of slow cooling rates, a liquid in the same condition (specifically 4.26% of C at 1154°C) can solidify following the stable diagram and result a eutectic of carbon in the form of graphite, and austenite in a weight percent of 2.33% and 97.67% respectively. In rolling cylinders, wheels, and thick plates, both types of eutectics can be obtained, ledeburite in the external zones and eutectic graphite in the inner zones of the part due to the lower cooling rate in the internal zones. So, for small amounts of eutectic liquids that were cooled at different cooling rates, if the rate is high, the molten metal solidifies at 1148°C and results in a eutectic of cementite and austenite, while on the contrary if the cooling rate is low, the solidification occurs at 1154°C and eutectic graphite and austenite is obtained as shown in the Figure 18. The affinity between carbon and iron takes part in the appearance of cementite for obtaining the intermetallic compound Fe_3C. This is the reason for the less time required to obtain cementite than to achieve graphite [34].
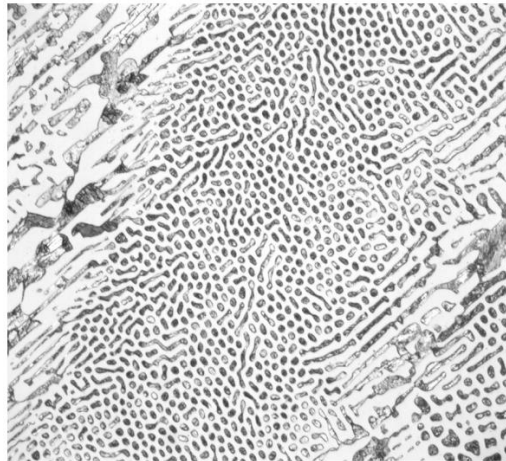
Figure 17: Ledeburite in a white cast iron (Fe–4.0% C–0.3% Si–0.16% Mn–0.91% Cr) etched with Beraha's sulfamic acid reagent. Original at 500x magnification. Taken in polarized light with sensitive tint [46]
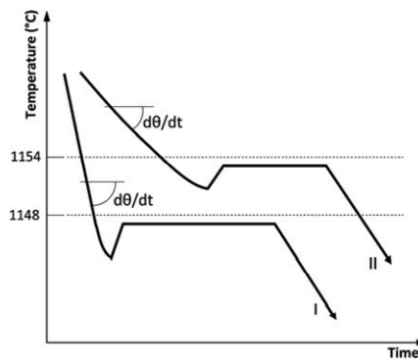
Figure 18: Fe–C stable eutectic and iron-cementite metastable eutectic formation according to the cooling rate. Curve I: metastable eutectic. Curve II: metastable eutectic[34]

Table 8 lists compositions and distinctive microstructural features for common cast irons. Ferrite and pearlite are defined identically to steel, and ausferrite is a two-phase, high-carbon austenite matrix with embedded ferrite lathes [47]. The composition of cast irons is defined by the Carbon Equivalent (CE) that is a value in weight percentage that combine the effects of the different elements present in the alloy in order to, as the name suggests, calculate the equivalent amount of carbon [48]. This is especially useful to determine in which position on the Fe-C diagram the alloy is without determine the new position of the eutectic (hypo or hypereutectic). There are different empirical expressions, and one of these is given by the Equation 2, in which it can be observed that carbon and silicon largely detrmine the microstructure of cast products immediately after solidification.

Equation 2 $\quad CE = C\% + 0.317Si + 0.33\,P - 0.027Mn$

Equation 2 is very useful to determine the range of cast iron according to Table 8. The determination of the type of cast iron according to Carbon and Silicon content is summarized in Figure 19 [49].

Table 8: Cast iron composition ranges and microstructures [47]

Type	C range (wt%)	Si range (wt%)	CE range	Usual composition	Eutectic product	Graphite shape	Common RT matrix microconstituents
Gray	2.5–4.0	1.0–3.0	2.8–5	Hypo	γ + graphite	Platelets	Ferrite, pearlite
Ductile	3.0–4.0	1.8–2.8	3.6–4.9	Hyper	γ + graphite	Spheres	Ferrite, pearlite, ausferrite
Malleable	2.0–2.6	1.1–1.6	2.4–3.2	Hypo	γ + carbide	'Popcorn'	Ferrite, pearlite
White	1.8–3.6	0.5–1.9	2–4.3	Hypo	γ + carbide		Ferrite, pearlite
Compacted	3.0–4.0	1.8–2.8	3.6–4.9	Eutectic	γ + graphite	Rods	Ferrite, pearlite
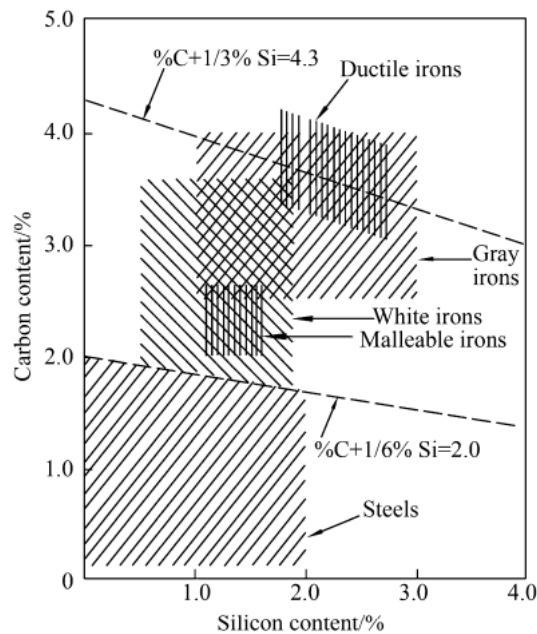
Figure 19: Definition of cast iron alloys according to carbon and silicon[49]

2.2.2.1 Influence of alloying elements

The Fe-C diagram in Figure 13 shows the variation of A_1 and the eutectoid carbon content with increasing amount of a selected number of alloying elements shown in Figure 20. The important alloying elements decrease the eutectoid carbon content, the austenite-stabilizing elements such as manganese and nickel decrease A_1, and the ferrite-stabilizing elements such as chromium, silicon, molybdenum, and tungsten increase A_1 [50].
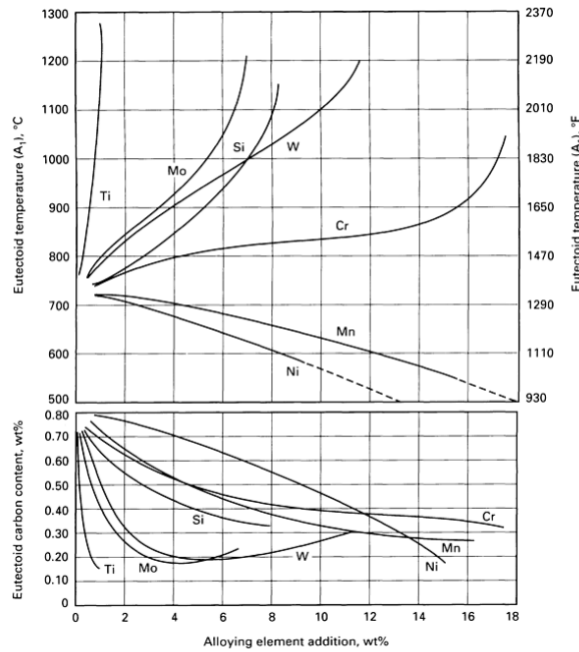
Figure 20: Influence of alloying element additions on eutectoid temperature and eutectoid carbon content [51]

In cast irons, elements can be added to increase the mechanical properties. Since the hypoeutectic composition is favourable for mechanical properties, the eutectic point position is important. Elements other than Fe and C can change the location of the eutectic. Lot of elements can promote graphitization and influence the structure of the matrix. In fact, for achieving the formation of graphite in the case of eutectic liquids and industrial cooling rates, even if they are low, the presence of graphitizing elements, such as Si, P, Al, Ni or Cu (Figure 21) are required. The presence of these elements in the liquid is effective due to both the dilution and the affinity effects. Graphitizing elements dissolve the pre-clusters of Fe and C necessary for the formation of cementite clusters. As consequence, the kinetics of cementite is retarded, and the formation of graphite is promoted. These inoculants facilitate the heterogeneous nucleation of graphite by epitaxy or crystallographic similarity. The nucleation rate and the refining of the graphite increase. The inoculation efficiency decreases with the time, and that is why in industry the casting occurs as soon as possible [34]. It is found that Mn and Ni increase the interlamellar spacing of pearlite, whereas an increasing content of Cr produces finer pearlite spacing. Si has only a slight influence on pearlite spacing [52].
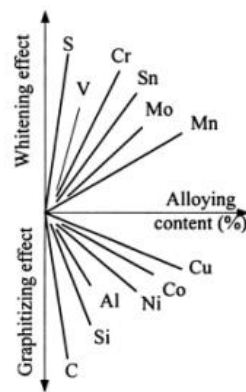
Figure 21: Effect of alloy elements on the microstructure of cast iron [48]

The addition to iron-carbon alloys of elements such as Ni, Si and Mn, which do not form carbides in competition with cementite, does not alter the microstructures obtained after transformation. In different way Mo, Cr and W are strong carbide-forming elements and cementite will be replaced by the appropriate alloy carbides, often at relatively low alloying element concentrations. Still stronger carbide forming elements such as Nb, Ti and V can form alloy carbides, preferentially at alloying concentrations less than 0.1 wt.%. As consequence of the presence of these elements, the microstructure will be altered. The difference of solubility of carbon in austenite and ferrite leads to ferrite/cementite aggregates in carbon steels. Carbides and nitrides, compared to cementite, are less soluble in austenite. Cr and Mo carbides are not included, but they are more soluble in austenite than the other carbides. Studies indicate that for Nb and Ti, concentrations higher than 0.25 wt. % lead to the formation of excess alloy carbides which cannot be dissolved in austenite at the highest solution temperature. The solubility limit of V is found to be 1-2% and for Mo, about 5 wt.% [53].

- Influence of Silicon in Cast Irons

Silicon and its dissolution in liquid iron contribute to the formation of graphite due to an increase of the thermodynamic activity of carbon in silicon-enriched microvolumes of cast iron. The dissolution is followed by a high speed and uniform distribution throughout the volume [54]. From all the elements that are used for achieving the graphite + austenite eutectic transformation, avoiding the appearance of ledeburite, silicon is the main low-cost graphitizing agent. Aluminium, for instance, is an energetic graphitizing element (Figure 21); but its addition reduces the castability and it usually produces surface defects in the parts. Silicon percentages, which are required to avoid the ledeburite formation in the plain and low-alloyed cast irons, range between 2 and 6%. when the quantity of silicon in the cast iron is increased, the temperature gap between stable and metastable binary

eutectics is increased as shown in Figure 22, favouring the eutectic of graphite (in stable solidification). As consequence, the formation of graphite is possible even for faster cooling rates. Increasing too much the cooling rate, the formation of ledeburite could not be avoid [34].
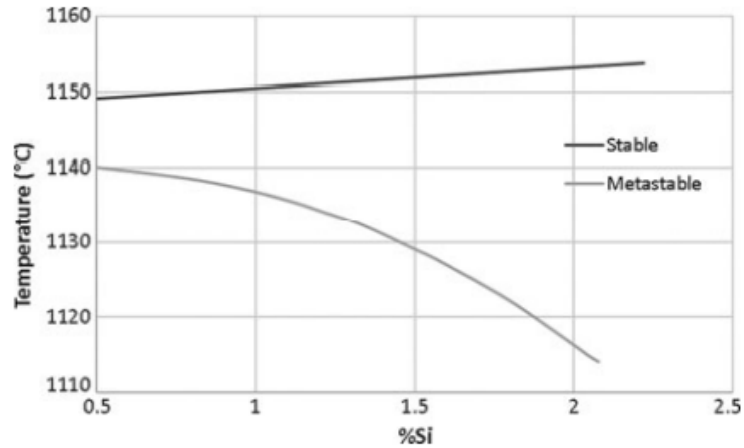
Figure 22: Beginning temperatures of both stable and metastable eutectics as a function of the silicon amount (wt.%) [34]

- Influence of Molybdenum in Cast Irons

Molybdenum acts as carbide stabilizer in cast iron and can be added to most grades of cast iron without changing the character of the charge, the normal metal practice, or the base metal. At low addition level it has trivial effect on castability and chilling tendency. Free carbides are only formed at higher molybdenum addition (Figure 23 and Figure 24). The amount and shape of graphite are not measurably affected by molybdenum additions below 0.5% [55].
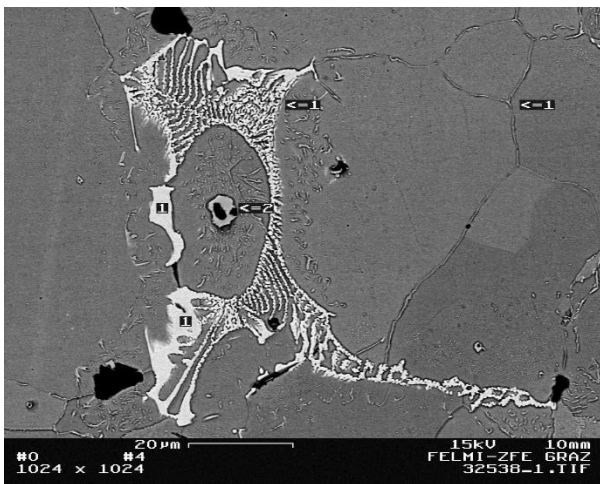
Figure 23: Typical molybdenum carbides of GJS, 1000:1, etched[56]
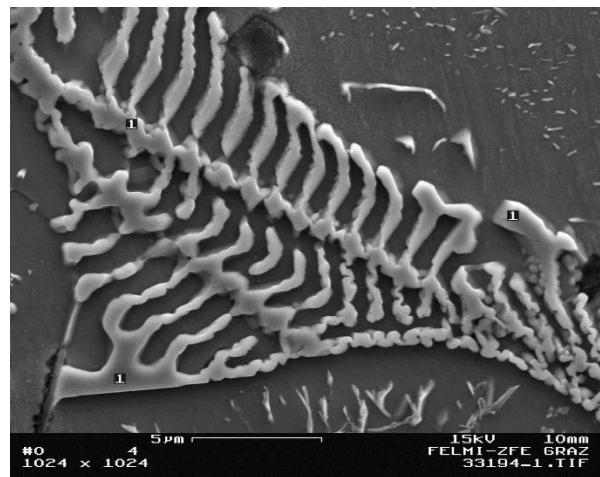
Figure 24: SEM- micrograph of molybdenum carbides, 5000:1[56]

The main effect of molybdenum in cast iron is observed during solid state transformations with the increase of molybdenum content that causes the shifting of pearlite phase field in the

continuous cooling transformation (CCT) diagram towards longer times. Molybdenum addition up to around 0.5% acts a powerful pearlite stabilizer and increases strength by refining pearlite. An addition of higher molybdenum content, preferably in conjunction with nickel or copper, promote the transformation of austenite into acicular ferrite. Such irons usually contain at least 0.8% Mo and more than 1.2% Ni. Molybdenum also has the strongest effect in decreasing the interlamellar spacing of pearlite [52].

Molybdenum increases the wear resistance of grey iron, promoting the formation of uniform fine pearlitic matrix. It also increases toughness which reduce chipping. The use of grey irons for cylinder liners and other parts exposed to frictional contact is well known, and this is due to the lubricating action of the graphite flakes. The frictional wear resistance is improved by increasing the hardness of the matrix structure and by promoting the formation of the most favourable pearlitic structure [55].

2.2.2.2 Graphite morphologies in stable system

The undercooling affects the crystallization of graphite that starts with nucleation. Many research focus and explain the nucleation of the graphite in the melt [[57][58][59]]. Logically, some graphite nuclei appear inside of eutectic liquid after a certain period, and their growth provides as much eutectic cells as graphite nuclei appeared. The number and morphology of graphite that forms will depend on its nucleation rate and the graphite and austenite associated growing rate. Briefly, it will depend on the liquid cooling rate [34].

Ductile spheroidal graphite (SG) can be divided into fully ferritic, ferritic-pearlite and fully pearlitic ductile iron according to their matrix microstructure. The mechanical response of ductile iron is also related to matrix microstructure. Ductile iron contains nodular graphite that increase the ductility and decrease the crack initiation phenomenon. In flaky graphite iron (FG), the lamellae growing is a cooperative irregular eutectic. Lamellar graphite in flaky graphite iron can have different morphologies depending on the initial composition and the cooling rate during solidification [60].
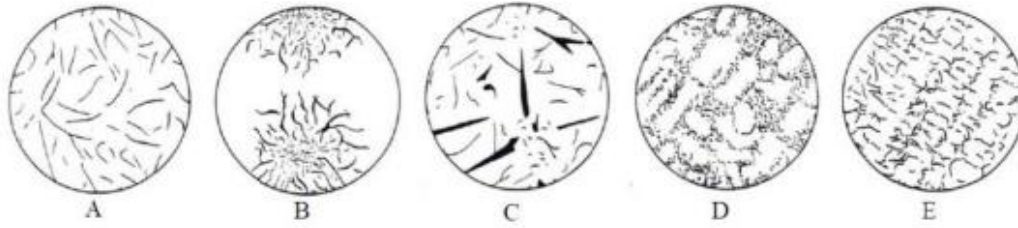
Figure 25: Schematics of the five classes of flaky graphite- DIN EN ISO 945 [61]

When the molten metal is hypereutectic (Carbon Equivalent higher than 4.25%), the solidification begins with the primary graphite formation in the range between the liquidus and the eutectic temperatures. The primary graphite grows freely inside of the liquid, without obstacles in its growth, and generates flakes whose thickness exceeds that of the subsequent eutectic graphite. This primary graphite is known as graphite type C shown in Figure 25. Initially, primary flakes appear until reaching the eutectic temperature, and the solidification continue following the eutectic path. At the end of solidification, there are two different morphologies of graphite: primary graphite type C, and eutectic graphite, which can be type A or type B depending on the cooling rate. On the other hand, the solidification of the hypoeutectic cast irons begins with the appearance of primary austenite. This austenite continues to freeze in the corresponding temperature range between liquidus and eutectic, and when the eutectic temperature is reached the graphite rosettes (type B) and the eutectic austenite appear [[62][63][64]]. It is important to know that there are not differences between primary and eutectic austenite. The interactions between austenite dendrites and cells are shown in Figure 26. In the case where the undercooling is to fast to produce a premature cover of the graphite during its growth, the rosette's formation would be avoided. In Figure 25 (type D and E), it is possible to see that dispersed austenite dendrites stand out over a eutectic whose graphite appears as punctual (graphite type D). In the same cast iron, if the liquid undercooling was much faster, the metastable eutectic temperature would be achieved without giving time to the graphite appearance. In this case, cementite would solidify and, it would be obtained as ledeburite instead of the stable eutectic of austenite and graphite. When the cast iron is very hypoeutectic (low carbon content), a higher amount of silicon would be required to avoid the appearance of ledeburite, and before reaching the eutectic temperature almost all the liquid will have solidified as primary austenite dendrites. The remaining eutectic liquid should be stored in the small interdendritic spaces. And this small amount of remaining eutectic liquid when solidifies without enough space for the properly development as rosettes, produces peculiar graphite morphology known as graphite type E, which draws the interdendritic spaces as a rib [34].
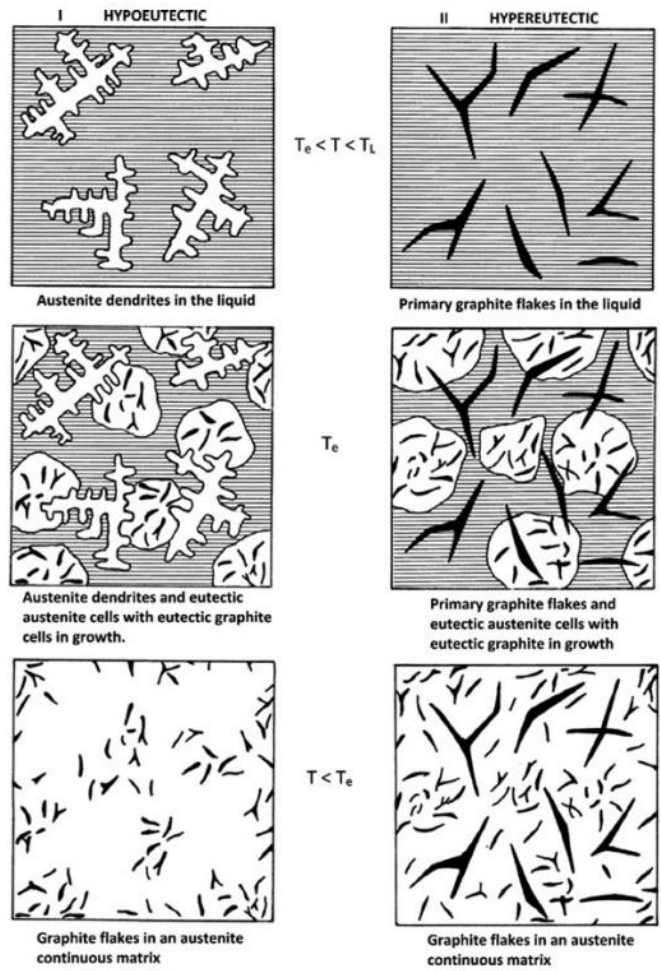
Figure 26: Grey cast iron microstructure evolution during the solidification [34]

3. EXPERIMENTAL METHODS

3.1 Original Powders

In this work, powders of AISI S2 (AISI type: Shock-Resisting Tool Steel) and Silicon Carbide (SiC) are used and mixed together in different volume percentage.

3.1.1 S2 Tool Steel

S2 powder produced by Gas Atomisation, were provided by SANDVIK OSPREY LTD [65]. Table 9 shows the chemical composition. The morphology of the powders is shown in Figure 27.

Table 9: Chemical composition of S2 Tool Steel powders

Element	C	Si	Mo	Mn	Fe
wt.%	0.49	1.2	0.6	0.6	Bal.
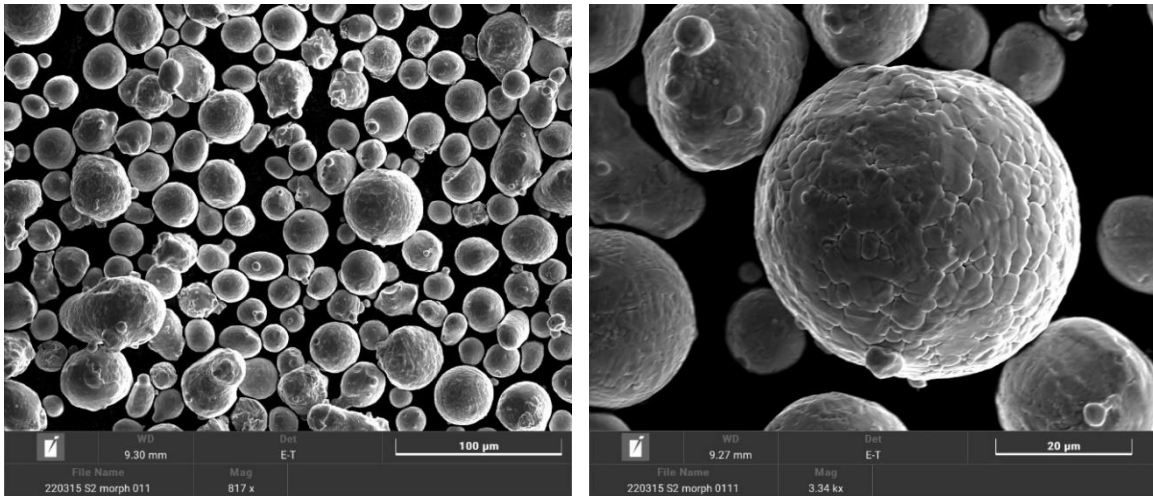
Figure 27: SEM micrographs of S2 powders

3.1.2 Silicon Carbide (SiC)

Alpha SiC powder were provided by H.C. Starck Ceramics Gmbh [66]. Table 10 shows the chemical composition.

Table 10: Chemical composition of SiC powders

Element	C	O	Al	Ca	Fe
wt.%	29-30	max. 1.5	max. 0.03	max. 0.01	max. 0.05

The morphology of SiC powders is irregular as shown in Figure 28, and at granule scale, it is observed that the powders tend to form agglomerates. The dimension of 50% of the powders is 0.75µm (Annex 1).
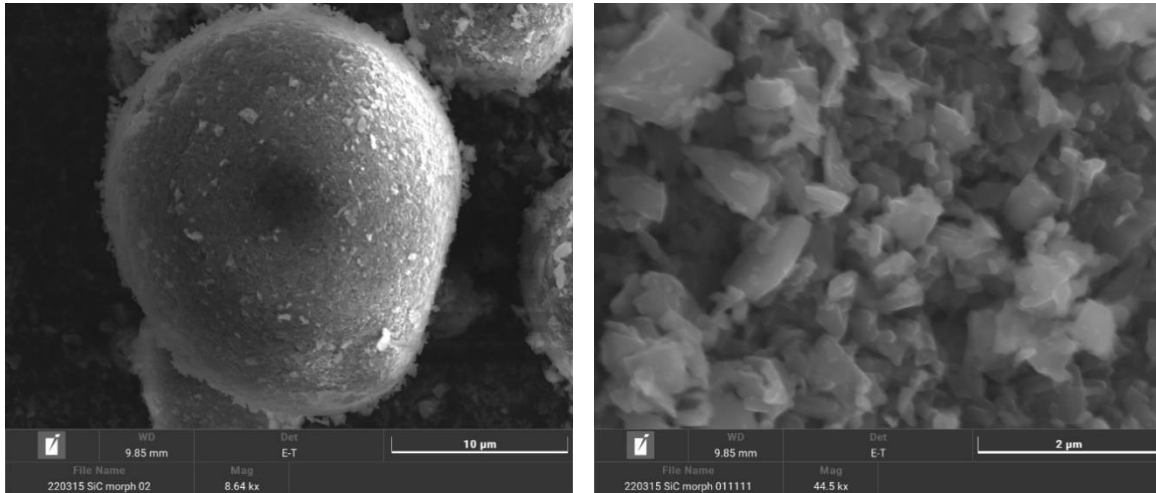
Figure 28: SEM micrographs of SiC

3.2 Samples preparation

3.2.1 Manual mixing of powders (S2 + X% (in volume) of SiC)

For this work, mixtures at different volumetric concentration of SiC were prepared, using the density of the two powders (S2 and SiC) for the calculations. The aim of this preparation is to understand the influence of the Silicon Carbide on the microstructure at low cooling rates. The mixture's method for the DTA test is simply manual. Knowing the composition of the S2 and SiC powders and the concentrations of the powders into the mixtures, it is possible to calculate the weight fraction of the elements in the mixture, and using the Equation 2, the Carbon Equivalent (CE) could be determined.

Table 11: Chemical composition of the different mixtures prepared manually

Vol.% SiC	C (wt.%)	Si (wt.%)	Mo (wt.%)	Mn (wt.%)	CE (wt.%)
S2+20%SiC	3,175	7,468	0,547	0,547	5,475
S2+15%SiC	2,439	5,750	0,561	0,561	4,207
S2+10%SiC	1,773	4,196	0,575	0,575	3,059
S2+5%SiC	1,081	2,579	0,588	0,588	1,864

3.2.2 Ball milling

The device used to mill the powders is 'Pulverisette 6'[67] . The equipment is composed by a double turning system in which a bowl, which contains powders and balls, is located. The bowl and the balls are made in tungsten carbide (WC), as shown Figure 29. The parameters that can be set up

are the bowl rotational speed (up to 650 rpm), the milling time, the break time, and the number of repetitions.

Figure 29: Milling equipment

During the milling process, the powders are picked up on a disc with adhesive paper as shown in Figure 30**Errore. L'origine riferimento non è stata trovata.** in order to observe the mixture at SEM and look at the effect of the milling process on the mixture powders.
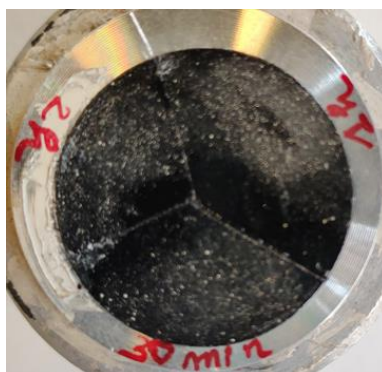
Figure 30: Powders on adhesive paper

3.2.2.1 SiC

A ball Milling process is provided on SiC powder in order to break the granules (Figure 28). After each stop a break time of 15min is achieved and a small amount is collected.

Table 12: Milling parameters for SiC

Ball to Powder Ratio	Mass [g]	Balls number	Rotational speed [rpm]	1st stop	2nd stop	3rd stop	4th stop
1:3	159	7	100	30min	1h	1h30	2h

3.3 Characterization

3.3.1 Differential Thermal Analysis (DTA)

The DTA tests were performed with a NETZCH STA 449C Jupiter DTA. This device can perform a Thermo Gravimetric Analysis in contemporary with the DTA. It can also operate under a high vacuum or under protective atmosphere [68].

Figure 31: NETZCH STA 449C Jupiter [68]

DTA is used to investigate the influence of the SiC addition on S2 and the influence of cooling rate on the microstructure. The different DTA tests are listed in Table 13.

Table 13: DTA tests on powders

Powders (vol.%)	m S2 [mg]	m SiC [mg]	Heating [°C/min]	Max Temperature [°C]	Cooling [°C/min]
S2+20%SiC	780	80,55	5	1550	5
S2+15%SiC	800	58,32	5	1550	5
S2+10%SiC	820	37,64	5	1550	5
S2+5%SiC	840	18,26	5	1550	5
S2	/	/	5	1550	20
S2+20%SiC	780	80,55	5	1550	20
S2+15%SiC	800	58,32	5	1550	20

| S2+10%SiC | 820 | 37,64 | 5 | 1550 | 20 |
| S2+20%SiC | 778 | 79,4 | 5 | 1120 | 20 |

3.3.2 Microstructural characterization

To characterize the microstructure of the powders and DTA samples, Optical Microscope (OM) and Scanning Electron Microscope (SEM) are used.

3.3.2.1 Samples preparation

The pieces resulting from DTA are incorporated in Bakelite using the STRUERS Citopress-1. The cylindrical Bakelite, with inside the part, is polished in multiple steps using the STRUERS Tegramin-30 to obtain a sample with very low roughness. An etching with 3% Nital is applied in some samples to highlight the microstructure phases [69].

STRUERS Citopress-1

STRUERS Tegramin-30

Figure 32: STRUERS equipment [69]
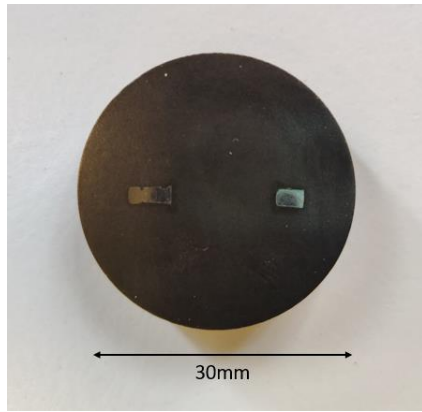
Figure 33: Sample after preparation
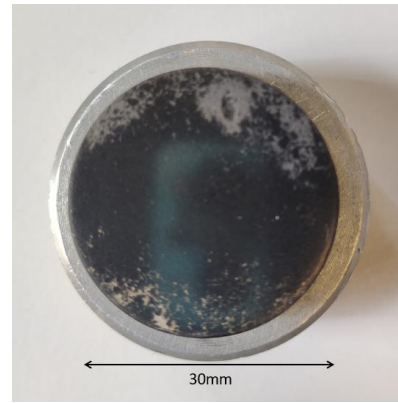
Figure 34: Powders cross section sample after preparation

The same process is used for the powders to obtain the cross sections (Figure 34).

3.3.2.2 Optical Microscope (OM) and Stream Analysis Software

The Optical Microscope ''Olympus BX60 Microscope''[70], shown in Figure 35, is used for the analysis with the help of the Stream Analysis Software. All the magnified images (2.5x, 5x, 10x and 20x) of the sample in Bakelite (Figure 33) and on adhesive (Figure 36) for the powders are obtained by this method.

Figure 35: Olympus BX60 Microscope [70]
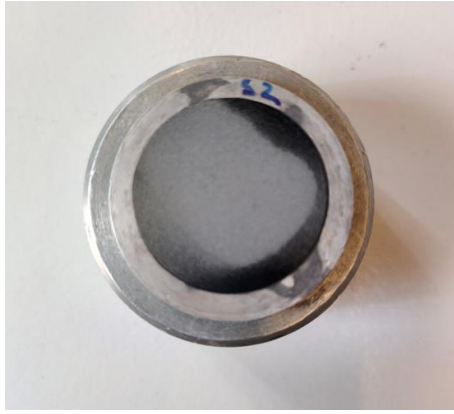
Figure 36: sample after preparation of powders on adhesive

The Stream Analysis Software is an advanced tool for acquiring and processing images. It also allows the quantification of the phases separating and quantifying the different tints present in the images.

3.3.3.3 Scanning Electron Microscope (SEM)

A Tescan Clara Ultra-High Resolution (UHR) SEM (Figure 37) is used for observation at high magnification, to make point analysis, line scan, spectral mapping and Electron Back Scattering Diffraction (EBSD) analysis[71]. These analyses are useful to obtain compositions in single points or on a line, to determine the elements and the phases present into the microstructure.

Figure 37: Tescan Clara Ultra-High Resolution [71]
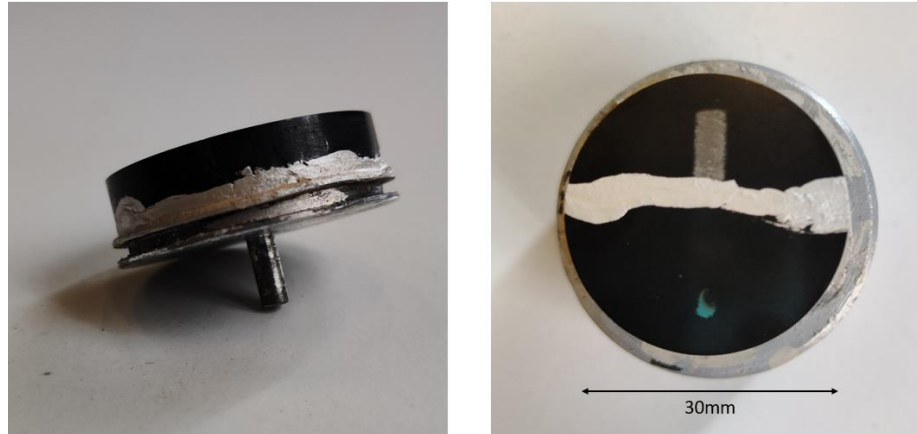
Figure 38: Sample after preparation with silver paint

The SEM analysis require an additional step of samples preparation. In particular, the samples need a support that allows to fix the sample in the SEM. Moreover, the part to observe is connected to the conductive support using a silver paint (Figure 38).

3.3.3 Rheological properties of S2 + 15% (in volume) of SiC powders

To understand the particles behaviour after ball milling, the characterization of the powders is necessary. Rheological properties and particles characterization are done in collaboration with Granutools™ and Greenmat, using technologies made available by them for this study.

3.3.3.1 Tap Density

Tap density measurement is done using the GranuPack (Figure 39) [72]. Moreover, the device allows the measurements of bulk density, Hausner ratio and Carr index that are very popular properties for powder characterization useful to understand the flowability and the processability of the powders.

The powders were fed in a tube that will release slowly the powder in the measurement cell. Then, a cylinder was placed on the top of the powder bed to flatten the interface and keep it flat. During the test, the GranuPack will tap the powder with either 1mm or 3mm free fall taps. After each tap, the height of the sample will be measured automatically with an inductive sensor. The volume and the density were calculated using the height of the sample, and the results were plotted in real-time. At the end of the measurement, several characteristics will be displayed in the table like the Hausner Ratio, the Carr's index, the bulk density, the final density, and the characteristic tap number $n_{1/2}$ [72].

For the evaluation of tap density in collaboration with Granutools, the GranuPack test is set with a tap's number of 1500 (in order to reach a plateau in the graph), a frequency of 1 Hz is set for the first 100 taps and a frequency of 2 Hz after the first 100 taps.

Figure 39: GranuPack equipment [72]

The test was done for the mixtures prepared through Ball Milling after 2 hours for S2 + 15% (in volume) SiC and after 1h30min for S2 + 15% (in volume) of pre-milled SiC powders. To ensure the validity of the results, two evaluations were made for each mixture.

3.3.3.2 Cohesive Index

The rheological properties of the powders have been assessed by GranuDrum (Figure 40) through a rotating drum method [[72] [73]. The cohesive index and the interface fluctuation is reliable to the spreadability of powder to the layer homogeneity in SLM [74].

A transparent drum cylinder is rotating around its axis half-filled with a sample of powder. The rotation starts and the drum will rotate at different velocities. A camera takes a snapshot during the rotation then the software can analyse the pictures stacked per speed. The analyses give the measurements for the cohesive index and flowing angle per speed. The cohesive index is only related to the cohesive forces between the grains. The average interface position gives the flowing angle, and the dynamic cohesive index is measured from the interface fluctuation. The flowing angle is influenced by a wide set of parameters: the friction between the grains, the shape of the grains, the cohesive forces between the grains (Van der Waals, electrostatic and capillary forces). The cohesive index is only influenced by the cohesive forces. The trend observed gives information on the way the powder behaves under a certain level of stress state or speed. If the speed increases in the rotating

drum (and so the stress state) and the cohesive index increases, this behaviour is called shear-thickening, the opposite way is called shear-thinning behaviour [75].

A cohesive powder leads to an intermittent flow while a non-cohesive powder leads to a regular flow. Therefore, a cohesive index closes to zero corresponds to a non-cohesive powder.

Figure 40: GranuDrum equipment [76]

3.3.3.3 Phases analysis by X-Ray Diffraction (XRD)

In order to determine the effects of the methods used for the mixing of S2 + 15% (in volume) of SiC powder on the microstructure of the particles, the Bruker D8 Discover Twin-Twin, owned by Greenmat is used (Figure 41)[[77][78]].

Figure 41: Bruker D8 Discover Twin-Twin [77]

4. RESULTS

4.1 Powders characterization

The evaluation of the behaviour of the powders starts with the characterization of the powders. The determination of morphology, composition, dimensions and physical properties is done to ensure the application of the powders and powders mix for SLM.

4.1.1 Virgin powders

4.1.1.1 S2 powder

The morphology of the S2 powders is evaluated at Scanning Electron Microscope (SEM). In addition, through the use of EDS and the Electron Backscattered Diffraction (EBSD), the composition and the phase present are determined.

Most of the powders has a spherical shape as shown in Figure 42b and c, with the presence of satellites on the surface. Powder particles with irregular shapes are also present (Figure 42c).
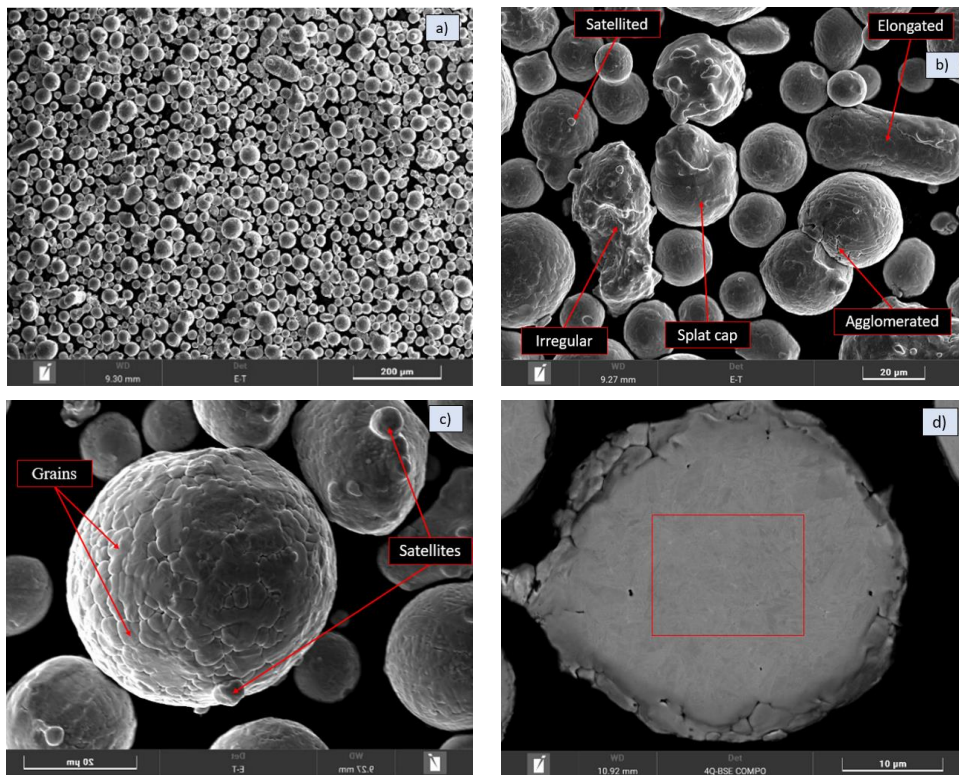
Figure 42: S2 powders a), b), c) S2 powders morphology; d) S2 particle cross section

To evaluate the composition of the initial microstructure and compare it with the datasheet in Annex 1, EDS analysis is used on the cross section of powders as shown in Figure 42d, and the result is resumed in Table 14.

Table 14: Atomic [%] composition of S2 powders

% Atom	Carbon	Silicon	Manganese	Iron	Molybdenum
S2	$22,05 \pm 3,04$	$2,28 \pm 0,15$	$0,54 \pm 0,08$	$74,91 \pm 2,98$	$0,24 \pm 0,01$

An EBSD was performed in order to complete the characterization, determining the phases present into the original S2 powder microstructure. The EBSD was carried out on the area shown in Figure 43a. The pattern quality (Figure 43b) ensure good results on the bright zones that coincide with the cross sections of S2 particles. The analysis of the crystal lattice revealed the presence of ferrite as shown in the phase map in Figure 43c.
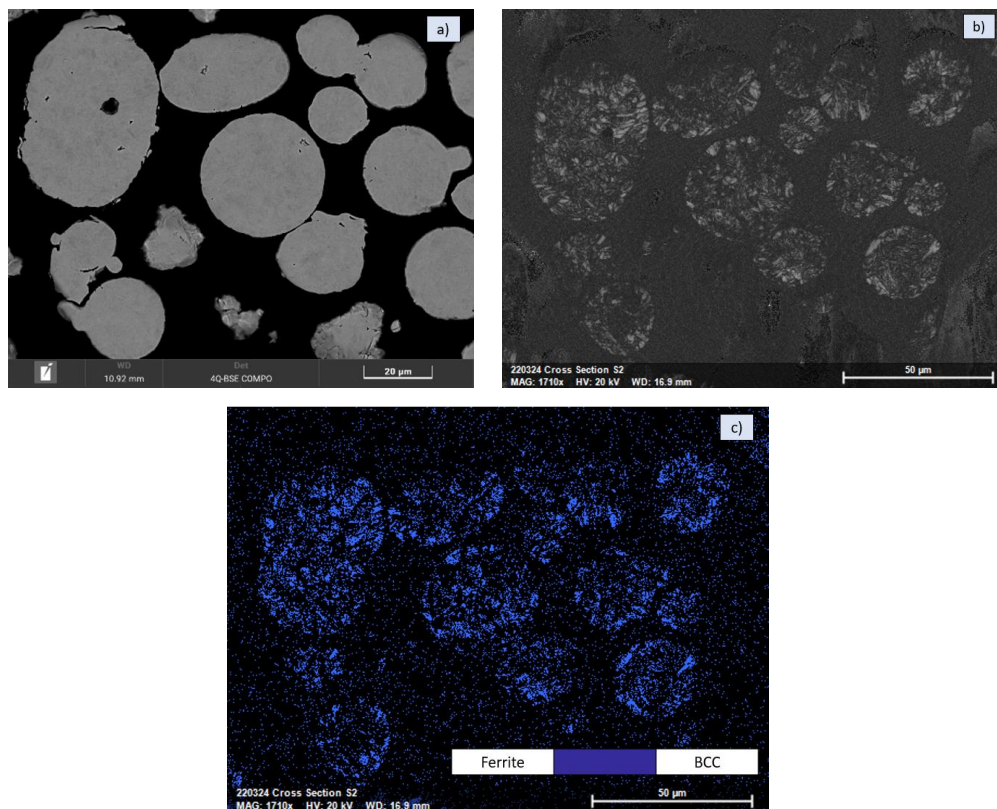
Figure 43: EBSD on S2 powder cross section. a) EBSD area b) Pattern quality c) Phase map

4.1.1.2 Silicon Carbide powder

The morphology, particle size distribution and composition of SiC powders are evaluated using SEM, granulometry analysis and EDS to compare the result with the datasheet in Annex 1 and

confirm the information. The morphology is confirmed to be irregular with particle size distribution similar to the results in, and the concentration is approximately the same (Table 15).
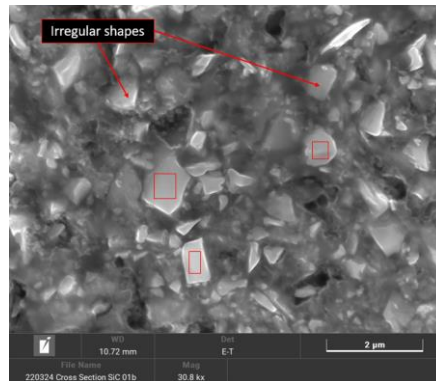
Figure 44: Morphology of SiC powders

Table 15: Atomic [%] concentration of SiC powders

% Atom	Carbon	Oxygen	Silicon
SiC	**72,67** ± 1,42	**3,07** ± 0,20	**24,26** ± 1,48

4.1.2 Milled powders

In this study. Three different mixing methods are tried to obtain the best properties of the mixtures for the printing through SLM. The milling was performed on S2 + 15% (in volume) of SiC and on SiC powder as explained in chapter 3.5. In this chapter microscope observations were performed on two of the three batches: ball milling S2 + 15% (in volume) of SiC and ball milling S2 + 15% (in volume) of pre-milled SiC.

4.1.2.1 Ball milling

- SiC powder

The milling was stopped after each run for a break time of 15min, during which, a small quantity of SiC were withdrawn to be checked with SEM.

After 30min of milling, only few granules break as can be observed in Figure 45a and b. After 1 hour, on the surface of the powders batch within the milling bowl (Figure 45c), areas with compact SiC appear. SEM micrographs (Figure 45d and e) still reveal the presence of intact SiC granules, but some of these granules start smashing as shown in Figure 45d, especially the bigger ones (Figure 45e). After 1h 30 the amount of compact areas of SiC on the surface of the powders batch increase (Figure 45f), as well as the amount of granules that are partially smashed, in terms of total amount

and relative volume of a single granule (Figure 45g). The compact areas of SiC are composed by the primary SiC particles that compact during the ball milling, due to the interaction with the WC balls.
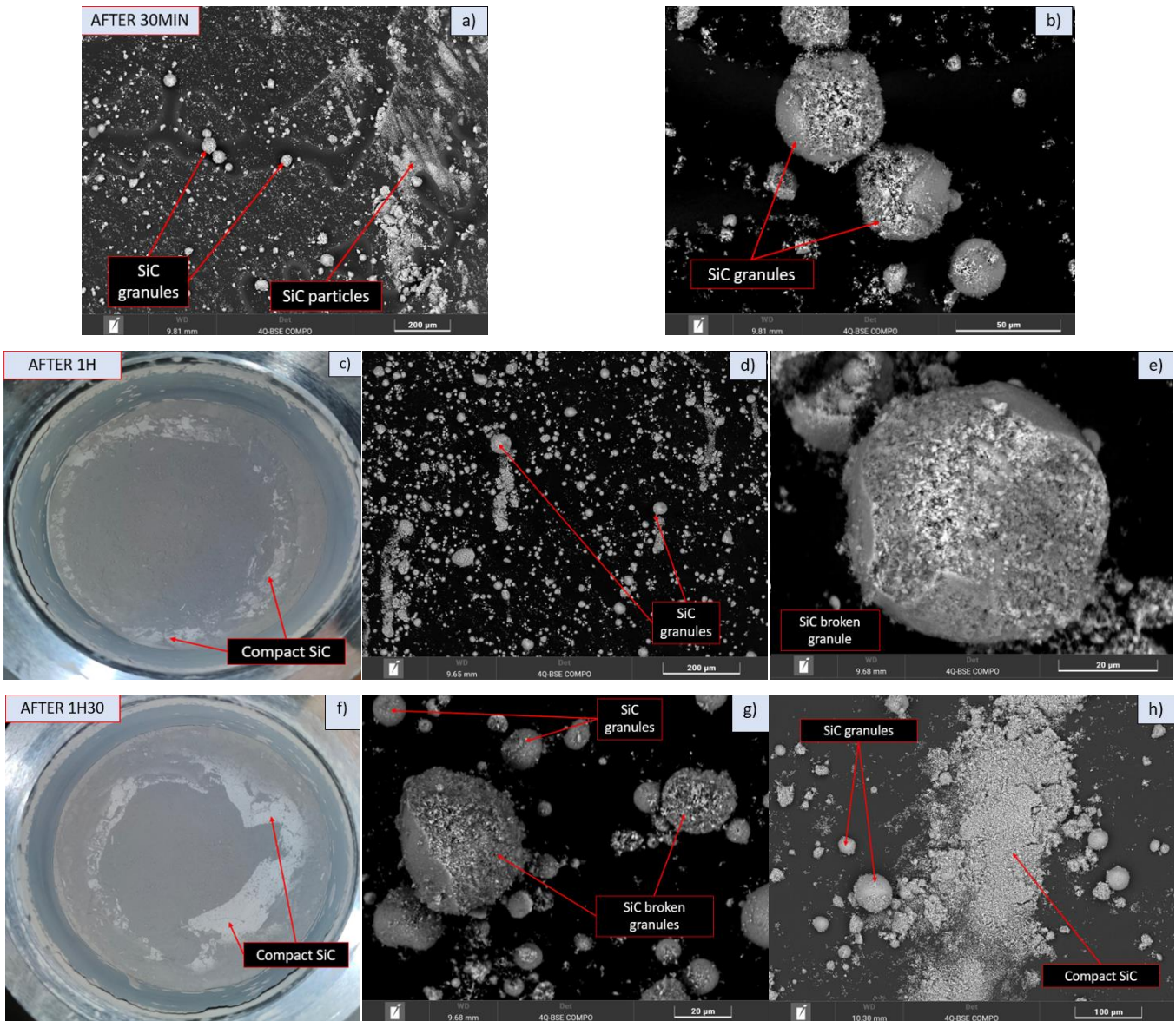
Figure 45: Observations of SiC powder after each ball milling stop

- Ball milling S2 + 15% (in volume) of SiC powder

After 30min of ball milling, at glance, it is possible to observe a level of heterogeneity of the mix in the ball milling bowl (Figure 46a). In Figure 46b and c, the heterogeneity of the mixing was evident, in fact, the two powders can be distinguished in the bowl. Some SiC particles better adhere on S2 in the regions characterized by an irregular shape (Figure 46c). The SiC granules were still present and did not break during the milling.

After 1h of ball milling, many SiC granules are present on the surface of the powders batch due to the heterogeneity of the mixture (Figure 46d). A similar situation to the mixture after 30min was observed (Figure 46e). In this case too, the SiC particles mainly adhere on the irregular surface zones of the S2 powders, with the presence of intact SiC granules around. At higher magnification (Figure 46f), some deformed and fractured S2 particles are observed. These phenomena create some flattened areas, which facilitate the adhesion of SiC. EDS analyses were performed in order to determine any presence of Oxygen on the surface of the powders. The results in Table 16 show the presence of Oxygen, but the amount is negligible.

As observed in Figure 46g, after 2h of ball milling the amount of SiC segregation on the surface increase. Compared to 1h of ball milling, more SiC granules break The adhesion, as can be observed on Figure 46i, is better on these irregular areas compared to spherical areas. EDS analysis (Figure 46i) doesn't reveal high oxygen content (Table 17).

After 4 hours, some flakes of compact SiC appear on the container surface (Figure 46j). The observation at SEM did not show an improvement of homogeneity of adhesion on most of S2 particles (Figure 46k). Crucial details that were revealed in Figure 46l is the deformation of S2 particles surfaces and the detachment of satellites in many particles. These two new phenomena are indications that the milling time were becoming excessive.

After 6 hours, consistently with the results obtained after each stop, the number of segregations on the container surface increase (Figure 46m). At SEM, it was observed that the adhesion of SiC on S2 surfaces barely increase with the appearance of these big SiC agglomerates that trapped S2 particles inside (Figure 46n). Many S2 particles were deformed and lose the satellites present on the surface. Some S2 particles were fractured during the interaction with WC balls. This phenomenon increases the amount of SiC that adhere on surface.
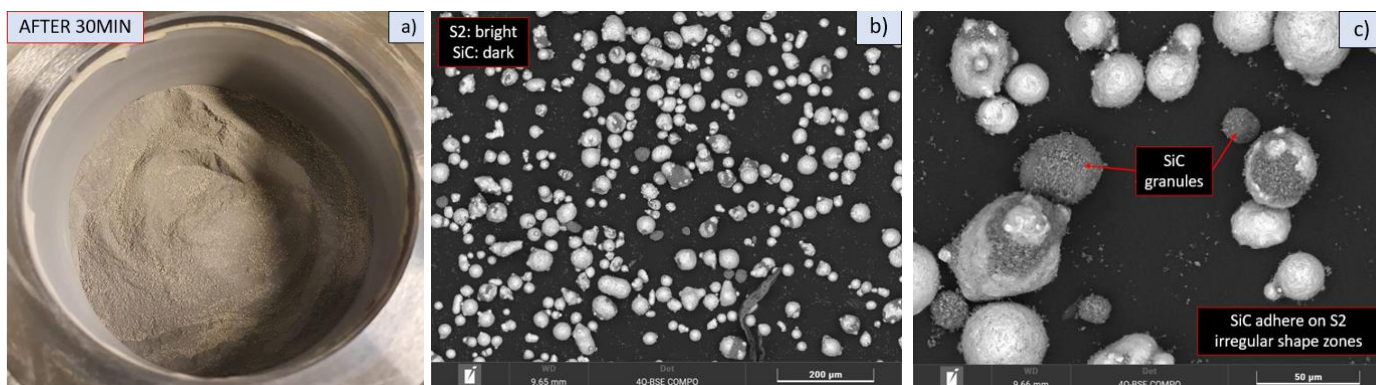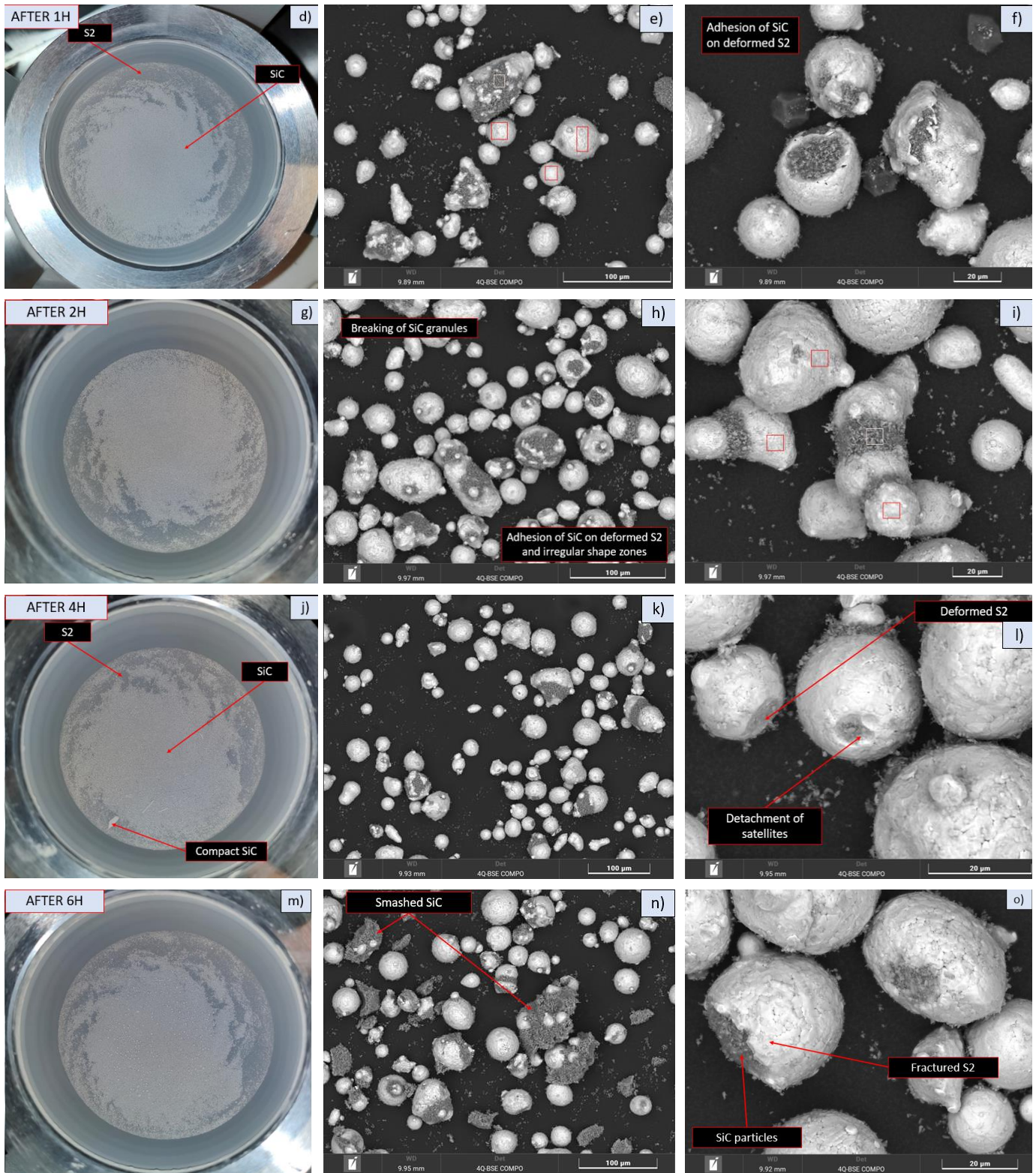
Figure 46: Observations of S2+15% (in volume) of SiC after each stop

Table 16: Atomic [%] composition of S2 and SiC particles in the mixture after 1h of ball milling

% Atom	Carbon	Oxygen	Silicon	Manganese	Iron	Molybdenum
S2	$33,43 \pm 1,32$	$2,08 \pm 0,92$	$6,73 \pm 3,18$	$0,31 \pm 0,05$	$57,24 \pm 3,64$	$0,22 \pm 0,07$
SiC	51,09	1,36	45,73	0	1,79	0,02

% Atom	Carbon	Oxygen	Silicon	Manganese	Iron	Molybdenum
S2	$33,44 \pm 9,35$	$2,27 \pm 0,37$	$5,11 \pm 0,72$	$0,32 \pm 0,06$	$58,66 \pm 10,15$	$0,21 \pm 0,10$
SiC	52,79	1,84	44,55	0	0,82	0

- Ball milling S2 + 15% (in volume) of pre-milled SiC powder

The aim of this preparation method is to mix the S2 powders with an already broken granules of SiC. For this, S2 is mixed with a milled SiC with the parameters described in Table 12 for 1h30min. The process, as usually, were stopped after each stage for a break time of 15 min.

After 30 minutes of milling, the heterogeneity of the mix could be observed on the milling container (Figure 47a) and at SEM (Figure 47b and c). The agglomerates appear on the bowl surface as it happened with the ball milling of S2 + 15% (in volume) of SiC. At SEM, the granules that resist to the ball milling of SiC alone and of the mixture were visible. The adhesion of SiC particles is better in the irregular shape areas of the S2 surfaces.

The number of agglomerates on the surface of the bowl increased (Figure 47d). After 1h, some S2 particles were deformed, and the detachment of satellites can be observed (Figure 47e and f).

After 1h30min, on the bowl surface, in addition to the increase of the amount of SiC agglomerates, some compact SiC appear (Figure 47g). Looking at SEM, the homogeneity of the mixture seems to not undergone an improvement, and some granules can still be observed as in Figure 47h. Making a zoom on a single S2 powder, in Figure 47i, it can be observed some SiC particles on the surface. The same phenomenon was observed in all the samples taken after each stop. The level of adhesion differs too much locally on a single S2 powder and in all the mixture.
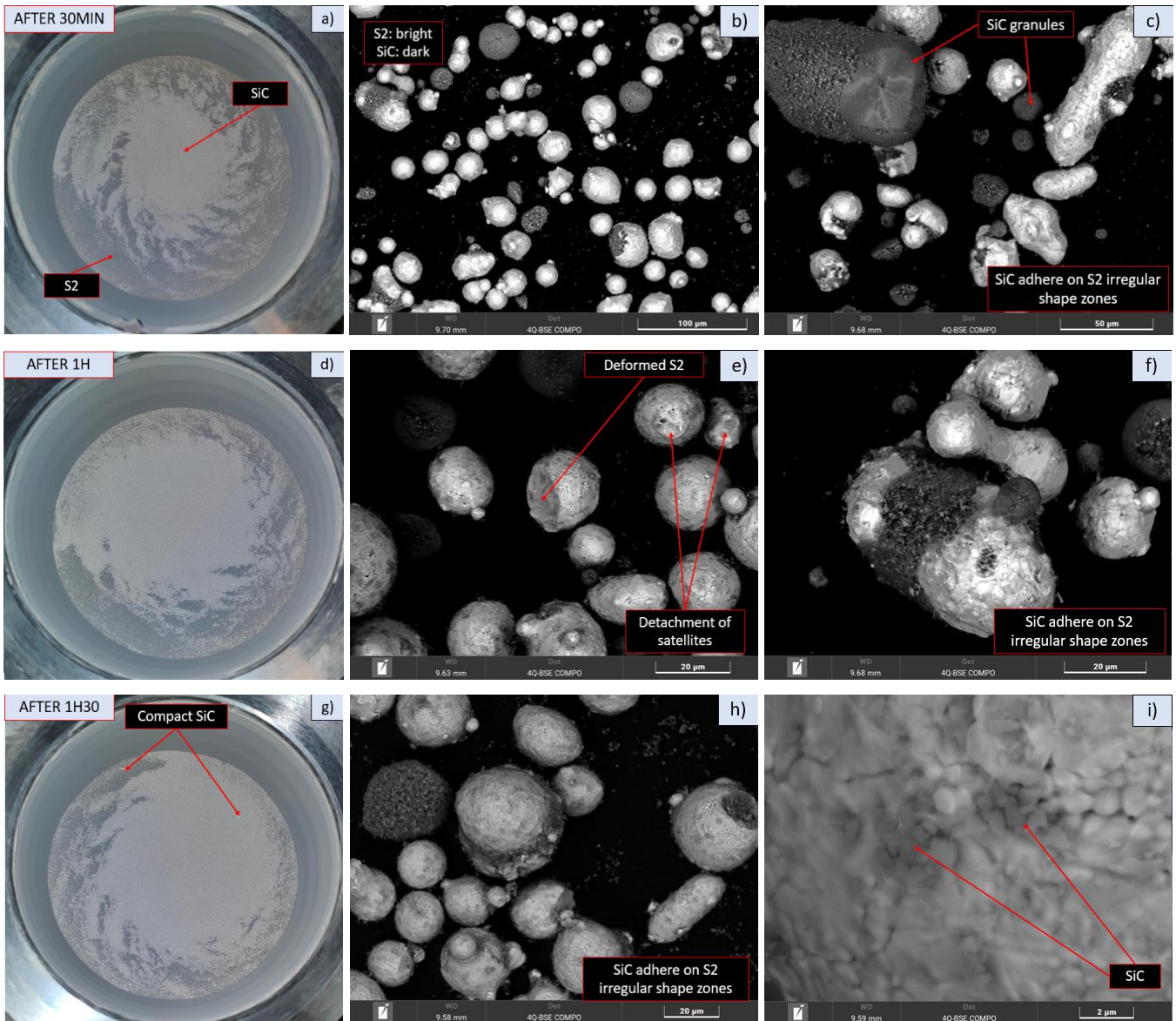
Figure 47: Observations of S2+15% (in volume) of pre-milled SiC after each stop

4.1.2.2. Rheological properties

In chapter 2.1.2.2, the properties necessary to understand the rheological properties of the powders are explained. The tap density and the cohesive index are evaluated to have an idea about the rheological properties of S2 powders, and to compare the behaviour of S2 with the different batches of S2 + 15% (in volume) of SiC prepared with the three different methods. The manual mixing seems to be homogeneous, more homogeneous compared to what has been seen at glance for the other two methods (Figure 48). The GranuPack and GranuDrum were performed with the same parameters described in chapter 4.1.2.2. The results of GranuPack are resumed in Figure 49 and Table 18 for the two different runs to minimize the error due to the operator that performed the test

In Table 18, some properties related to rheological properties (density variation with taps, Hausner ratio, Carr's index) are evaluated.
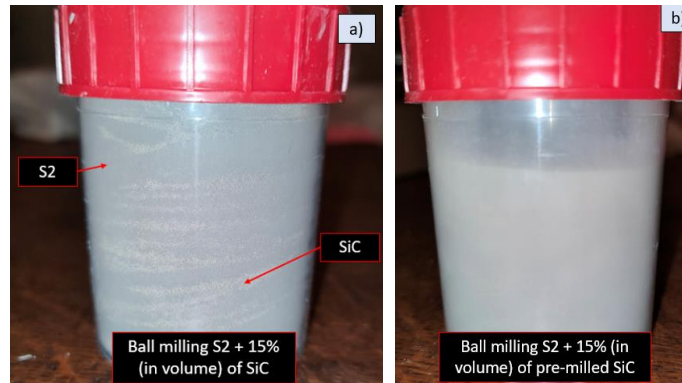
Figure 48: Batches for GranuPack and GranuDrum tests
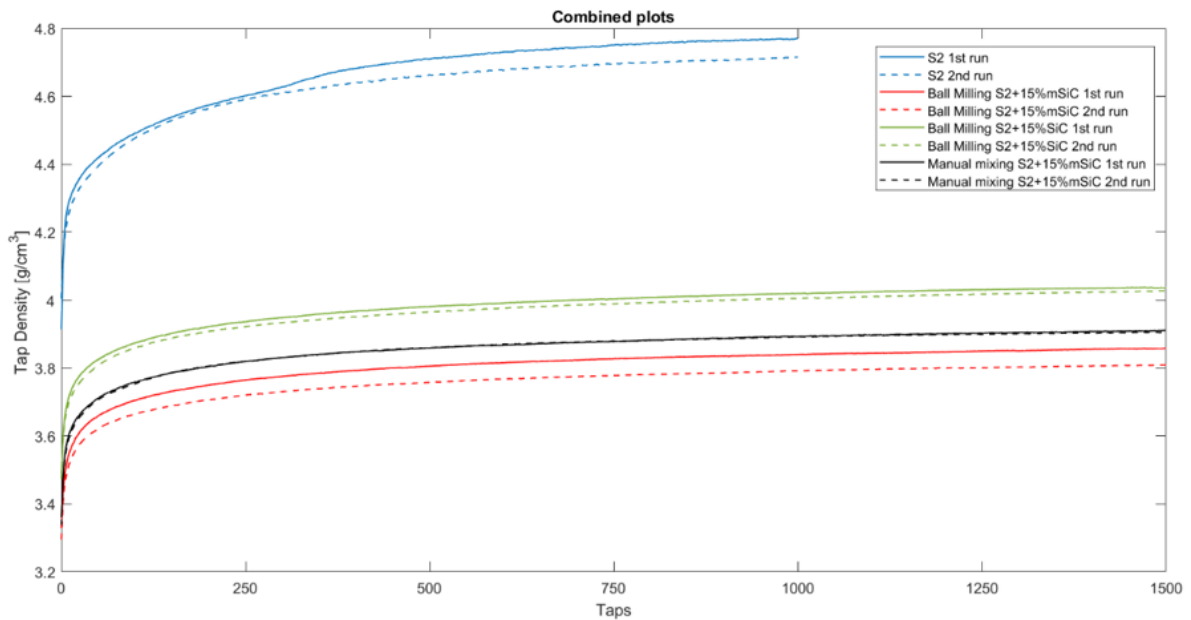
Figure 49: Tap density evaluation

Table 18: Tap density results

Name	Number of taps n	$\rho(0)$ (g/ml)	$\rho(n)$ (g/ml)	Hausner ratio	Carr's index	α (g/l)
S2	1000	3,959	4,743	1,20	16,51	32
BallMilling_S2+15% (in volume) of pre-milled SiC	1500	3,312	3,833	1,16	13,60	21,9
BallMilling_ S2+15% (in volume) of SiC	1500	3,481	4,032	1,16	13,67	22,7
ManualMixing_ S2+15% (in volume) of pre-milled SiC	1500	3,349	3,909	1,17	14,31	25,2

In Figure 50, the cohesive index follows a shear thickening behaviour for the original S2 powder, while a shear thinning behaviour is observed for the manual mixing. The trend of the cohesive index is more or less constant for the two mixtures prepared by the other two methods.
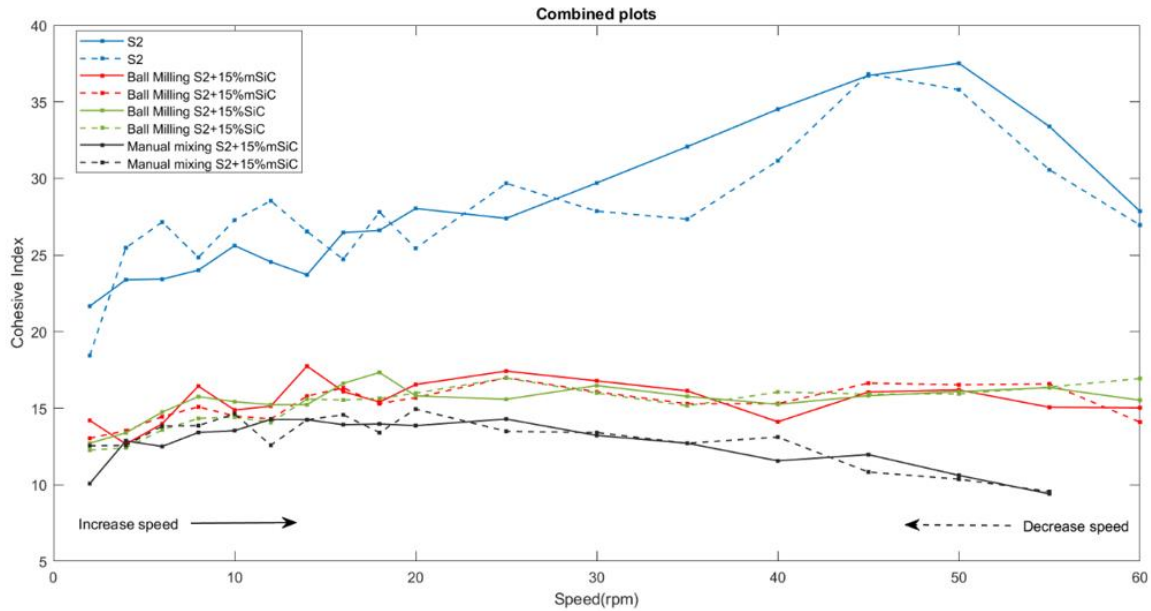
Figure 50: Cohesive index evaluation

An XRD analysis is provided on the original powders and on the three batches prepared as shown in Figure 51. The test reveals a martensitic microstructure of the S2 powder, while the alpha-SiC phase is determined into the microstructure of SiC powder. The peaks related to these two phases are evidenced in the graphs of the three batches of S2 + 15% SiC.
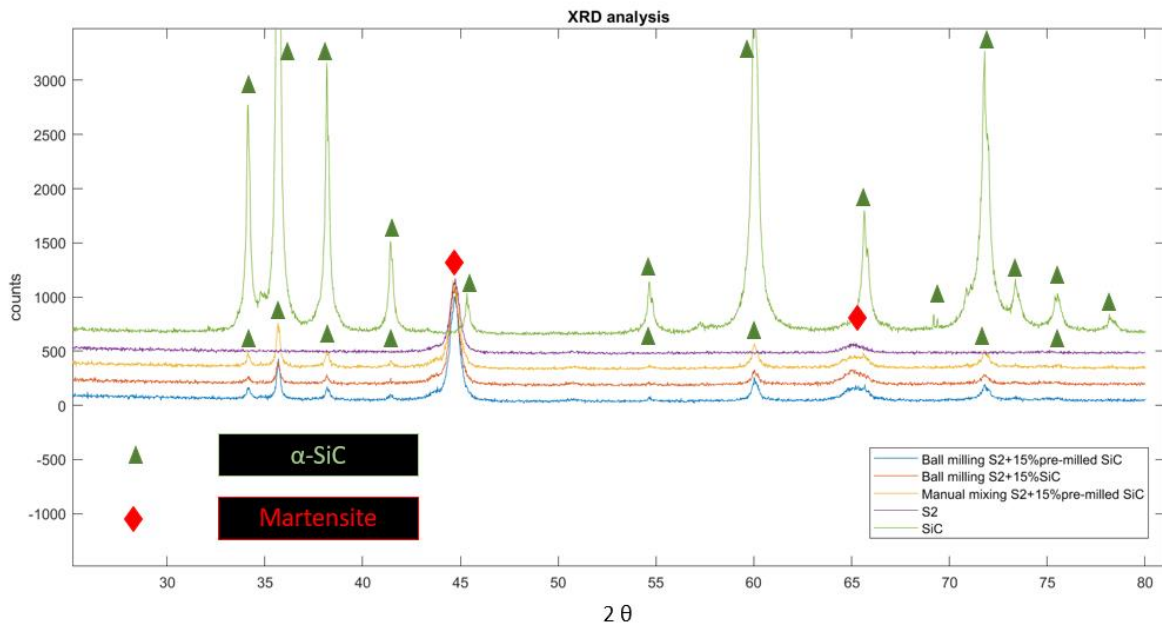
Figure 51: Results of XRD analysis

4.1.3 Summary of the results

The three different methods performed are described in chapter 3.2.2.2. Two of these three methods include a ball milling process. The aim of using this process is to break the granules of SiC powder and provide to a mechanical alloying of S2 and SiC powders reaching a homogeneous mix. The low level of oxygen content and the absence of alteration of the phases after performing the mixing methods, both confirmed by the EDS (Table 16 and Table 17) and XRD analysis (Figure 51) were useful to conclude that the mixing methods adopted avoid these problems. To determine the effectiveness of the methods adopted, observations at SEM were performed on aliquots at different times as presented in chapter 4.1. A ball milling time greatly influence the effectiveness of the methods.

The heterogeneity of the mix in all the batches even after 6 hours of ball milling performed as first method on S2 + 15% (in volume) of SiC powder with 1:5 balls to powder weight ratio. Moreover, the time was also too long because it causes the deformation of the S2 particles and the break of satellites on S2 particles without significantly increase the homogeneity of the adhesion of SiC on S2 particles surfaces. Such a long time also causes agglomerations of SiC powder that trap inside some S2 particles. So, to evaluate the rheological properties of the mixture, the ball milling time was set at 2 hours because it ensures a decent homogeneity of the mix with only few remained granules of SiC and without evident deformation of S2 particles. The last two methods use a pre-milled SiC powder prepared with ball milling with 1:3 balls to powder weight ratio for 1h30min. This SiC ball milling time was chosen because at higher time, more compact SiC powder was generated and would not have favoured an adequate mixing with S2 powder. One method consists into the ball milling of S2 powder with 15% in volume of pre-milled SiC powder performed for 1h30min resulting on the best time for the same reason of the previous method. The last method is a manual mixing of the S2 powder with the pre-milled SiC.

4.2 Differential Thermal Analysis

Different DTA were performed at different volumetric concentration SiC and two different cooling rates (Table 13).

4.2.1 S2

Figure 52 shows the heating and the cooling curves of the DTA performed on S2 powders.
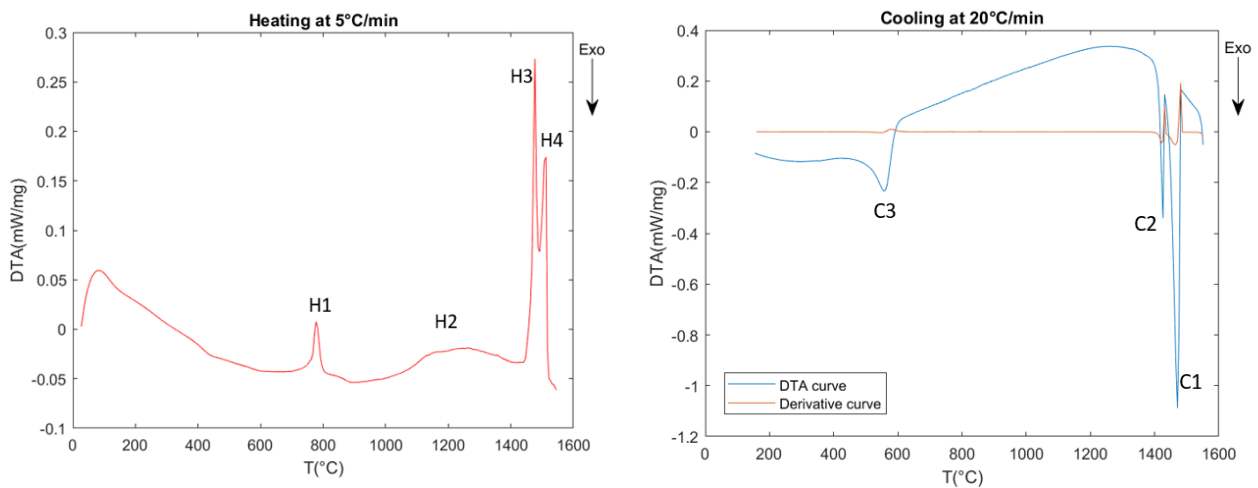
Figure 52: DTA curves for S2 powders. a) Heating curve b) Cooling curve

The meaning of the principal peaks evidenced in the heating and cooling curves are respectively resumed in Table 19 and Table 20.

Table 19: Principal heating peaks for S2 powder

Peak	Start Temperature [°C]	End Temperature [°C]	Reaction or phase transformation
H1	750	820	Bainite/Martensite to Austenite
H2	1050	1400	Sintering of powders
H3	1450	1490	Austenite to δ-Ferrite
H4	1500	1530	δ-Ferrite to liquid

Table 20: Principal cooling peaks for S2 powder

Peak	Start Temperature [°C]	End Temperature [°C]	Reaction or phase transformation
C1	1500	1450	Liquid to δ-Ferrite
C2	1050	1400	δ-Ferrite to Austenite
C3	1450	1490	Widmanstätten solidification

The microstructure obtained after DTA (Figure 53) is typical of the Widmanstätten solidification, on which the pro-eutectoid phase (ferrite or cementite depending on the carbon content of the steel) separates not only along the grain boundaries of austenite, but also inside the grains along certain crystallographic planes (octahedral planes) and direction in the shape of plates, or needles forming mesh-like arrangement [79].
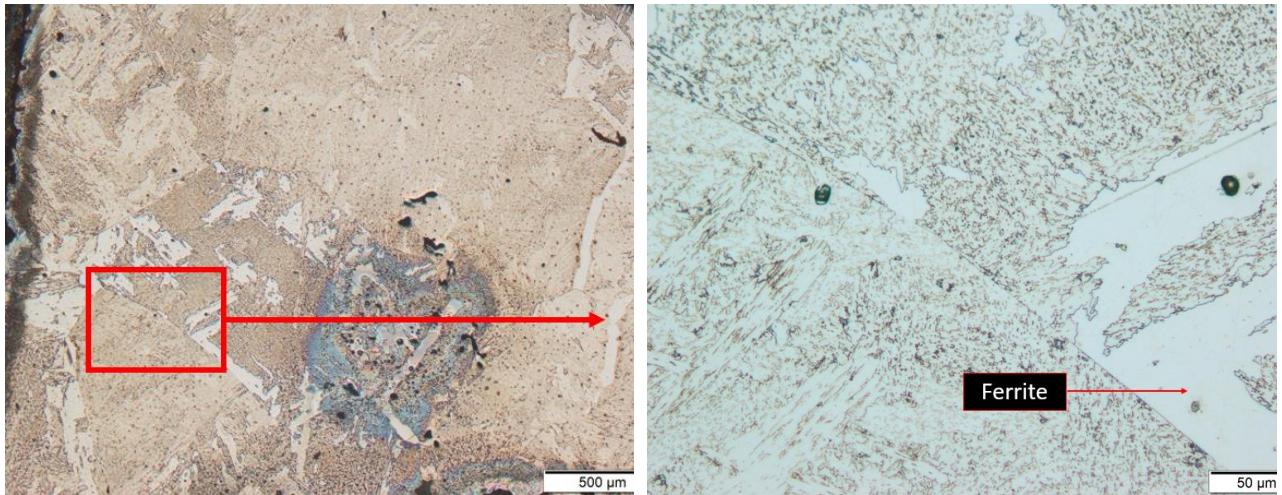
Figure 53: Optical Microscope observation of S2 etched sample with 3% Nital after DTA test

4.2.2 S2 + 5% (in volume) of SiC powder

The heating and cooling curves of the DTA test are illustrated in Figure 54. In Table 21 and Table 22, the meaning of the principal peaks in heating and cooling curves are resumed.
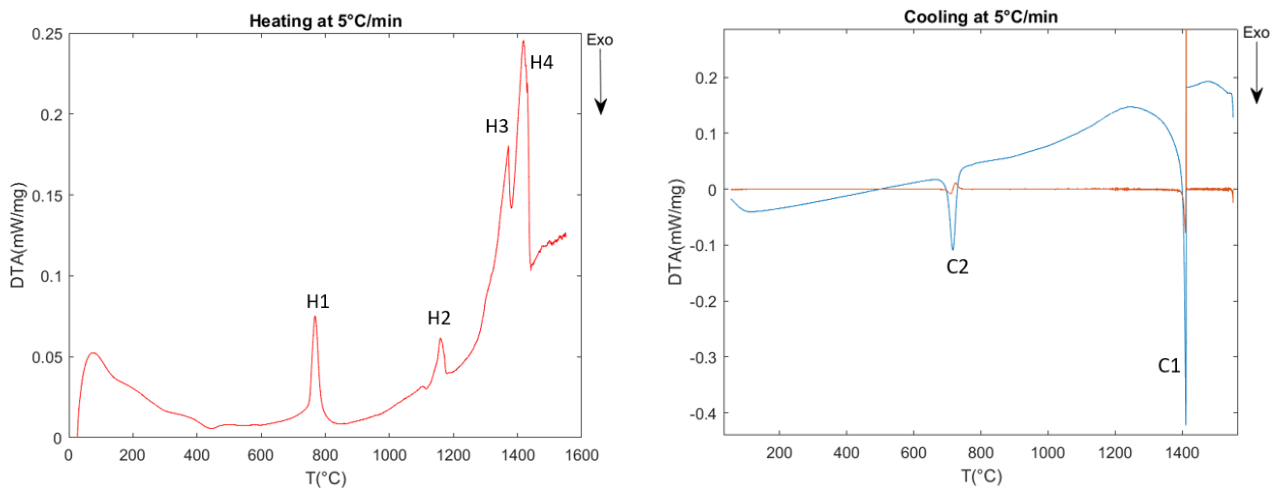
Figure 54: DTA curves for S2+5% (in volume) of SiC powder. a) Heating curve b) Cooling curve

Peak	Start Temperature [°C]	End Temperature [°C]	Reaction or phase transformation
H1	760	800	Bainite/Martensite to Austenite
H2	1050	1200	Sintering of powders
H3	1350	1390	Austenite to δ-Ferrite
H4	1400	1430	δ-Ferrite to liquid

Table 22: Principal cooling peaks for S2+5% (in volume) of SiC powder

Peak	Start Temperature [°C]	End Temperature [°C]	Reaction or phase transformation
C1	1420	1370	Liquid to Austenite
C2	760	680	Austenite to Pearlite

In Figure 55a, the phases present in the microstructure were not completely defined. After an etching with 3% Nital, the microstructure reveals a fully pearlitic matrix (Figure 55b) with the presence of very few Iron/Molybdenum carbides as highlighted in Figure 55a and d.
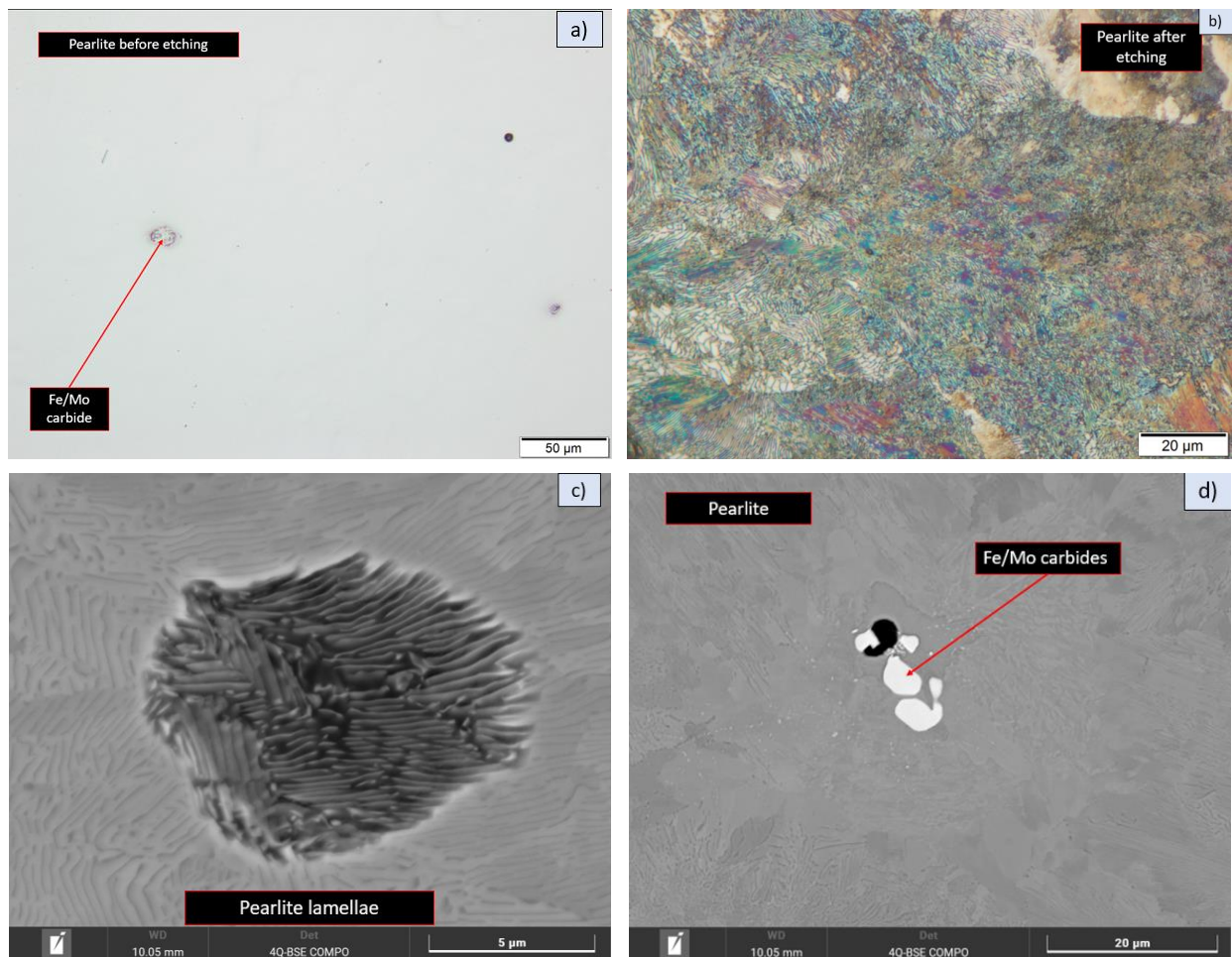
Figure 55: Microscope observations of S2+5% (in volume) of SiC powder after DTA test. a) OM observation before etching b) OM observation after etching with Nital c-d) SEM micrographs

The composition of the cementite that composed the pearlite is resumed in Table 23.

Table 23: Atomic [%] composition of the pearlite in S2+5% (in volume) of SiC powder at 5°C/min of cooling rate

%Atom	Carbon	Silicon	Manganese	Iron	Molybdenum
Pearlite	**31,00** ± 3,06	**3,29** ± 0,65	**0,31** ± 0,11	**65,25** ± 3,40	**0,16** ± 0,04

4.2.3 S2 + 10% (in volume) of SiC powder

The heating and cooling curves of DTA test are respectively shown in Figure 56 and Figure 57 and the respective meaning of the principal peaks are resumed in Table 24 and Table 25.

Figure 56: DTA heating curve for S2+10% (in volume) of SiC powder

Table 24: Principal heating peaks for S2+10% (in volume) of SiC powder

Peak	Start Temperature [°C]	End Temperature [°C]	Reaction or phase transformation
H1	750	820	Bainite/Martensite to Austenite of S2 powders
H2	1020	1520	Sintering of powders + Reverse peritectic transformation

The complex peak H2 is referred to the sintering of the powders together with the reverse peritectic transformation that occurs at higher temperature. Looking at the heating curve in Figure 56, it was impossible to dissociate these two phenomena, so the range of temperature and the phenomena that occur are combined (Table 24).

Figure 57: DTA cooling curve for S2+10% (in volume) of SiC powder at 5°C/min and 20°C/min of cooling rate

Table 25: Principal cooling peaks for S2+10% (in volume) of SiC powder of 5°C/min and 20°C/min of cooling rate

Peak	Start Temperature [°C]	End Temperature [°C]	Reaction or phase transformation
C1	1320	1220	Liquid to Austenite
C2	1170	1090	Eutectic Fe/Mo carbides
C3	820	?	Austenite to α-Ferrite
C4	?	700	Magnetic transition of α-Ferrite

At first glance, looking at the overviews of the microstructure obtained at Optical Microscope (Figure 58a), the presence of graphite type E was observed (types D and E are very similar and vary in amount and dimension of graphite, and hard to distinguish). The same observations were done for the S2 + 10% (in volume) of SiC at 20°C/min of cooling rate (Figure 58b) and the columnar dendrites can be observed. The columnar growth started from the zone in contact with the crucible to the inner part of the liquid. In addition to graphite and Fe/Mo carbides, Discontinuous Cellular Precipitates (DCP: Troostite) were also observed near the Fe/Mo eutectic carbides as shown in Figure 58e and f [80]. The composition of DCP was performed and evaluated using EDS, and the result is resumed in Table 27.

Figure 58: Microscope observations of S2+10% (in volume) of SiC. a-c-e) After DTA at 5°C/min of cooling rate. b-d-f) after DTA at 20°C/min of cooling rate

Table 26: Atomic [%] composition of the DCP phase in S2+10% (in volume) of SiC powder at 20°C/min of cooling rate

%Atom	Carbon	Silicon	Manganese	Iron	Molybdenum
DCP (Troostite)	**45,62** ± 8,39	**3,97** ± 0,94	**0,66** ± 0,13	**49,15** ± 7,40	**0,60** ± 0,13

The compositions of the phases present into the microstructures were evaluated using EDS. The results are shown in the following tables: Table 27 and Table 28.

Table 27: Atomic [%] compositions of different phases in S2+10% (in volume) of SiC at 5°C/min of cooling rate

%Atom	Carbon	Silicon	Manganese	Iron	Molybdenum
Fe/Mo carbide precipitates	**19,70** ± 2,63	**6,78** ± 0,48	**0,41** ± 0,05	**71,07** ± 3,05	**2,04** ± 0,74
Fe/Mo eutectic carbides	**43,24** ± 7,06	**6,01** ± 2,26	**0,35** ± 0,10	**27,63** ± 11,62	**22,26** ± 6,38
Matrix	**18,29** ± 2,04	**6,19** ± 0,52	**0,45** ± 0,13	**74,49** ± 2,29	**0,56** ± 0,79

Table 28: Atomic [%] compositions of different phases in S2+10% (in volume) of SiC at 20°C/min of cooling rate

%Atom	Carbon	Silicon	Manganese	Iron	Molybdenum
Fe/Mo eutectic carbides	**44,73** ± 10,94	**6,20** ± 2,78	**0,50** ± 0,17	**27,14** ± 12,61	**21,45** ± 5,08
Matrix	**22,74** ± 2,23	**4,93** ± 0,91	**0,71** ± 0,25	**71,00** ± 2,43	**0,62** ± 0,24

An EBSD was performed on S2 + 10% (in volume) of SiC. The pattern quality in Figure 59b is useful to understand if the EBSD analysis had a good result. The dark areas of the pattern quality represent the zones with a low quality/not attainable result due to the bad indexation of the lattice structure. The phase map mainly highlights the presence of a ferritic matrix, in addition of the confirmation of graphite presence with zero solutions of 12,2%. Figure 59e shows the grains with a misorientation angle between each other above 15°. The grains map, the misorientation angle distribution and the grains size distribution were obtained doing a post-processing after the EBSD.
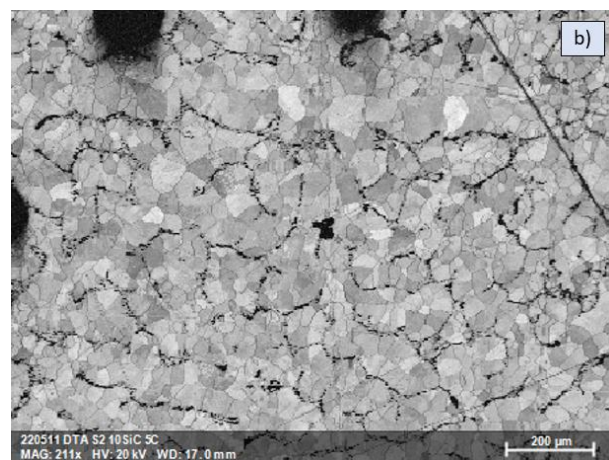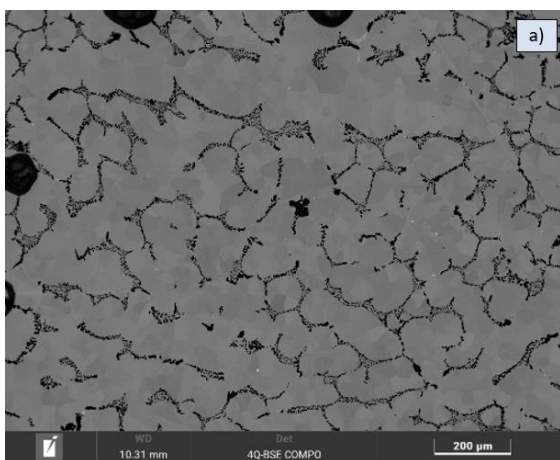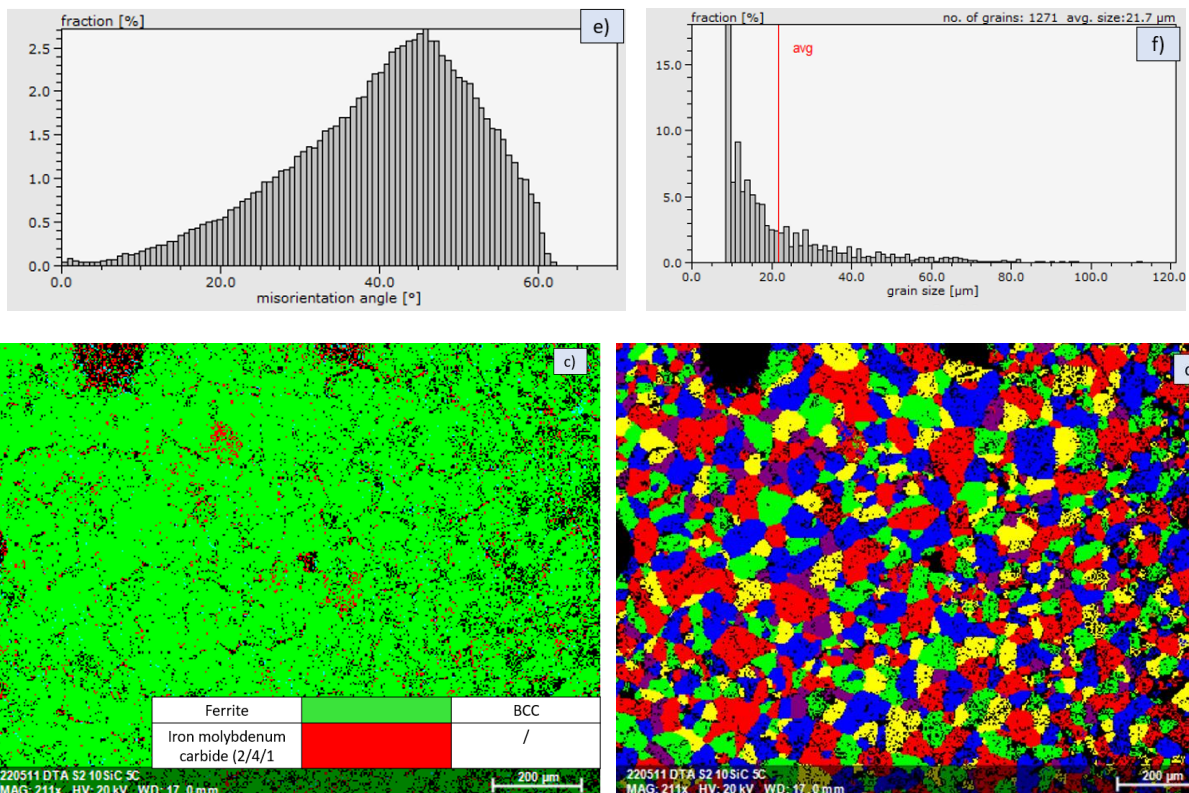
Figure 59: EBSD on S2+10% (in volume) of SiC at 5°C/min of cooling rate after DTA. a) EBSD area b) Pattern quality c) Phase map d) grains with misorientation above 15° e) Misorientation angle distribution f) Grains size distribution

Using Stream analysis software on the overviews of the two samples of the same mixture at different cooling rates, it was possible to do a quantification of the phases present into the microstructure. The phases revealed and coloured in red in Figure 60 encompass all the graphite and the different carbides, in other word, all the phases except the matrix. The results obtained are the percentages of these phases in the area delimited by the ROI 1 and are resumed in Table 29.
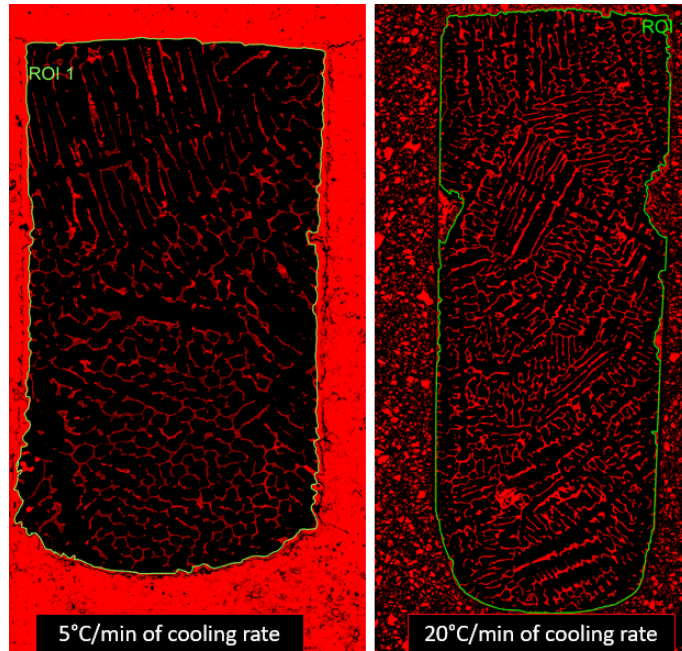
Figure 60: Quantification of the phases in the microstructure of S2+10% (in volume) of SiC

Table 29: Quantification of the phases of S2+10% (in volume) of SiC powder through Stream analysis software

S2 + 10% (in volume) of SiC	Quantification
5°C/min of cooling rate	8,45%
20°C/min of cooling rate	16,13%

4.2.4 S2 + 15% (in volume) of SiC powder

The DTA heating are illustrated in Figure 61. As explained for S2 + 10% SiC, the H2 peak combined the sintering of the powders and the reverse peritectic transformation. The cooling curve is visible in Figure 62.
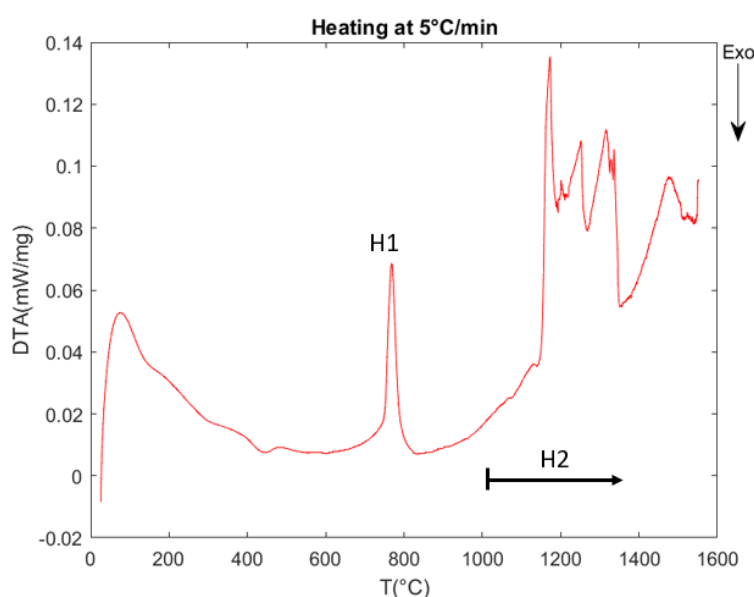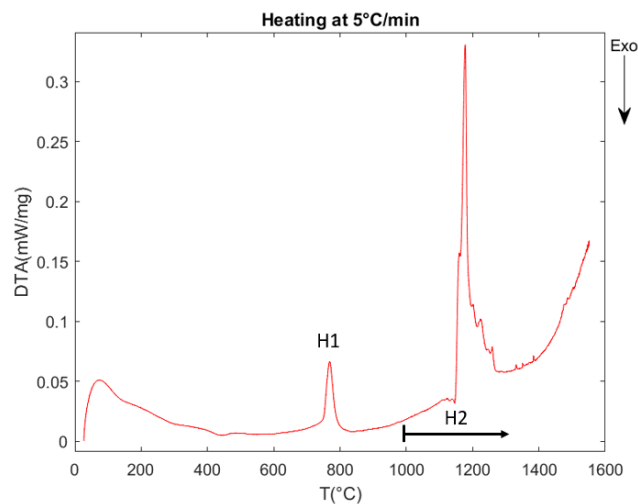

Figure 61: DTA heating curve for S2+15% (in volume) of SiC powder

Table 30: Principal heating peaks for S2+15% (in volume) of SiC powder

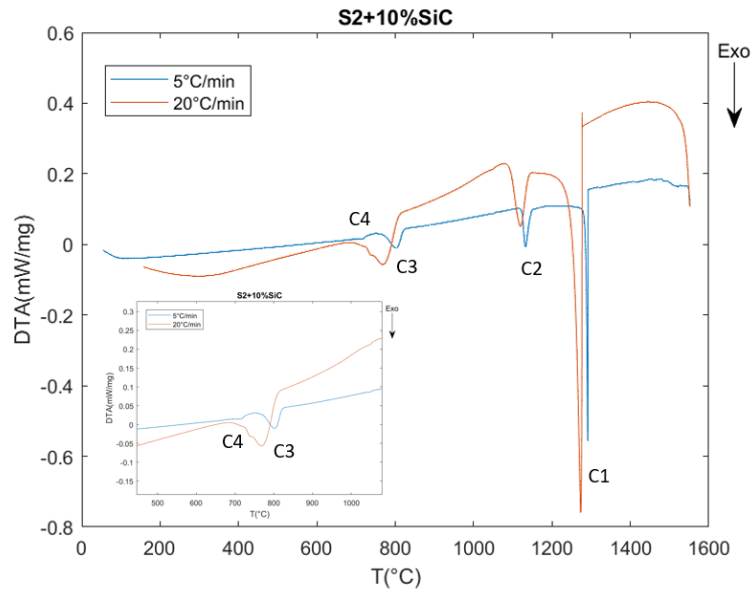| Peak	Start Temperature [°C]	End Temperature [°C]	Reaction or phase transformation
H1	750	820	Bainite/Martensite to Austenite of S2 powders
H2	1020	1520	Sintering of powders + Reverse peritectic transformation
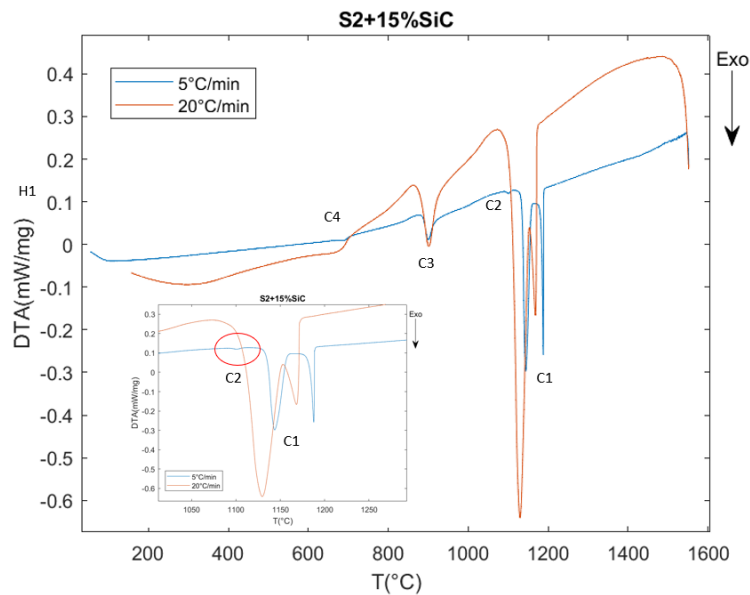
Figure 62: DTA cooling curve for S2+15% (in volume) of SiC powder at 5°C/min and 20°C/min of cooling rate

Table 31: Principal cooling peaks for S2+15% (in volume) of SiC powder of 5°C/min and 20°C/min of cooling rate

Peak	Start Temperature [°C]	End Temperature [°C]	Reaction or phase transformation
C1	1200	1090	Liquid to Austenite + eutectic Graphite
C2	1120	1070	Eutectic Fe/Mo carbides
C3	960	880	Austenite to α-Ferrite
C4	710	650	Magnetic transition of α-Ferrite

Optical Microscope observation (Figure 63) shows the presence of graphite D. Making a zoom on the microstructure, carbides can be observed (Figure 63c and d). The micrograph in Figure 63b shows the two different local microstructures obtained due to the heterogeneity of the liquids from which they were formed. After the first observations at Optical Microscope and SEM observations

(Figure 63e-h) that highlighted the morphology and the presence of the different phases, an etching with a solution with 3% Nital was done in order to obtain more information about the phases. After the etching, in Figure 63c, the grain boundaries were highlighted, and the ferritic matrix of the microstructure was confirmed.
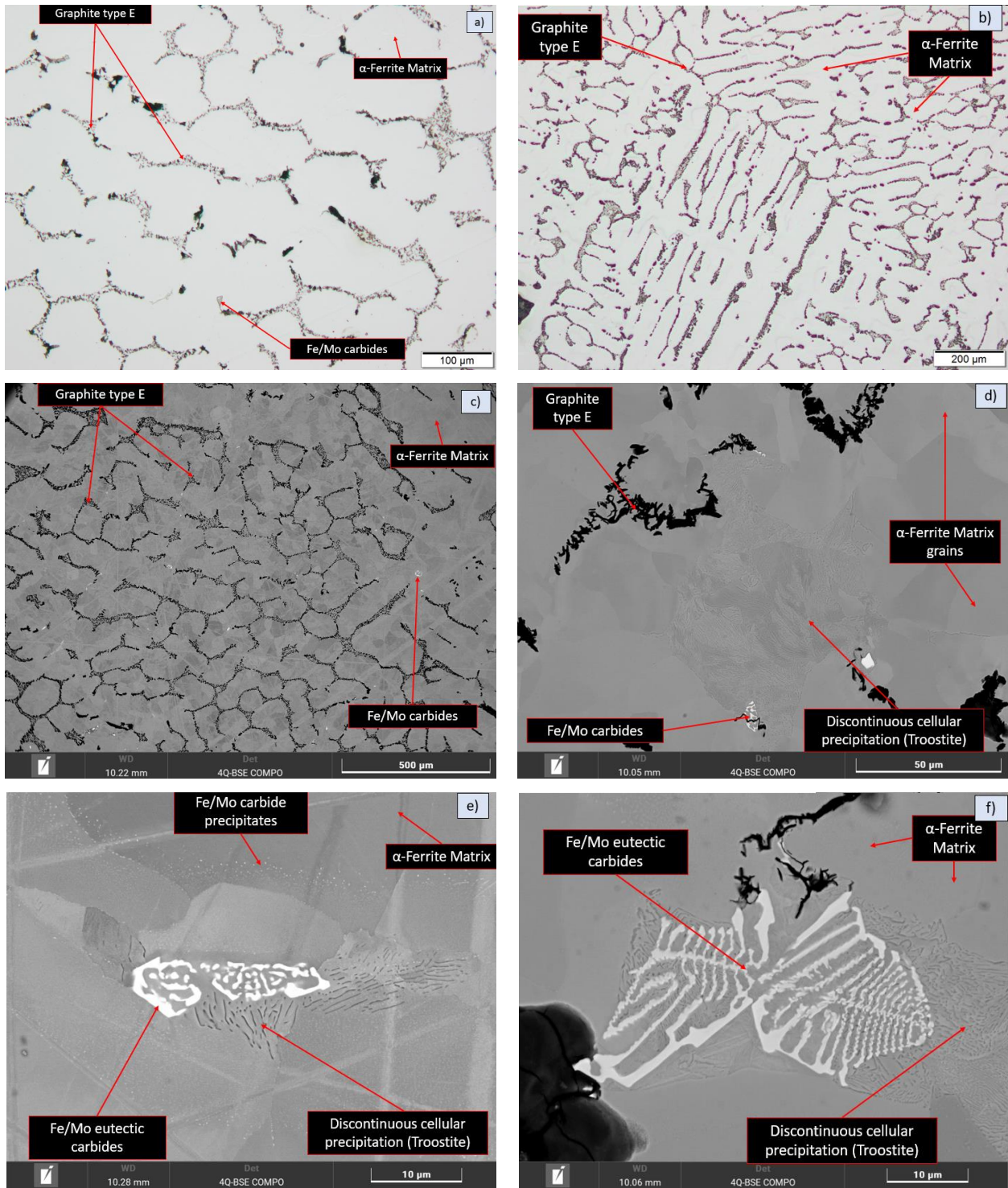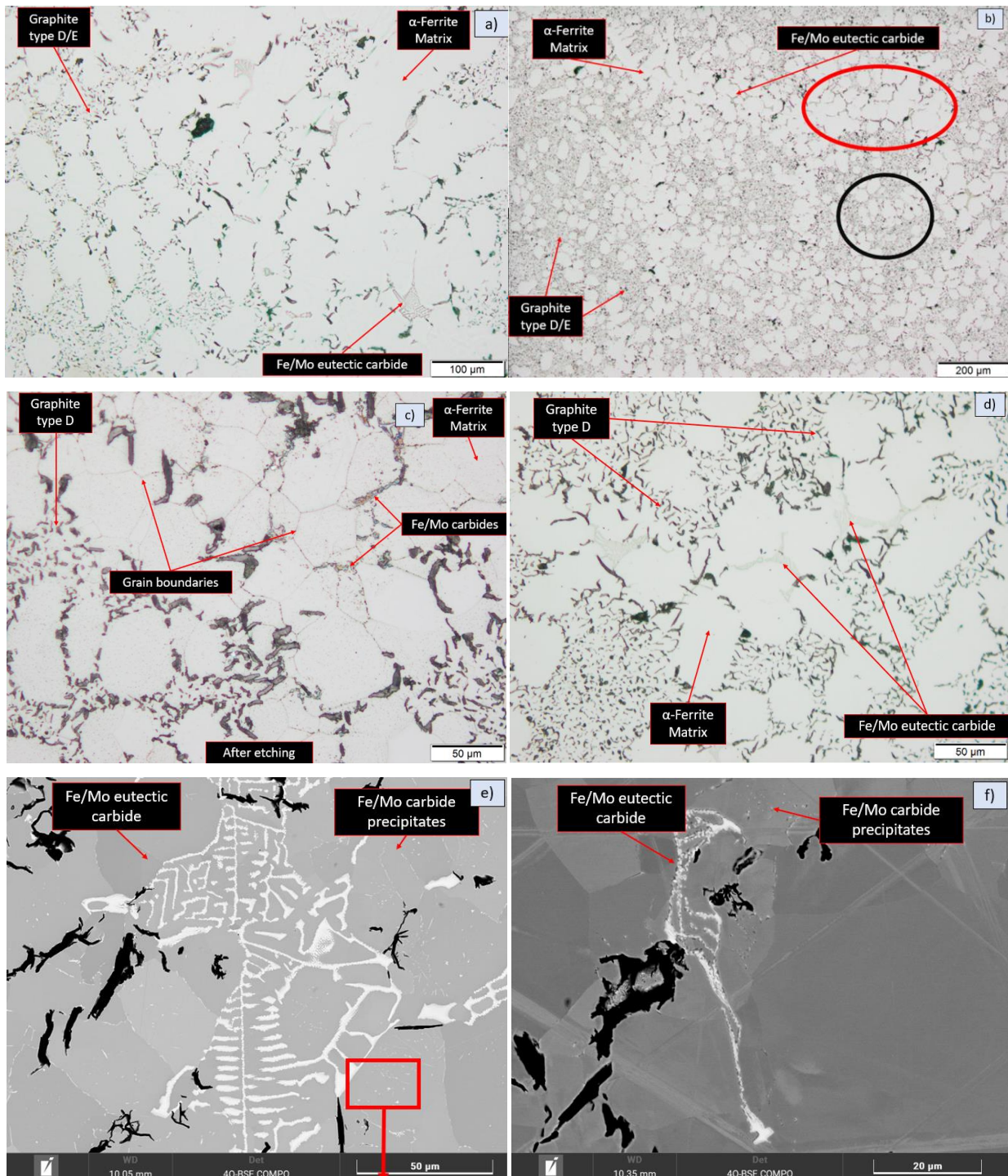
Figure 63: Microscope observations of S2+15% (in volume) of SiC. a-c-e-g) After DTA at 5°C/min of cooling rate. b-d-f-h) after DTA at 20°C/min of cooling rate

With the SEM in EDS mode, many compositions have been taken. The compositions in atomic percent of the various zones corresponding to the different phases are presented in Table 32 and Table 33 respectively for 5°C/min and 20°C/min of cooling rate during the DTA.

Table 32: Atomic [%] compositions of different phases in S2+15% (in volume) of SiC at 5°C/min of cooling rate

| %Atom	Carbon	Silicon	Manganese	Iron	Molybdenum
Fe/Mo carbide precipitates	$29,52 \pm 3,56$	$8,32 \pm 0,42$	$1,06 \pm 0,54$	$53,09 \pm 3,76$	$8,01 \pm 1,34$
Fe/Mo eutectic carbides	$40,56 \pm 1,97$	$8,92 \pm 0,58$	$0,54 \pm 0,13$	$30,50 \pm 2,70$	$19,49 \pm 1,31$
Matrix	$18,87 \pm 1,99$	$8,30 \pm 0,32$	$0,34 \pm 0,13$	$72,33 \pm 1,68$	$0,15 \pm 0,09$

Table 33: Atomic [%] compositions of different phases in S2+15% (in volume) of SiC at 20°C/min of cooling rate

%Atom	Carbon	Silicon	Manganese	Iron	Molybdenum
Fe/Mo carbide precipitates	$30,38 \pm 2,23$	$8,06 \pm 0,25$	$0,77 \pm 0,23$	$55,72 \pm 2,22$	$5,06 \pm 1,05$
Fe/Mo eutectic carbides	$38,82 \pm 1,77$	$8,52 \pm 0,49$	$0,51 \pm 0,06$	$37,14 \pm 3,85$	$15,00 \pm 6,31$
Matrix	$19,37 \pm 1,31$	$8,48 \pm 0,27$	$0,36 \pm 0,14$	$71,64 \pm 1,19$	$0,14 \pm 1,10$

An Electron Backscattered Diffraction (EBSD) was carried out as shown in Figure 64. The bright zone in the pattern quality (Figure 64b) confirm the accuracy of the results obtained. The phase map illustrated in Figure 64c was carried out with zero solutions of 9,3%. The matrix is fully ferritic, and the misorientation angle and grain size distributions were obtain in Figure 64e and f. The grains map shows the grains with a misorientation angle above 15°.

Figure 64: EBSD on S2+15% (in volume) of SiC powder at 5°C/min of cooling rate after DTA. a) EBSD area b) Pattern quality c) Phase map d) grains with misorientation above 15° e) Misorientation angle distribution f) Grains size distribution

A second EBSD was performed on the sample cooled at 20°C/min to evaluate the grain size distribution. The results is shown in Figure 65.
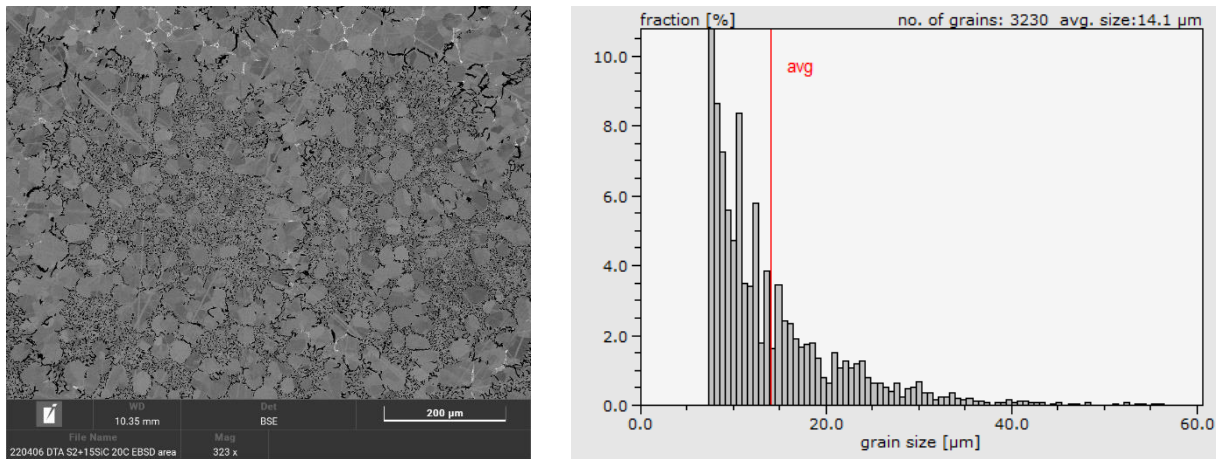
Figure 65: Grain size distribution of S2+15% (in volume) of SiC powder at 20°C/min of cooling rate. a)EBSD area. b) Grain size distribution

The quantification with Stream analysis software of the phases present into the microstructure for the two different cooling rates are reported in Figure 66 and the values in Table 34.
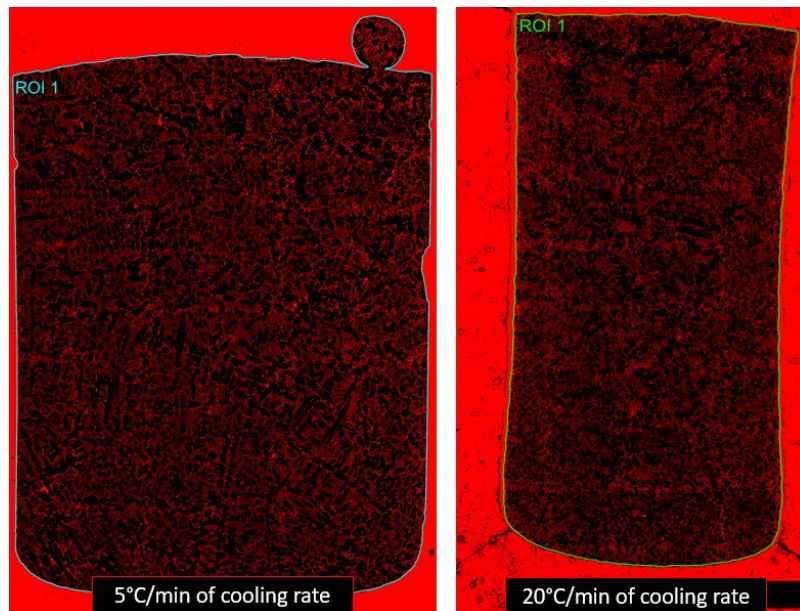
Figure 66: Quantification of the phases in the microstructure of S2+15% (in volume) of SiC powder

Table 34: Quantification of the phases of S2+15% (in volume) SiC powders of through Stream analysis software

S2 + 15% (in volume) of SiC	Quantification
5°C/min of cooling rate	18,04%
20°C/min of cooling rate	20,25%

4.2.5 S2 + 20% (in volume) of SiC powder

Two different thermal cycles were provided for this mixture. One is the DTA that ensure the complete fusion of S2 and complete dissolution of SiC powders, and the other one is the DTA stopped during the sintering phenomenon.

- Single cycle DTA

DTA heating and cooling curves are visible in the next figures (Figure 67 and Figure 68).
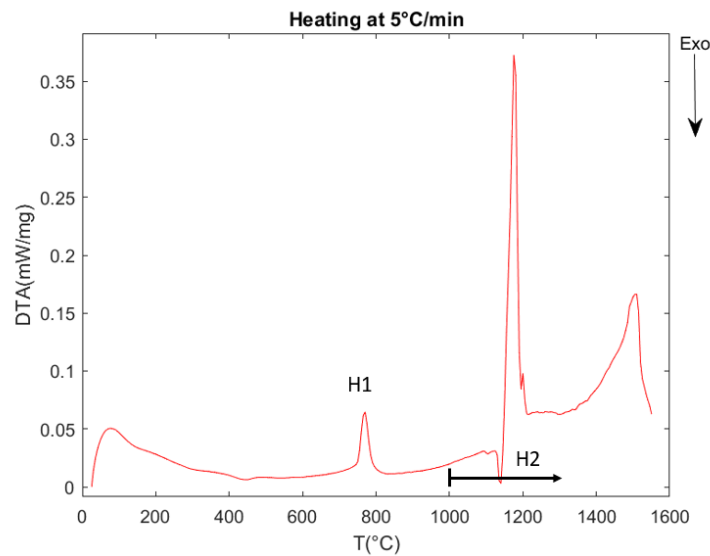
Figure 67: DTA heating curve for S2+20% (in volume) of SiC powder

Table 35: Principal heating peaks for S2+20% (in volume) of SiC powder

Peak	Start Temperature [°C]	End Temperature [°C]	Reaction or phase transformation
H1	750	820	Bainite/Martensite to Austenite of S2 powders
H2	1020	1520	Sintering of powders + Reverse peritectic transformation
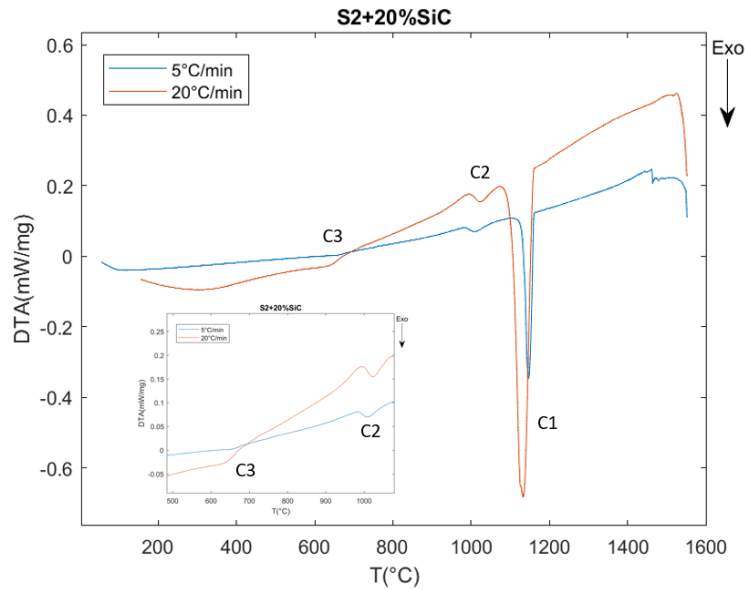
Figure 68: DTA cooling curve for S2+20% (in volume) of SiC powder at 5°C/min and 20°C/min of cooling rate

Table 36: Principal cooling peaks for S2+20% (in volume) of SiC powder at 5°C/min and 20°C/min of cooling rate

Peak	Start Temperature [°C]	End Temperature [°C]	Reaction or phase transformation
C1	1180	1100	Liquid to Austenite + eutectic Graphite
C2	1060	990	Eutectic Fe/Mo carbides
C3	680	630	Magnetic transition of α-Ferrite

Optical Microscope observations on the solidified powders are shown in Figure 69a and b. The presence of two distinct types of graphite were observed in the microstructures in addition to the usual Fe/Mo carbides and ferritic matrix (Figure 69c and d). The graphite flakes (type C) were the first phase that form, in fact, they are not contained in a grain or in grain boundaries, they pass through multiple ones. That is also confirmed by the fact that the rosettes formed and are arranged in function of the position of the flakes. Looking at SEM at higher magnification in Figure 69e and f, it was found that inside the graphite rosettes, there is no carbides precipitates differently from what was observed near the Fe/Mo eutectic carbides. Passing from 5°C/min of cooling rate to 20°C/min the microstructure obtained did not change, and the same phases were observed.
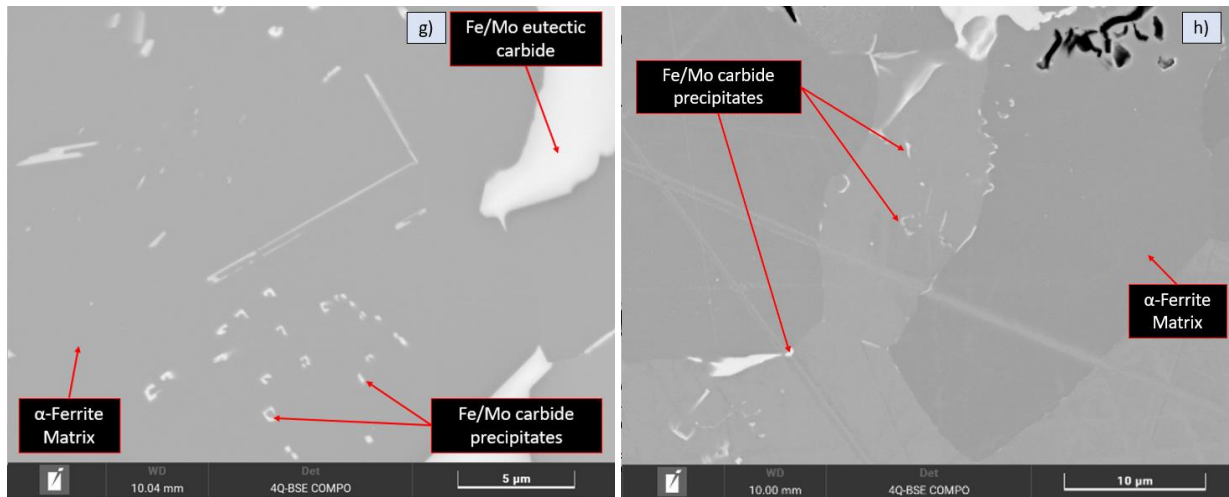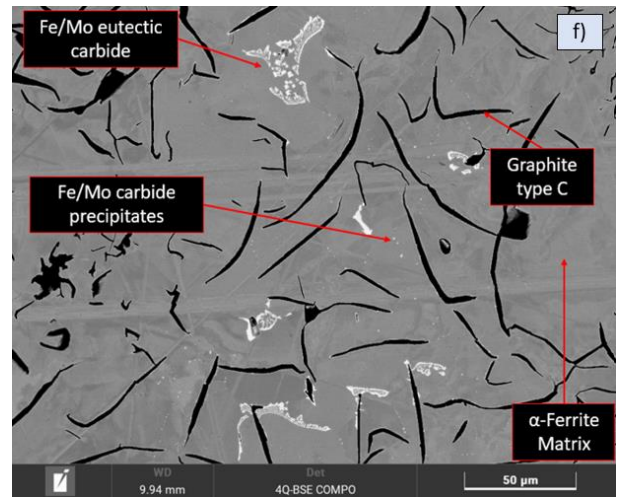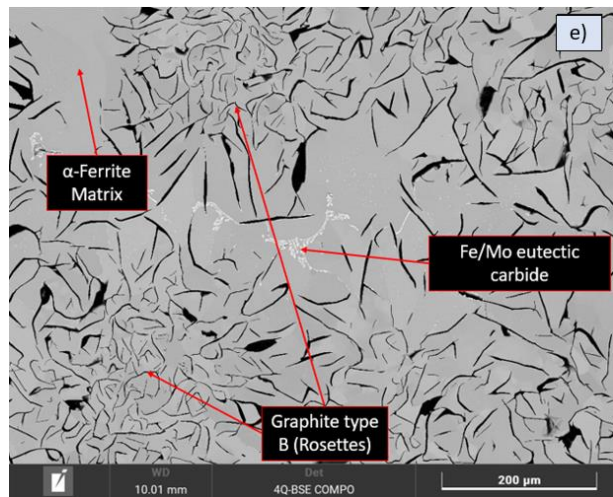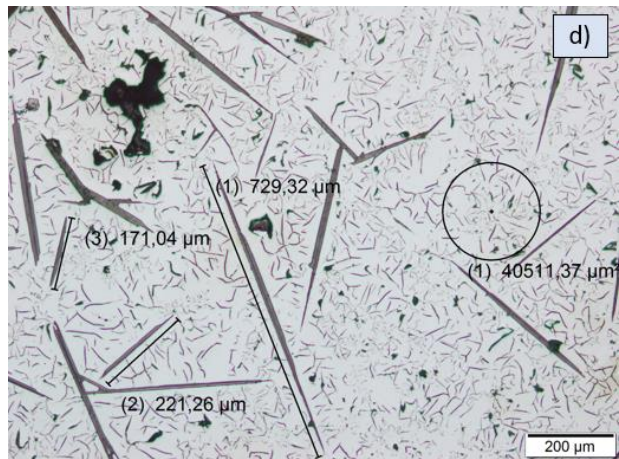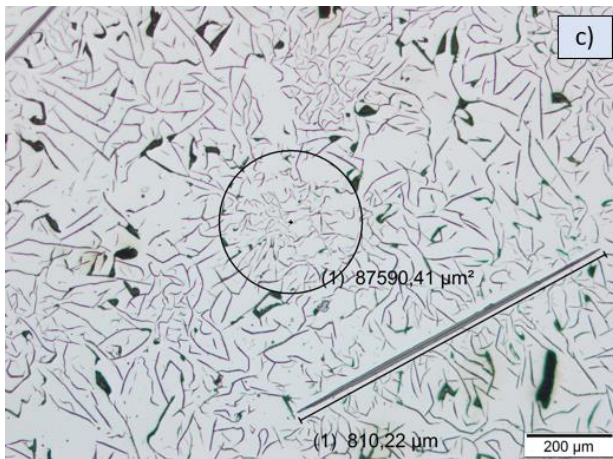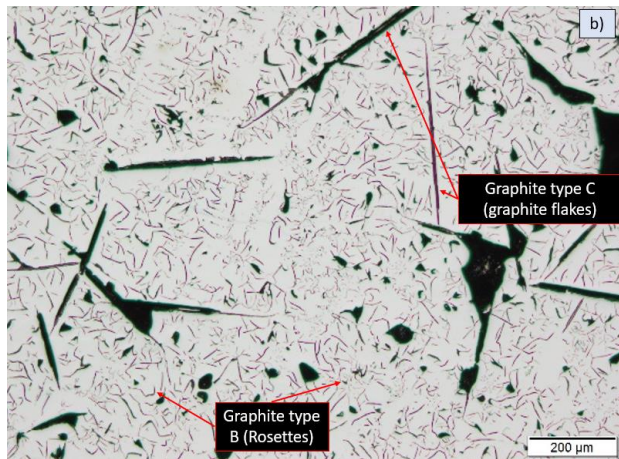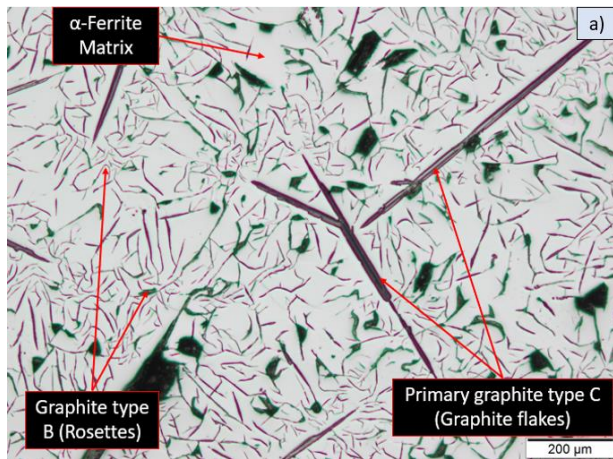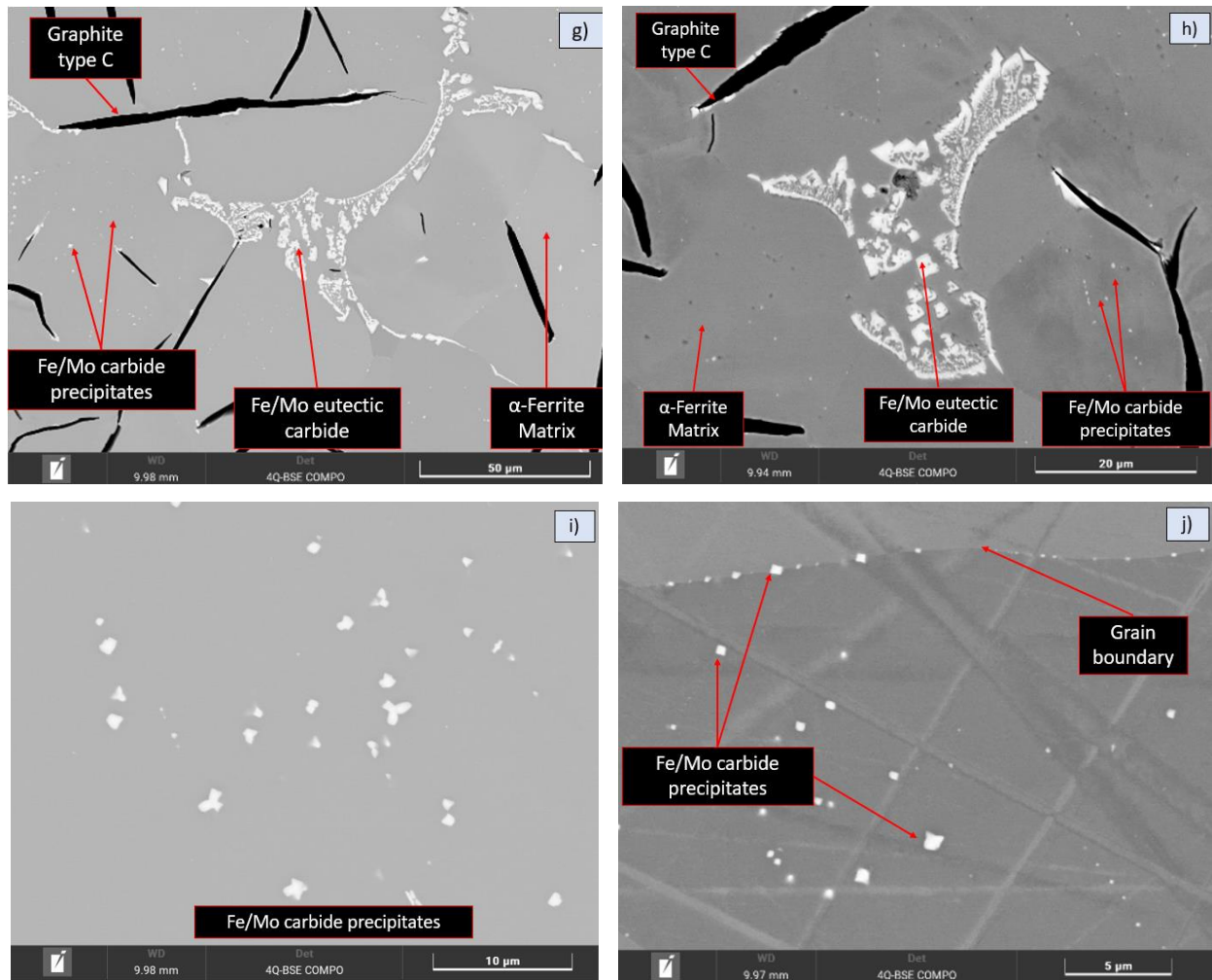
Figure 69: Microscope observations of S2+20% (in volume) of SiC. a-c-e-g-i) After DTA at 5°C/min of cooling rate. b-d-f-h-j) after DTA at 20°C/min of cooling rate

The compositions of the phases are evaluated using EDS at SEM. The values are resumed in Table 37 and Table 38.

Table 37: Atomic [%] compositions of different phases in S2+20% (in volume) of SiC at 5°C/min of cooling rate

%Atom	Carbon	Silicon	Manganese	Iron	Molybdenum
Fe/Mo carbide precipitates	$39,66 \pm 2,60$	$9,11 \pm 0,04$	$0,73 \pm 0,21$	$35,24 \pm 6,78$	$15,28 \pm 3,94$
Fe/Mo eutectic carbides	$42,82 \pm 1,84$	$8,75 \pm 0,38$	$0,51 \pm 0,09$	$27,88 \pm 3,27$	$20,05 \pm 2,23$
Matrix	$21,74 \pm 1,32$	$10,59 \pm 0,56$	$0,38 \pm 0,09$	$67,17 \pm 1,18$	$0,14 \pm 0,09$

Table 38: Atomic [%] compositions of different phases in S2+20% (in volume) of SiC at 20°C/min of cooling rate

%Atom	Carbon	Silicon	Manganese	Iron	Molybdenum

Fe/Mo carbide precipitates	**33,92** ± 6,43	**10,29** ± 0,86	**0,66** ± 0,17	**48,06** ± 9,76	**7,08** ± 4,32
Fe/Mo eutectic carbides	**39,42** ± 5,59	**8,77** ± 0,68	**0,60** ± 0,09	**39,38** ± 9,99	**11,82** ± 5,15
Matrix	**21,87** ± 1,81	**9,94** ± 3,14	**1,35** ± 3,15	**66,66** ± 1,93	**0,16** ± 0,08

An EBSD was conducted on S2 + 20% (in volume) of SiC sample as shown in Figure 70. The pattern quality shows a good revelation of the crystal lattice of the phases (Figure 70b). The phase map illustrated in Figure 70c was carried out with zero solutions of 14,7%. The matrix is fully ferritic, and the misorientation angle and grain size distributions were obtained in Figure 70e and f.
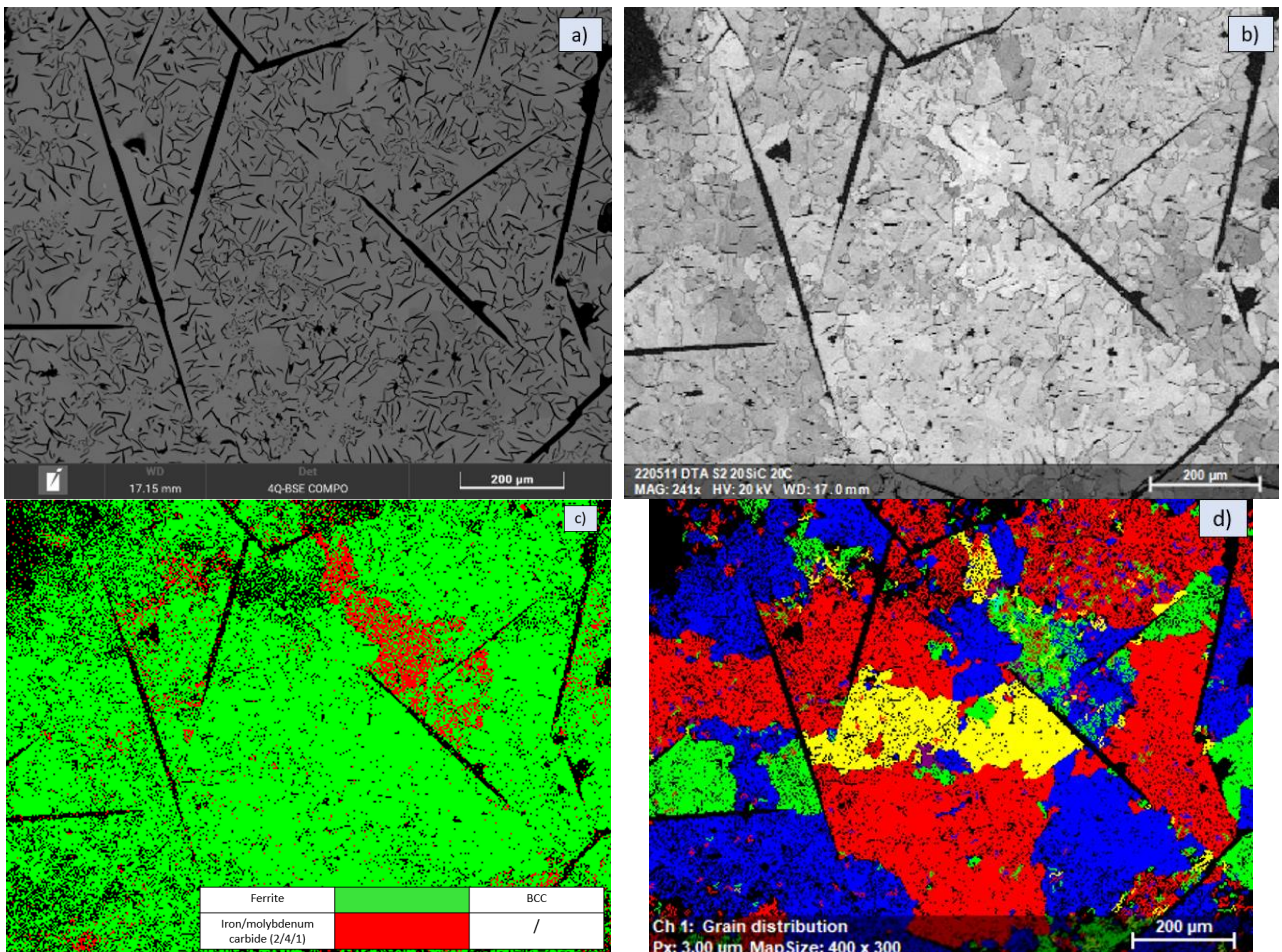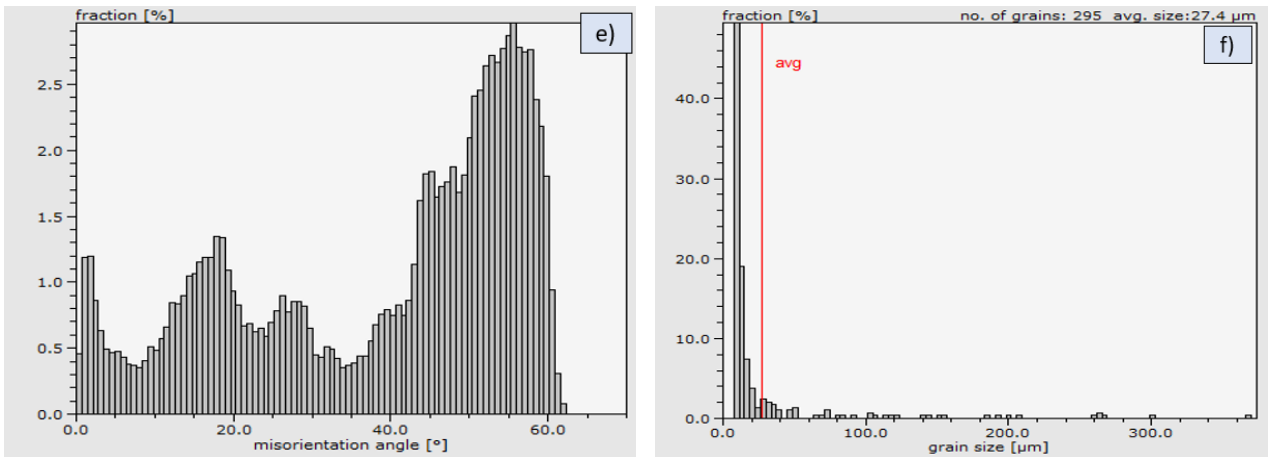
Figure 70: EBSD on S2+20% (in volume) of SiC powder at 20°C/min of cooling rate. a) EBSD area b) Pattern quality c) Phase map d) grains with misorientation above 15° e) Misorientation angle distribution f) Grains size distribution

A quantification of the phases was provided through Stream analysis software and the results are resumed in Table 39.
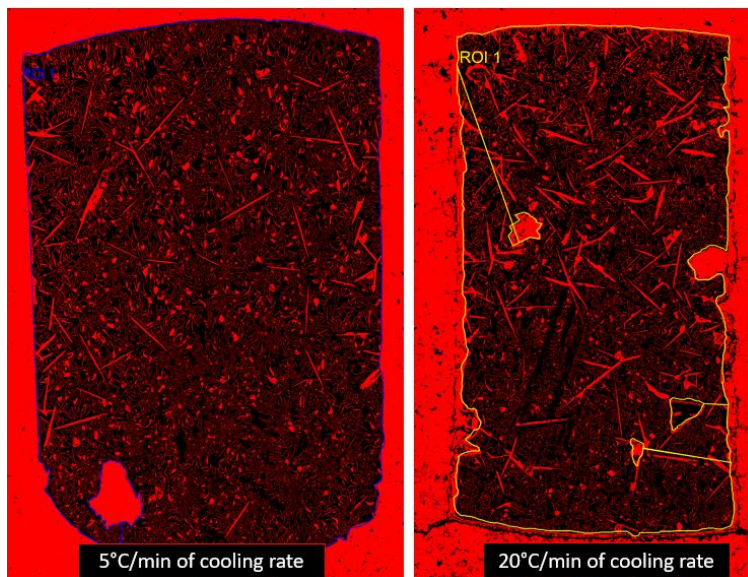
Figure 71: Quantification of the phases in the microstructure of S2+20% (in volume) of SiC powder

Table 39: Quantification of the phases of S2+20% (in volume) SiC powders of through Stream analysis software

S2 + 15% (in volume) of SiC	Quantification
5°C/min of cooling rate	22,75%
20°C/min of cooling rate	23,38%

- Specific DTA

A specific DTA was provided up to 1120°C to stop the heating cycle during the sintering of the powders. The aim was to observe the dissolution of the SiC powders and to understand in which way they influence the S2 powders. For this reason the S2 + 20% (in volume) of SiC powder was chosen for this test, and the maximum temperature has been chosen looking at the DTA curve of the complete thermal cycle of this mixture up to 1550°C (Figure 67). After this specific thermal cycle, a sample is prepared and observed at SEM (Figure 72). It was observed that the dissolution starts from the contact between S2 and SiC particles and continue in the inner zone of S2. At 1120°C the microstructure in the regions where the dissolution early start, graphite and ferritic matrix were formed. The other regions have the initial microstructure (bainitic/martensitic microstructure) that have been modified by the thermal cycle suffered by the powders. An EBSD was provided on the sample to confirm the phases obtained as shown in Figure 73. The pattern quality in Figure 73b shows that only the S2 powders gave accurate results. The phase map is shown in Figure 73c with zero solutions of 32,1%.
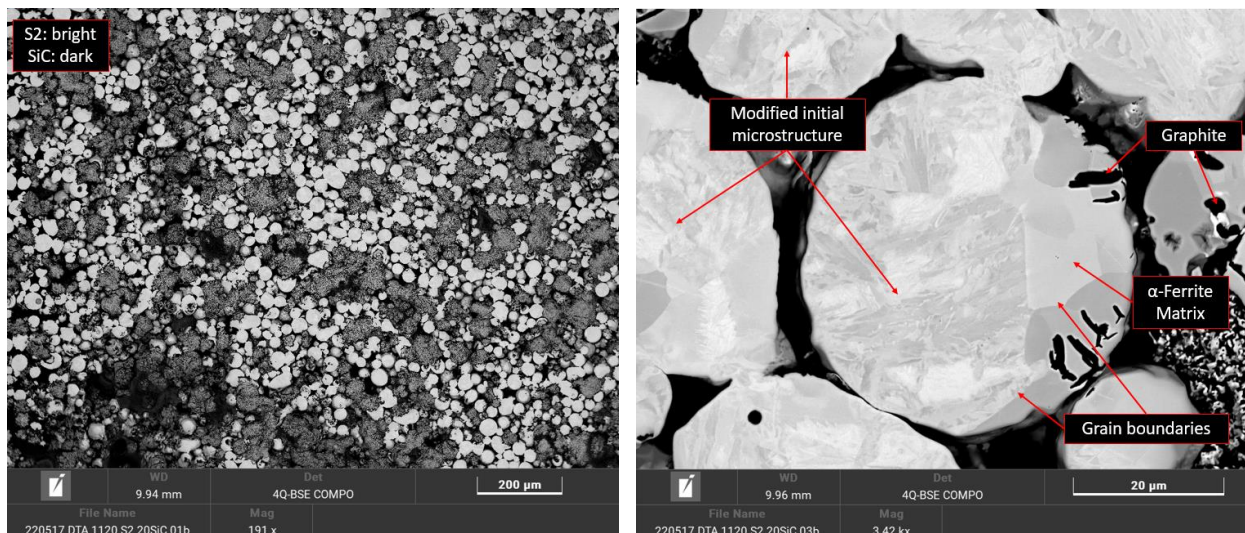
Figure 72: SEM micrographs
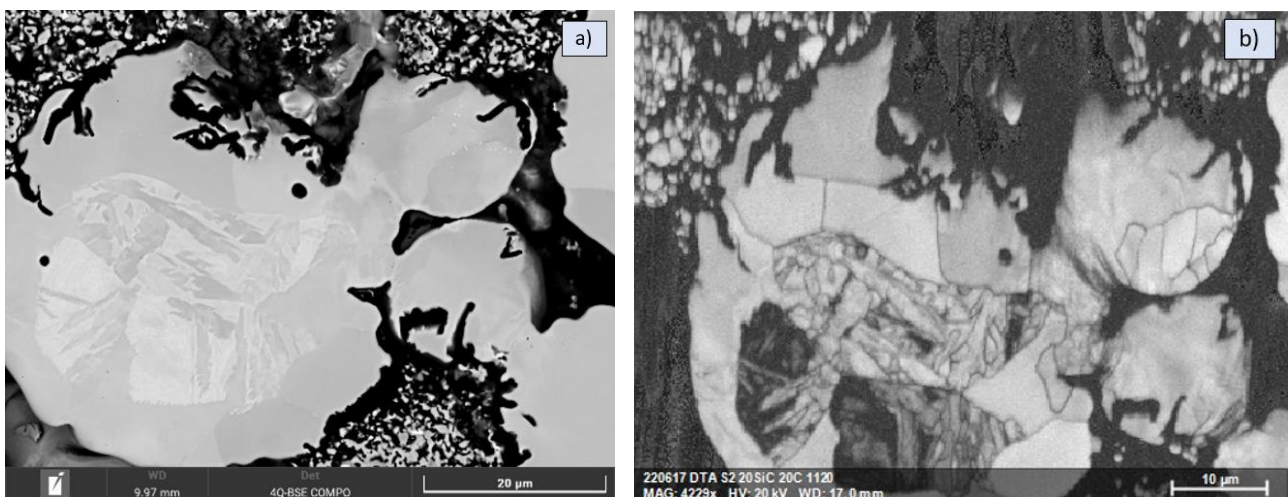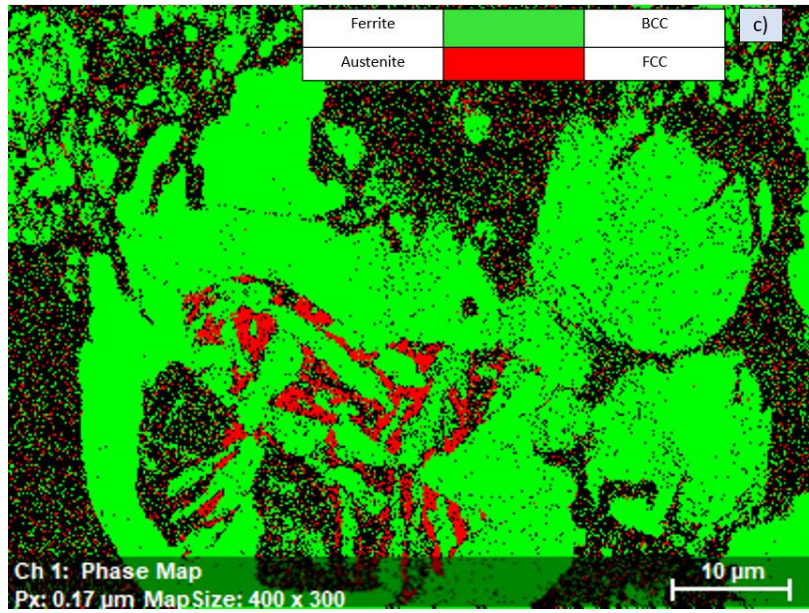
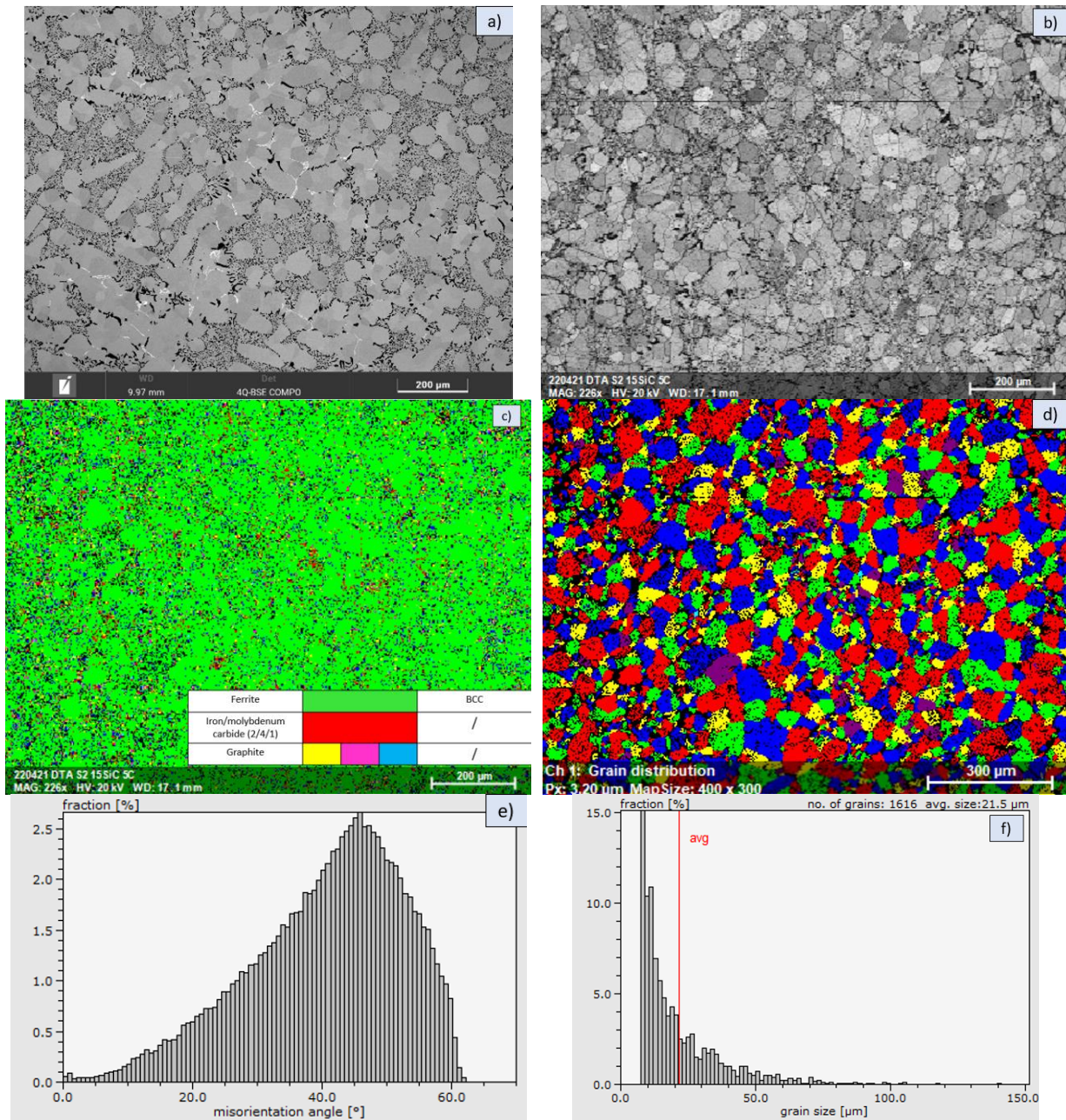*Figure 73: EBSD on S2+20% (in volume) of SiC powder at 20°C/min of cooling rate after specific DTA. a) EBSD area b) Pattern quality c) Phase map*

5. DISCUSSION
5.1 Rheological properties of powder mixtures

The preparation of powders for SLM application is crucial to avoid problems during the process and obtain a final component with good characteristics. When two powders with different properties are used, their preparation for the SLM process becomes more challenging, because of the difficulties to have a homogeneous batch of powder. The second aim of this study is to identify the proper method of preparation of the powder mix S2 + 15% (in volume) of SiC. This composition of the mixture was chosen because it represents a middle ground between the various compositions.

To determine the proper method of mix preparation the tap density properties and cohesiveness is analysed. Based on results of the tap density test that provides some indices, in addition to the cohesive index results, the manual mixing method of S2 + 15% (in volume) of pre-milled SiC powder results on the lowest value of cohesive index at every rotational speed represents the best mixing method to obtain the best performance in term of spreadability, although compared to S2 powder, all the mixing methods offer a better flowability. The same conclusion can be reached by comparing the Carr's index values with the support of Table 41 and Hausner ratio with the support of Table 40. The results of the test could be compared because the curve reach a plateau and ensure a good reliability. The mix prepared by ball milling of S2 with pre-milled offers the best performance in term of flowability but the difference with the other methods is not that relevant and have a good flowability. The value of the slope of the first 10 taps (α) shows a higher variation of S2 density compared to the three batches prepared. To rationalize the physical effects of mixed bimodal powders, where the main difference is particle size and shape, designated by effective sizes D_L and D_S [97]. The subscripts L stands for large and S for small. The packing density improves in the terminal region rich in small particles (low X) where large particles substitute dense regions for porous clusters of small particles (Figure 74).
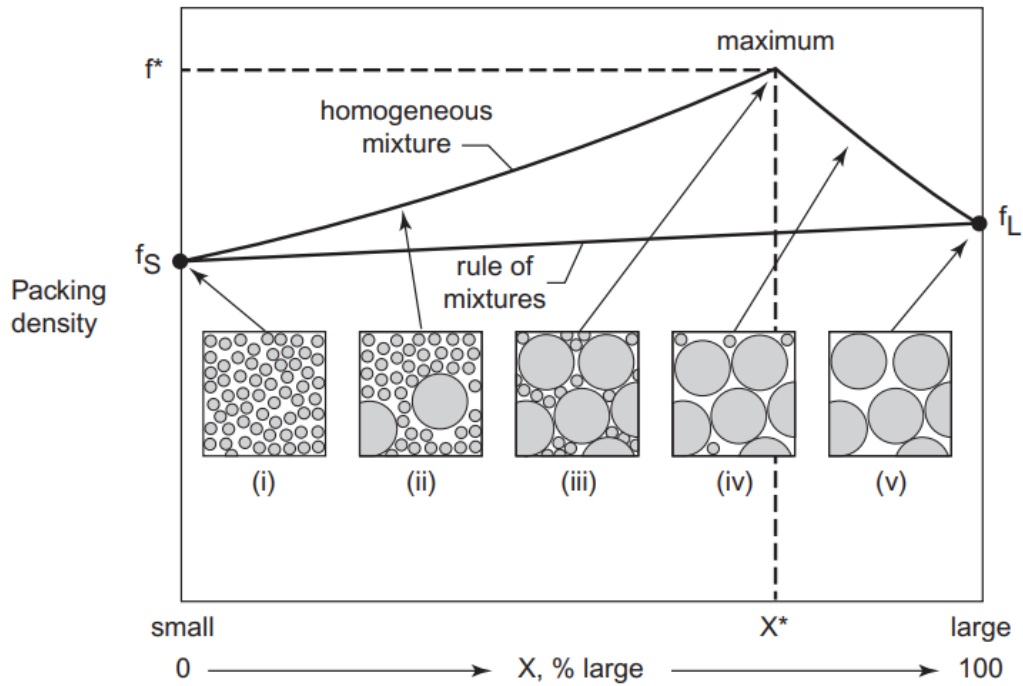
Figure 74: Packing density variation with composition from small to large particles

This is the case of S2 mixed with SiC powder that have a very low average particle size compared to S2. SiC particles fill the voids between the S2 particles and ensure a lower density variation. In many studies, it is found that the powder's flowability decreases with smaller particles because of an increase in powder cohesiveness. This cohesiveness, in previous study, represents the key to correlate powder characteristics to the spreadability [98].

Table 40: Powder flowability based on the Hausner ratio [99]

Flow character	Hausner ratio
Excellent	1.00 – 1.11
Good	1.12 – 1.18
Fair	1.19 – 1.25
Passable	1.26 – 1.34
Poor	1.35 – 1.45
Very poor	1.46 – 1.59
Very, very poor	> 1.60

Table 41: Estimation of powder flowability from the Carr's index value (calculated by $(\rho_n - \rho_0)/\rho_n$)

Carr index	Flowability
0.05 to 0.15	Very good
0.15 to 0.18	Good
0.18 to 0.22	Poor
0.22 to 0.35	Bad
0.35 to 0.40	Very bad
> 0.40	Awful

A recent study performed by Granutools allows a correlation between the spreadability of powder in powder bed fusion with the cohesive assessments of the powder [74]. When the powder cohesiveness increases, the cohesive index increases accordingly. The study cited above demonstrates that a powder that exhibits a higher cohesive index in the GranuDrum will produce less homogeneous layers in the printer. As mentioned in the beginning of the chapter, the investigation on the cohesiveness of the powders' mix is a critical point to understand the effectiveness of the mixing methods. The results of the GranuDrum test as shown in Figure 50, reveal a clear gap of the cohesive index, showing a higher value for the S2 powder compared to the S2 + 15% SiC batches. The behaviour of a powder depends on the inter-particle contact forces such as cohesive index and adhesive forces which are typically higher with more fine particles present in the mixture, but the driving gravitational forces act less on small particles due to their lower masses. A study demonstrates that an addition of 5-35 wt.% of fine particles reduce the cohesive index in a rapid flow regime because the magnitude of forces acting on the particles are different [100]. On the one hand, the inertial effect is stronger, which could lead to increased cohesive index. On the other hand, friction by cohesive and adhesive forces is typically reduced. This is to the rolling friction which is typically much smaller than static or sliding friction. Moreover, the trend of the cohesive index of S2 powder shows a strong shear thickening. This indicates that cohesiveness increases with rotational speed, which is associated with more intermittent and irregular flow. while S2 + pre-milled SiC mixed manually shows a shear thinning trend, both at high rotational speed of the drum. The shear thinning phenomenon at high rotational speed is due to the aeration of the powder at higher rotational speeds, which increases the distance between particles and thereby reduces the cohesive surface interactions [101]. The batches prepared through ball milling show a low dependence of the cohesive index from the rotational speed already above 10 rpm.

The good flowability of the manual mixed powders and his lowest value of cohesive index with a shear thinning phenomenon at high rotational speed are the characteristics that allow the deduction of this method as the best one compared to the others.

5.2 Sintering and dissolution of powders during heating

The first aim of this study is to deeper understand the role of SiC addition on the final microstructure of the mix S2 + SiC after a DTA analyse. DTA test cooling rates can be considered closed to the equilibrium conditions [81], therefore this study contribute as a base for the evaluation of the powder mix S2 + SiC for SLM applications, where the cooling rates are $10^5/10^6$ K/s and out-of-equilibrium microstructure are achieved [23] .

A first reference DTA test was performed only with S2 powders. The DTA heating curve in Figure 52a shows the expected transformations and reactions. The first endothermic peak is related to the transformation of the original martensitic structure of the S2 powders into austenite. Indeed, as revealed by the EBSD analysis on the cross section of the powders, BCC phases corresponding to martensite are indexed. This microstructure is formed due to the high cooling rates of the gas atomization process. At higher temperature, starting from 1050 °C, the sintering between powders occurs. Assuming the particles as spherical of the same size, the sintering can be represented as the sintering between two particles (Figure 75). The driving force behind sintering is largely determined by neck geometry and size. The distance between two spherical particles does not change but the neck size increases as the sintering time increases by material transport between the particles.
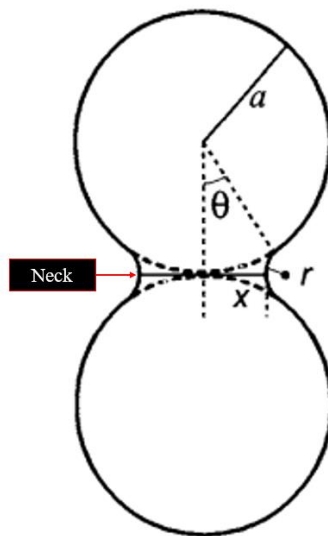
Figure 75: Two-particle model for initial stage sintering

When material comes to the neck from the particle surface, the distance between particles is not reduced but the neck size is increased. Therefore, the grain boundary is the source of material transport for densification and shrinkage in crystalline powder compacts. The diffusion mechanism, which is one of the most important sintering mechanisms, is related to the movement of atoms under a difference in vacancy concentration [82]. The sintering phenomenon continue until reach the reverse peritectic transformation at higher temperature. The reverse peritectic transition is achieved under

two consecutive steps: the reverse peritectic phase transformations (γ-austenite → γ-austenite and liquid → δ-ferrite) followed by the reverse peritectic reaction (γ-austenite → δ-ferrite + liquid) [83]. After reaching the liquid phase, the cooling step occurs until the solidification is completed at room temperature. The composition of S2 tool steel together with low cooling rates allows the formation of a Widmanstätten microstructure (Figure 53) following the solidification during the cooling stage using DTA. Such a microstructure is achieved under near-equilibrium conditions. This microstructure is formed also because of the initial composition of austenite that is not enough enriched by alloying elements to allow the formation of bainite or martensite, even if the cooling rate is increased.

The addition of SiC changes the melting sequence of the powders mix. Indeed, under both equilibrium and out-of-equilibrium conditions, SiC exhibits good dissolution properties under its melting temperature [[85][86]]. Microscope observations, after the specific DTA performed at 1120°C, revealed as shown in Figure 72 that in the regions of S2 in contact with SiC powder, this last starts dissolving causing an alteration of the local composition of the liquid and of the microstructure. The theories often utilized to model the dissolution process are based on Fick's laws of diffusion, the Noyes and Whitney equation, and Hixson and Crowell cube-root law [87]. Due to the presence of SiC powder in the S2 + SiC powder mixtures, the DTA heating curves (Figure 54a, Figure 56, Figure 61 and Figure 67) compared to the only S2 curve (Figure 52a) show many peaks around the reverse peritectic temperature. The local alteration of the composition due to the dissolution of SiC causes a variation of temperature at which the transformation occurs.

The liquid composition achieved at 1550 °C by varying the amount of SiC, also affect both the solidification sequence of the DTA cooling step and the final microstructure achieved when the solidification is completed. Combining the DTA cooling curve with microscope observations, EBSD and EDS analysis is possible to have comprehensive insights on the influence of the SiC on the powder mix S2 + SiC. The following discussion is done considering the DTA performed at 5°C/min of cooling rate only for simplicity, because the same speech can be done for 20°C/min of cooling rate samples. The biggest difference between the mixtures are the presence and the morphology of the graphite in addition to the type of matrix that is obtained. These differences are resumed in Figure 81.
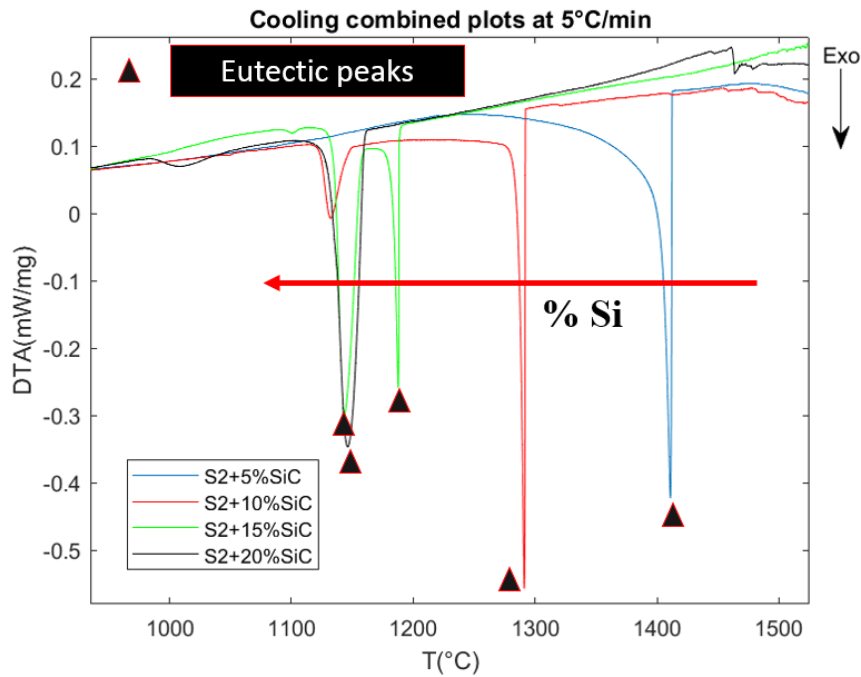
Figure 76: DTA cooling combined plots at 5°C/min of cooling rate in the range of temperature where solidification starts

5.3 Effects of cooling rate on solidification structures

In this study the variation of cooling rate is not large compared to the cooling rates achieved under AM processes, in fact, the two cooling rates performed were 5°C/min and 20°C/min. The microstructures of the mix with 15 and 20 vol.% of SiC, each obtained at the two different cooling rates, were compared to investigate on the effect of cooling rate on microstructure. The cooling rate sightly affects the morphology of the eutectic carbides and greatly affect their composition. Moreover, it affects the quantity of the phases, different from matrix phase, into the microstructure. The morphologies of two different eutectic carbides are shown in Figure 63e and f in the case of S2 + 15% SiC. A fish-bone structure can be clearly observed at 5°C/min of cooling rate. According to previous studies, this structure is frequently encountered with higher Mo-contents, related to higher degrees of segregations associated with slow cooling [95]. In the microstructure solidified at 20°C/min, the structure of the eutectic carbide does not assume a so defined structure because of a higher cooling rate.

A quantitative evaluation of the effects of cooling rate on microstructure is considered in the following discussion. The effect of the cooling rate on the composition of the Fe/Mo eutectic carbides can not be evidenced in the composition tables because it does not evidence the composition gradient in a Fe/Mo eutectic carbide. This gradient is due to the microsegregation of the alloying elements that increase when increasing the cooling rate [95]. To observe the effect of gradient of composition inside

the Fe/Mo eutectic carbides, the internal and boundary zones were evaluated distinctly as shown in Figure 77. The eutectic carbides of S2 + 20% (in volume) of SiC samples at 5 and 20°C/min of cooling rates were compared. Two shades of carbides were observed at SEM and correspond to two different compositions. Increasing the cooling rate, the composition gradient inside the eutectic carbides increases (Figure 77). This comparison is valid for all the microstructures that contain Fe/Mo eutectic carbides obtained at different cooling rates of the same mixture.

%Atom	Carbon	Silicon	Manganese	Iron	Molybdenum	
S2+20%SiC 5°C/min	43,24±1,35	8,67±0,31	0,52±0,10	26,52±1,52	21,05±0,82	(Bright zone)
	41,14±3,27	9,06±0,64	0,46±0,01	33,30±2,60	16,04±0,06	(Dark zone)

%Atom	Carbon	Silicon	Manganese	Iron	Molybdenum	
S2+20%SiC 20°C/min	43,99±2,00	8,21±0,40	0,60±0,13	30,72±2,20	16,49±0,86	(Bright zone)
	34,86±3,68	9,34±0,27	0,61±0,01	48,05±5,30	7,16±1,79	(Dark zone)
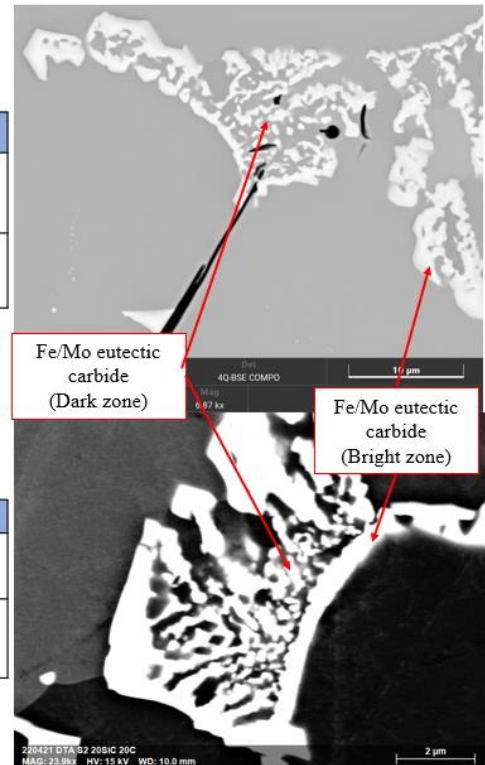
Figure 77: Iron/Molybdenum eutectic carbides in S2+20% (in volume) of SiC at 5°C/min and 20°C/min of cooling rates

Another effect of the cooling rate was observed during the quantification of the phases done on the overviews of the microstructure (Table 29, Table 34 and Table 39). It can be concluded, comparing the values, that increasing the cooling rate the amount of the phases different from matrix greatly increase. The cooling rate affects the maximum degree of undercooling at the beginning of graphite proeutectic and eutectic solidification [96]. Considering the S2 + 20% (in volume) of SiC, the number of graphite flake is higher at elevated cooling rate because higher is the undercooling, and higher is the number of nuclei that were generated. Moreover, the dimension of the graphite flakes and rosettes decrease increasing the cooling rate comparing the results in Figure 69e and f. This phenomenon consequently reduces the average grain size (Figure 64f and Figure 65).

5.4 Effects of the amount of silicon carbide on solidification and solid state transformations

5.2.1 Case of graphite, carbides and matrix phase during the solidification

Starting from liquid, the solidification occurs with exothermic transitions and transformations. As shown in Figure 75, the exothermic peaks are referred to the solidification sequence of the liquid with different amount of SiC. The formation of solid phase from liquid occurs releasing energy. So, on the DTA cooling curve an exothermic peak can be observed. The solid phases that form from the liquid depends on its composition. The addition of Si more than 2.5 wt.% causes the formation of graphite, impedes the formation of pearlitic structure, and promotes the ferritic structure. It promotes the formation of stable eutectic instead of by lowering the temperature for the metastable transformation under the stable one and increasing the gap between both. This phenomenon can be observed in all the samples at Si over 5 vol.% but is not visible on cooling curves during thermal analysis because the quantity of graphite is small and not occur with high variation of enthalpy, so endo or exothermic peaks cannot be easily evidenced. This phenomenon starts when the temperature falls under the graphite liquidus temperature and continue until the solidification path intersects the metastable extrapolation of the austenite liquidus, that favoured its nucleation from the bulk melt [88]. In the case of S2 + 5% (in volume) of SiC powder, the graphite is absent, because the amount of carbon Table 11 and graphitizing elements in the alloy (Figure 21) are not enough to establish the perfect conditions for the graphitizing phenomenon. Considering only the 5, 10 and 15 vol.% of SiC, the eutectic melting temperature, at which the transformation from liquid to γ-austenite, is lowered increasing the SiC amount, as shown in Figure 76. This phenomenon depends from the composition of the liquid. Increasing the amount of Si and C in the liquid, the eutectic temperature increases accordingly, and the austenite is stabilized at higher temperature.

When the liquid is highly heterogeneous caused by high local different composition, as in the case of S2 + 15% (in volume) of SiC, it can be observed that two distinct peaks were obtained for the transformation from liquid to austenite. As consequence, the solidification starts at two different ranges of temperature. To confirm this phenomenon, during the post-processing after the EBSD (Figure 64), the grains map and the misorientation (MO) angle distribution were investigated. Looking at the MO distribution, it can be observed many grains have a MO angle above 15° that suggested the independent nucleation of most of them. Looking at the EBSD area, two distinct regions can be identified: a region where there are mainly matrix and carbides in addition to non-eutectic graphite, and region where eutectic austenite and graphite grow. The first region seems nucleate in

the aftermath, also because the presence of most of the carbides in these areas is an index. It is known that the carbides nucleate and grow when the liquid is supersaturated of carbides forming elements during the solidification. These two solidifications that start in different moments can be observed in the DTA cooling curve.

The liquid phase becomes enriched in carbon and silicon rejected during the solidification from the austenite dendrites that initially start forming and growing. Then, when the eutectic concentration and temperature are reached, the stable eutectic transformation occur producing a cooperative growth of graphite and austenite [89]. This is correct for the eutectic graphite that form in these samples. The speech is different for S2 + 20% SiC because there are two different types of graphite. The graphite flakes (type C), that form in the case of the hypereutectic composition of the mixture (CE above 4.3%), start forming by the nucleation and the free growth of graphite particles from the melt. Comparing the amount of Silicon in all the phases present in the microstructure, except in graphite, is equally distributed. Looking at the composition tables in chapter 4.2, the amount of Silicon obviously increases in the matrix and carbides, increasing the amount of Si in the liquid. Using Stream Motion software on the overviews of the microstructures of the samples that contain graphite, it is observed that increasing the amount of Carbon and when the Silicon is enough to ensure the stable solidification path, the amount of graphite that is the main phase that is present in the microstructure, excluding the matrix, increases with of carbon amount. The amount of graphite does not increase overlimit, and in fact, comparing the amounts, the difference between 10 and 15 vol.% is way larger than the difference between 15 and 20 vol.%. In the same Figure 76, at lower temperature compared to eutectic peaks, an exothermic peaks are observed. The last liquid that remains during the solidification is rich in carbide formers.

Molybdenum is known to be an α-phase stabilizer but it is usually added because it also reduces the graphite content and strongly refine the graphite as well as the pearlite [92]. Also due to its strong carbide-former effect, the presence of Mo causes the formation of few Iron/Molybdenum carbides inside the microstructure. The Molybdenum amount is not enough to form a structured carbide Mo segregates strongly during solidification and as consequence, the formation of the eutectic carbides is obtained. In all the microstructures, the eutectic carbides are confined in the regions near the cell boundaries because of the segregation that raise the concentration of Mo in the last liquid that solidify. This allow to determine that the eutectic carbides were formed at elevated temperature during the solidification. The eutectic carbide formation can be seen in the DTA cooling curve in Figure 78 and coherently to what just said, the exothermic reaction occurs after the beginning of austenite solidification. When the concentration reaches the critical one, the carbides formation occurs [93].

These carbides reveal to be Iron/Molybdenum eutectic and precipitate carbides and were observed in the samples from 10% to 20% vol.%. To determine the type of carbides, the EDS analysis was provided as shown in chapter 4 and the results show the presence of Fe, Mo, Si, and small amount of Mn as components of the carbides. The morphologies of the eutectic carbides in the samples are quite similar. The concentration of the eutectic carbides in the different samples can be considered equal. This observation cannot be applied for the precipitates that vary in composition and in morphology.

5.2.2 Case of subsequent solid state transformations in the matrix phase

During the cooling in DTA, in a range of temperature between 600°C and 900°C, solid state transformations occurs. The microstructures of the samples observed through microscopes are generally the phases formed through solid state transformation. In the S2 + 5% (in volume) of SiC powder, the solidification follows the metastable one, causing the formation of a pearlitic matrix due to the composition and also because of the low cooling rate. The usual mechanism of formation of pearlite is by the decomposition of austenite, which form around 1400°C (Figure 76), upon cooling by diffusion of carbon atoms, when ferrite and cementite grow continuously, carbon precipitating as Fe_3C between laths of ferrite at the advancing interface leaving parallel laths of Fe-α and Fe_3C which is pearlite. As demonstrated in literature, the range of temperature for the pearlite formation is between 1150°C and 723°C. This range can be confirm in the DTA cooling curve in Figure 78. This phenomenon can be easily seen in the DTA cooling curve. The presence of a fully pearlitic matrix in non-theoretical eutectoid concentration and temperature is due to the alloying elements that modify the Fe-C curves, because at this composition and this temperature, a proeutectoid cementite should be observed, which is not the case. The effect of silicon and molybdenum is evident observing the microstructures of the samples from 10% to 20% vol.% SiC and looking at the eutectoid transformation peaks during DTA in Figure 78. On contrary, the eutectoid transformation occurs at increasingly higher temperature (Figure 78) because of silicon and molybdenum that both ferrite stabilizers, increasing the range of the α-phase. The influence is manifested in an increase in the ferrite and in a significant variation in shape, size, and distribution of graphite also due to the presence of Mo [90]. In S2 + 10% (in volume) of SiC, compared to 5 vol.%, a ferritic matrix is formed, and the pearlite is absent. The composition of the initial mixture suggests that the melt is in hypoeutectic range. it is difficult to determine the amount of primary austenite, and in addition, the following solid-state transformation of austenite into ferrite hinder the analysis of the austenite on the metallographic structure. The carbides that are observed were the Iron/Molybdenum carbides in very low amount and the presence of Troostite is observed. The Troostite has been revealed and differentiated from pearlite by the degree of fitness of the structure that was different and by the Carbon content that is

higher in Troostite compared to pearlite. The solidification mechanism of Troostite is similar to pearlite and its generally lower when the temperature of the troostite formation decrease but usually occur at higher cooling rates, moreover, the lamellae spacing is lower than pearlite [91].

To understand the influence of Si in the matrix phase, referring to the DTA curves and to the ternary Fe-C-Si diagram in Figure 79 are useful. It can observed that all the samples with a wt.% of Silicon under above 7% start the solidification with the formation of austenite. In all those cases, the austenite undergoes in solid state transformation showing the eutectoid. For the sample with 20 vol.% of Si, this eutectoid is absent (Figure 78), and this absence suggests that first phase that form do not undergo in solid state transformation. In fact, for this sample, under equilibrium after the formation of proeutectic graphite (type C), the ferrite is directly formed from the melt. This is due to the very high amount of Silicon in the melt that is over 7 wt.% (around 7.5%).
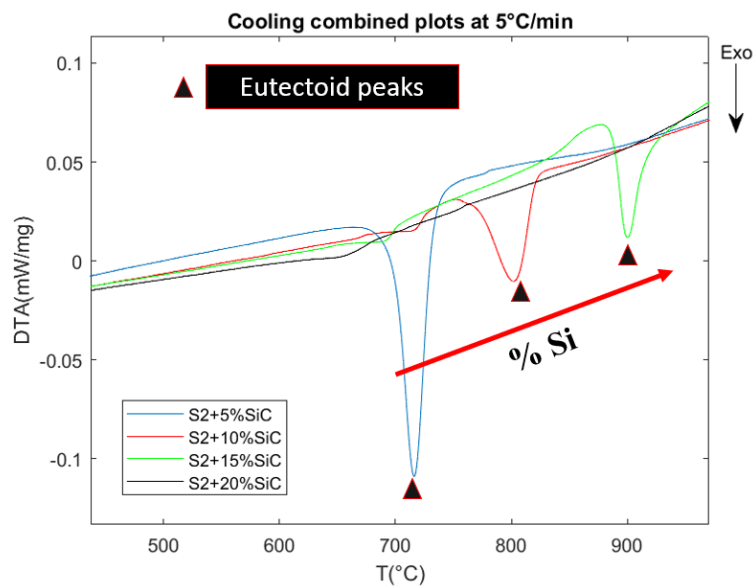
Figure 78: DTA cooling combined plots at 5°C/min of cooling rate in the range of temperature of eutectoid transformation
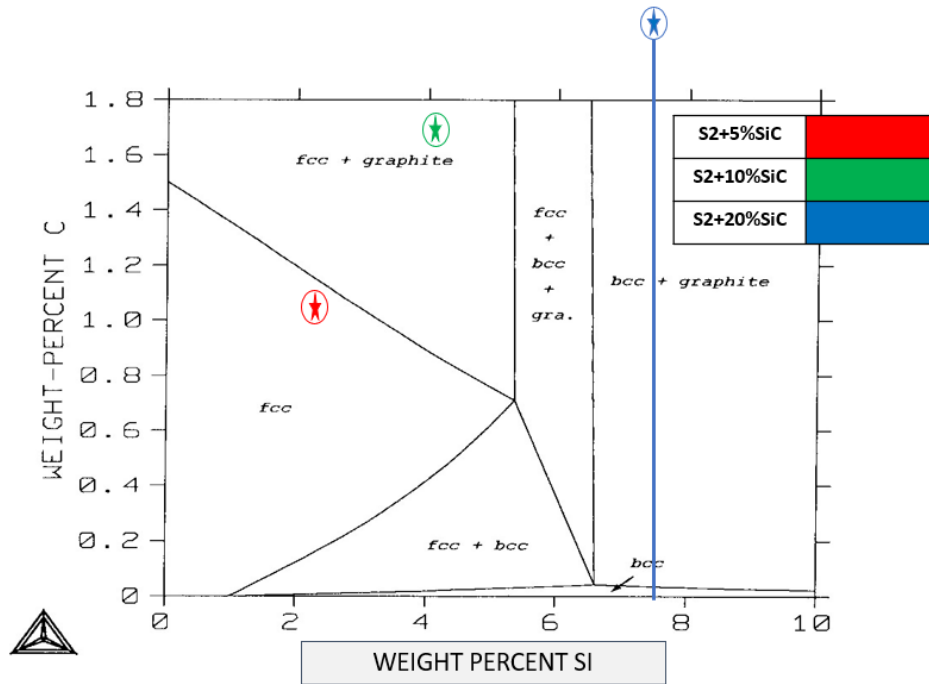
Figure 79: Calculated isothermal section (1000°C) of the iron-rich corner of the stable Fe-C-Si system

The matrix final phase is not the only generated in solid state transformations. Iron/Molybdenum carbide precipitates in solid state during the cooling at lower temperature. The precipitates do not necessarily form at the same temperature and are not highly exothermic. As consequence the peaks in the DTA cooling curve in Figure 78 do not show evident peaks relative to this precipitation. Observing at microscopes, it is observed that the intracellular precipitates have the same morphology in the 10 and 15 vol.% of SiC samples, and a butterfly morphology in 20 vol.%. This is due to the higher Mo content in the intracellular precipitates in this last sample. The intracellular precipitates were formed after the proeutectoid, and eutectoid transformation were completed and occur only at slower cooling rates in the ferritic matrix. This is demonstrated by the absence of grain boundaries between precipitates and ferrite grains [93]. These precipitates are not so exothermic because it is about a solid-state reaction and the corresponding peaks in a DTA cooling curves are not sharp and are difficult to determine.
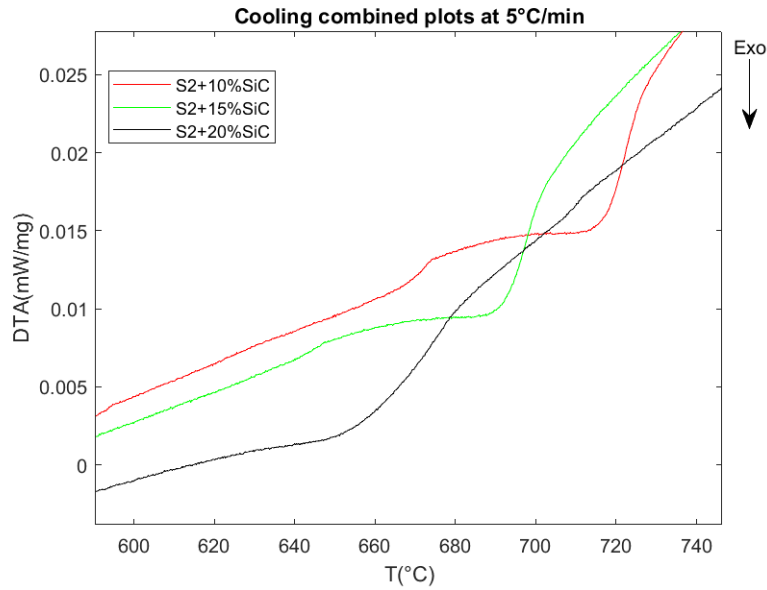
Figure 80: DTA cooling combined plots at 5°C/min of cooling rate in the range of temperature of magnetic Curie transition of ferrite

In the range of temperature between 620°C and 740°C, all microstructures with ferritic matrix present a peak (Figure 80) associated to the magnetic Curie transition of the ferrite according to similar results obtained in a previous study [94]. According to this study, this transition occurs at a temperature that decreases at the increase of the Silicon amount.

Figure 79 shows a resume of the phases obtained after the DTA of the different powders mix.
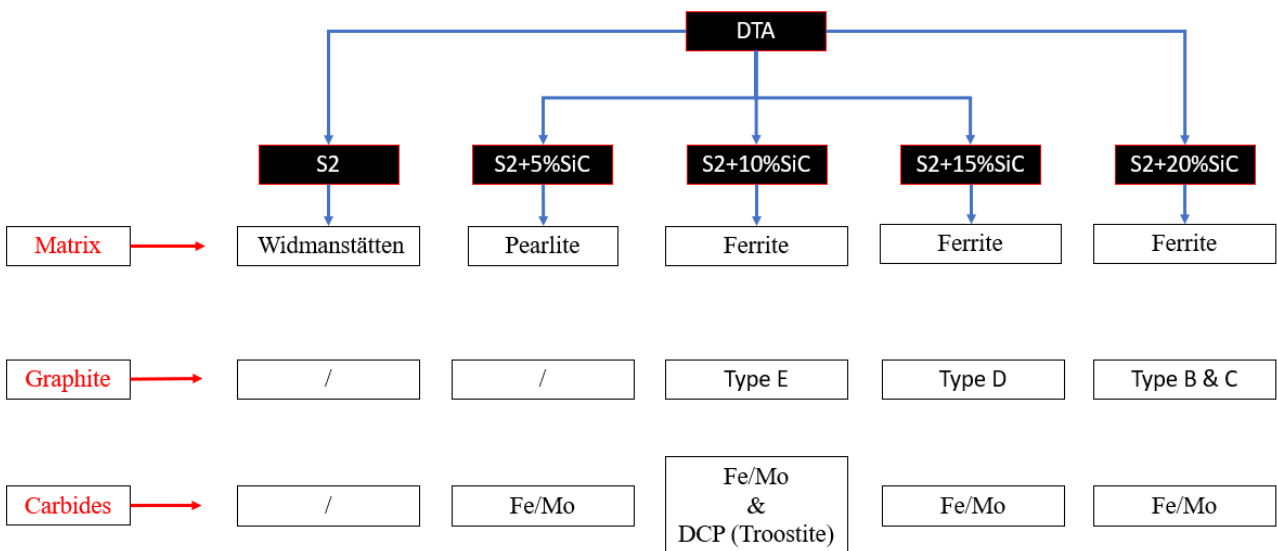
Figure 81: Phases of the microstructures of DTA mixtures

6. CONCLUSIONS

- The complete dissolution of SiC on S2 powder mixtures occur after heating up to 1550°C. Varying the amount of SiC, the microstructure of the solid obtained is altered. Increasing the amount of SiC, the formation of graphite of several types is promoted according to the Si amount. An addition of 5% in volume of SiC is not enough to cause the formation of graphite, and as result, with 5 vol.% of SiC, a fully pearlitic microstructure solidified without graphite. While from 10% to 20%, several graphite types are obtained.

- Analysing the DTA curve and according to literature, an amount of Si higher than 7 wt.% allow the formation of ferrite instead of austenite as first phase that form from the liquid. This phenomenon has been observed of S2 + 20% (in volume) of SiC powder. Compared to S2 tool steel subjected to DTA, in which the microstructure obtained is Widmanstätten after complete solidification, the addition of SiC change the solid to pearlitic and ferritic matrix according to the amount. The Mo and C contents in the mixtures, in addition to the cooling rate near equilibrium during the DTA allow the formation of Iron/Molybdenum eutectic carbide and precipitates.

- The cooling rate affects the amount of the phases different from matrix in the microstructure. In fact, it was observed that increasing the cooling rate, the amount of phases increase and the composition of the carbides becomes more heterogeneous. Another effect observed is the difference in dimension of the phases varying the cooling rate. Higher is the cooling rate and lower will be the dimension of the phases that form during solidification.

- Different batches of S2 + 15% (in volume) of SiC powder prepared with ball milling and manual mixing show a good rheological property of the powders compared to the only S2 powder. All the methods operated did not cause an alteration of the phases and oxidation. Between these methods, it is determined that a manual mixing of S2 powder with pre-milled SiC performed with ball milling result the best mixing method in term of flowability and tap density. For the preparation of the feedstock for SLM application, the methods adopted are valid to obtain good rheological properties of the mix.

7. PERSPECTIVES

- Higher amount of SiC (> 30 % in volume) can be added to S2 and study the mixture through DTA in order to have deeper insights on high Si and C steels.

- Try different powders preparation in order to achieve the best powder batch for the SLM application.

- A rheological properties investigation should be performed reducing the vol.% of SiC under 15% of the powder mixture to observe the influence of the SiC amount. It will be interesting to provide the analyses on S2 + 10 vol.% of SiC powder.

- The mechanical properties of the pieces will be studied to understand the possible application of this alloy

8. REFERENCES

[1] M. Mehrpouya, A. Dehghanghadikolaei, B. Fotovvati, A. Vosooghnia, S. S. Emamian, and A. Gisario, "The Potential of Additive Manufacturing in the Smart Factory Industrial 4.0: A Review," *Applied Sciences 2019, Vol. 9, Page 3865*, vol. 9, no. 18, p. 3865, Sep. 2019, doi: 10.3390/APP9183865.

[2] G. Yang, Y. Xie, S. Zhao, Y. Ren, and C. Wang, "Methods and Mechanism of Powder Mixing for Selective Laser Melting," vol. 22, no. 1, pp. 102–110, 2022.

[3] "European Powder Metallurgy Association (EPMA) - What is Powder Metallurgy?" https://www.epma.com/what-is-powder-metallurgy .

[4] K. Skotnicová, M. Kursa, and I. Szurman, "VŠB-TECHNICAL UNIVERSITY OF OSTRAVA Faculty of Metallurgy and Materials Engineering POWDER METALLURGY," 2014.

[5] H. Danninger, R. de Oro Calderon, and C. Gierl-Mayer, "Powder Metallurgy and Sintered Materials," in *Ullmann's Encyclopedia of Industrial Chemistry*, Wiley-VCH Verlag GmbH & Co. KGaA, 2017, pp. 1–57. doi: 10.1002/14356007.a22_105.pub2.

[6] "Metal powders for AM: Manufacturing processes and properties." https://www.metal-am.com/articles/metal-powders-for-3d-printing-manufacturing-processes-and-properties/

[7] G. S. Upadhyaya, "POWDER METALLURGY TECHNOLOGY."

[8] "Introducing Powder Metallurgy." https://www.mpif.org/IntrotoPM.aspx.

[9] A. S. Mujumdar, *Handbook of industrial drying*. CRC press, 2006.

[10] O. D. Neikov, "Atomization and Granulation," in *Handbook of Non-Ferrous Metal Powders*, Elsevier, 2019, pp. 125–185. doi: 10.1016/b978-0-08-100543-9.00004-x.

[11] "Optimizing Metal Powders for Additive Manufacturing | Additive Manufacturing." https://www.additivemanufacturing.media/articles/.

[12] "The Water-Atomizing Process: Part One :: Total Materia Article." https://www.totalmateria.com/.

[13] C. Suryanarayana, "Mechanical Alloying: A Novel Technique to Synthesize Advanced Materials," *Research*, vol. 2019, pp. 1–17, May 2019, doi: 10.34133/2019/4219812.

[14] A. Al-Azzawi, P. Baumli, and G. Mucsi, "Mechanical Alloying and Milling," 2015. doi: 10.26649/musci.2015.017.

[15] "ISO/ASTM 52900:2015(en), Additive manufacturing — General principles — Terminology." https://www.iso.org/obp/ui#iso:std:iso-astm:52900:ed-1:v1:en:term:2.6.1.

[16] "Applications for Additive Manufacturing technology." https://www.metal-am.com/introduction-to-metal-additive-manufacturing-and-3d-printing/applications-for-additive-manufacturing-technology/

[17] S. Ford and M. Despeisse, "Additive manufacturing and sustainability: an exploratory study of the advantages and challenges," *Journal of Cleaner Production*, vol. 137, pp. 1573–1587, Nov. 2016, doi: 10.1016/J.JCLEPRO.2016.04.150.

[18] M. Gebler, A. J. M. Schoot Uiterkamp, and C. Visser, "A global sustainability perspective on 3D printing technologies," *Energy Policy*, vol. 74, no. C, pp. 158–167, Nov. 2014, doi: 10.1016/J.ENPOL.2014.08.033.

[19]   S. H. Huang, P. Liu, A. Mokasdar, and L. Hou, "Additive manufacturing and its societal impact: a literature review," *The International Journal of Advanced Manufacturing Technology 2012 67:5*, vol. 67, no. 5, pp. 1191–1203, Oct. 2012, doi: 10.1007/S00170-012-4558-5.

[20]   R. Jiang, R. Kleer, and F. T. Piller, "Predicting the future of additive manufacturing: A Delphi study on economic and societal implications of 3D printing for 2030," *Technological Forecasting and Social Change*, vol. 117, pp. 84–97, Apr. 2017, doi: 10.1016/J.TECHFORE.2017.01.006.

[21]   I. Ribeiro *et al.*, "Framework for life cycle sustainability assessment of additive manufacturing," *Sustainability (Switzerland)*, vol. 12, no. 3, Feb. 2020, doi: 10.3390/su12030929.

[22]   "METAL ADDITIVE MANUFACTURING PM TITANIUM CONFERENCE REPORT NON-FERROUS POWDER PRODUCTION POWDER METALLURGY REVIEW," 2014.

[23]   B. Song, S. Wen, C. Yan, Q. Wei, and Y. Shi, "Introduction and basic principles," in *Selective Laser Melting for Metal and Metal Matrix Composites*, Elsevier, 2021, pp. 1–16. doi: 10.1016/b978-0-08-103005-9.00001-8.

[24]   W. ming Peng *et al.*, "Bionic mechanical design and 3D printing of novel porous Ti6Al4V implants for biomedical applications," *Journal of Zhejiang University: Science B*, vol. 20, no. 8, pp. 647–659, Aug. 2019, doi: 10.1631/jzus.B1800622.

[25]   B. Song, S. Wen, C. Yan, Q. Wei, and Y. Shi, "Guidelines for selective laser melting," in *Selective Laser Melting for Metal and Metal Matrix Composites*, Elsevier, 2021, pp. 17–33. doi: 10.1016/b978-0-08-103005-9.00002-x.

[26]   H. P. Tang, M. Qian, N. Liu, X. Z. Zhang, G. Y. Yang, and J. Wang, "Effect of Powder Reuse Times on Additive Manufacturing of Ti-6Al-4V by Selective Electron Beam Melting," *JOM*, vol. 67, no. 3, pp. 555–563, Mar. 2015, doi: 10.1007/s11837-015-1300-4.

[27]   V. Seyda, N. Kaufmann, and C. Emmelmann, "Investigation of Aging Processes of Ti-6Al-4 V Powder Material in Laser Melting," *Physics Procedia*, vol. 39, pp. 425–431, Jan. 2012, doi: 10.1016/J.PHPRO.2012.10.057.

[28]   L. Cordova, M. Mo´, M. Campos, and T. Tinga, "EFFECTIVE PRODUCTION AND RECYCLING OF POWDER MATERIALS Revealing the Effects of Powder Reuse for Selective Laser Melting by Powder Characterization," *JOM*, vol. 71, doi: 10.1007/s11837-018-3305-2.

[29]   H. P. Tang, M. Qian, N. Liu, X. Z. Zhang, G. Y. Yang, and J. Wang, "Effect of Powder Reuse Times on Additive Manufacturing of Ti-6Al-4V by Selective Electron Beam Melting," *JOM*, vol. 67, no. 3, pp. 555–563, Mar. 2015, doi: 10.1007/s11837-015-1300-4.

[30]   J. Clayton, D. Millington-Smith, and B. Armstrong, "The Application of Powder Rheology in Additive Manufacturing," *JOM*, vol. 67, no. 3, pp. 544–548, Mar. 2015, doi: 10.1007/s11837-015-1293-z.

[31]   O. D. Neikov and N. A. Yefimov, "Powder Characterization and Testing," in *Handbook of Non-Ferrous Metal Powders*, Elsevier, 2019, pp. 3–62. doi: 10.1016/b978-0-08-100543-9.00001-4.

[32]   A. P. Ferreira, C. F. Rawlinson-Malone, J. Gamble, S. Nicholson, and M. Tobyn, "Applications of Multivariate Analysis to Monitor and Predict Pharmaceutical Materials Properties," *Multivariate Analysis in the Pharmaceutical Industry*, pp. 235–267, 2018, doi: 10.1016/B978-0-12-811065-2.00008-4.

[33]   *Metallography, Structures, and Phase Diagrams*, 8th ed., vol. Vol 8. American Society for Metals, 1973.

[34]   J. Antonio, P.-S. Elorz, D. Fernández González, and L. Felipe Verdeja, "Physical Metallurgy of Cast Irons."

[35] B. Zheng *et al.*, "Three-Body Abrasive Behavior of Cementite-Iron Composite with Different Cementite Volume Fractions," *Tribology Letters*, vol. 62, no. 2, May 2016, doi: 10.1007/s11249-016-0683-x.

[36] v. Raghavan, *Alloys Phase Diagrams*, vol. 2. 1986.

[37] J. Lacaze and B. O. Sundman, "An Assessment of the Fe-C-Si System.", vol.22. 1991

[38] W. Patterson, G. HULSENBECK, and H. A. S. Madi, "A STUDY OF THE SOLIDIFICATION EQUILIBRIA IN THE IRON CORNER OF THE STABLE IRON-CARBON-SILICON SYSTEM," *GIESSEREI FORSCH*, vol. 20, no. 2, pp. 49–65, 1968.

[39] V. A. Il'inskii, L. v Kostyleva, and M. N. Litvinenko, "Group of nonliquating alloys with constant solidification point in the system Fe−C−Si," *Metal Science and Heat Treatment*, vol. 34, no. 2, pp. 86–93, 1992, doi: 10.1007/BF00769872.

[40] J. Chipman, J. C. Fulton, N. Gokcen, and G. R. Caskey, "Activity of silicon in liquid Fe-Si and Fe-C-Si alloys," *Acta Metallurgica*, vol. 2, no. 3, pp. 439–450, May 1954, doi: 10.1016/0001-6160(54)90064-4.

[41] J. E. Hilliard and W. S. Owen, "A THERMAL AND MICROSCOPIC STUDY OF THE IRON CARBON SILICON SYSTEM," *Journal of the Iron and Steel Institute*, vol. 172, no. 3, p. 268, 1952.

[42] Y. N. Malinochka and V. Z. Dolinskaya, "A New Metastable Equilibrium Diagram and Structure of Iron-Carbon-Silicon Alloys," *Liteinoe Proizvod*, vol. 7, pp. 26–27, 1970.

[43] W. Oldfield, "The chill-reducing mechanism of silicon in cast iron," *BCIRA Journal*, vol. 10, no. 1, pp. 17–27, 1962.

[44] J. Lacaze and B. O. Sundman, "An Assessment of the Fe-C-Si System.", vol. 22A, 1991

[45] "Cast iron - tec-science." https://www.tec-science.com/material-science/iron-carbon-phase-diagram/cast-iron/ (accessed Jun. 14, 2022).

[46] G. F. vander Voort, "ANALYTICAL CHARACTERIZATION OF ALUMINUM, STEEL, AND SUPERALLOYS," 2006.

[47] K. B. Rundman, "Chapter 09803 - Cast Irons," 2016, doi: 10.1016/B978-0-12-803581-8.09803-9.

[48] M. Tisza, *Physical Metallurgy for Engineers*. ASM International, 2001.

[49] J. E. Bringas and M. L. (Michael L. Wayman, *CASTI metals black book, European ferrous data*. CASTI Pub, 2003.

[50] "INTERNATIONAL ® The Materials Information Company."

[51] "Alloying_Elements_in_Steel_2nd_Ed_by_E_c".

[52] X. R. Chen, Q. J. Zhai, H. Dong, B. H. Dai, and H. Mohrbacher, "Molybdenum alloying in cast iron and steel," *Advances in Manufacturing*, vol. 8, no. 1, pp. 3–14, Mar. 2020, doi: 10.1007/s40436-019-00282-1.

[53] "The Effects of Alloying Elements on Iron-Carbon Alloys :: Total Materia Article." https://www.totalmateria.com/page.aspx?ID=CheckArticle&site=kts&LN=PT&NM=151 (accessed Jun. 14, 2022).

[54] J. Lacaze *et al.*, "Redistribution and Effect of Various Elements on the Morphology of Primary Graphite in Cast Iron," 2013, doi: 10.1155/2013/638451.

[55] C. K. Gupta, *Extractive Metallurgy of Molybdenum*. Routledge, 2017. doi: 10.1201/9780203756287.

[56] "Molybdenum in cast iron." https://www.giessereilexikon.com/en/foundry-lexicon/Encyclopedia/show/molybdenum-in-cast-iron-4929.

[57] J. R. Davis, "Cast Irons, ASM International," *Materials Park, OH*, pp. 5–8, 1996.

[58] D. M. Stefanescu, "Solidification and modeling of cast iron—A short history of the defining moments," *Materials Science and Engineering: A*, vol. 413, pp. 322–333, 2005.

[59] Č. ISO, "Microstructure of cast irons-Part 1: Graphite classification by visual analysis," 2008.

[60] G. Toktaş, M. Tayanç, and A. Toktaş, "Effect of matrix structure on the impact properties of an alloyed ductile iron," *Materials Characterization*, vol. 57, no. 4–5, pp. 290–299, Dec. 2006, doi: 10.1016/J.MATCHAR.2006.02.008.

[61] Io. Standardization, "Microstructure of cast irons–Part 1: Graphite classification by visual analysis." ISO, 2008.

[62] E. Fraś and M. Górny, "Inoculation effects of cast iron," *Archives of Foundry Engineering*, 2012.

[63] Meehan A.F, " Making Gray Iron," U.S.A, Jun. 1924.

[64] P. Magnin and W. Kurz, "Competitive growth of stable and metastable Fe- C- X eutectics: Part I. experiments," *Metallurgical Transactions A*, vol. 19, no. 8, pp. 1955–1963, 1988, doi: 10.1007/BF02645199.

[65] "Osprey — Osprey® metal powders and CE alloys." https://www.osprey.sandvik/en/

[66] "High-performance ceramics sector | KYOCERA Fineceramics Precision GmbH." https://www.kyocera-precision.com/company/ (accessed Jun. 15, 2022).

[67] "Planetary Mono Mill PULVERISETTE 6 classic line / Description - fritsch.de." https://www.fritsch-international.com/sample-preparation/milling/planetary-mills/details/product/pulverisette-6-classic-line.

[68] "NETZSCH - Analysing and testing. Leading Thermal analysis, rheology and firetesting - NETZSCH Analyzing & Testing." https://analyzing-testing.netzsch.com/en.

[69] "Metallographic products, knowledge and service | Struers.com." https://www.struers.com/.

[70] "Olympus Global Homepage." https://www.olympus-global.com/.

[71] "TESCAN CLARA | New Field-Free UHR SEM - TESCAN." https://www.tescan.com/tescan-clara-new-field-free-uhr-sem.

[72] "Granutools | GranuPack." https://www.granutools.com/en/granupack.

[73] G. Lumay *et al.*, "Measuring the flowing properties of powders and grains," *Powder Technology*, vol. 224, pp. 19–27, Jul. 2012, doi: 10.1016/J.POWTEC.2012.02.015.

[74] A. Neveu, F. Francqui, and G. Lumay, "How to Relate the Spreadability of Powder to the Layer Homogeneity in Powder Bed Fusion Additive Manufacturing: A Correlation between Cohesion Assessments and In Situ Printer Measurements," in *Progress in additive manufacturing 2020*, 100 Barr Harbor Drive, PO Box C700, West Conshohocken, PA 19428-2959: ASTM International, 2022, pp. 40–50. doi: 10.1520/STP163720200118.

[75] "Granutools | GranuDrum." https://www.granutools.com/en/granudrum

[76] "Granutools | GranuDrum." https://www.granutools.com/en/granudrum

[77] "D8 DISCOVER Plus | Bruker." https://www.bruker.com/en/products-and-solutions/diffractometers-and-scattering-systems/x-ray-diffractometers/d8-discover-family/d8-discover-plus.html

[78] B. Vertruyen, "Presentation of the X-ray diffractometer at GREENMAT (University of Liege): characterization of polycrystalline materials."

[79] G. R. Purdy, "Widmanstätten Structures," *Encyclopedia of Materials: Science and Technology*, pp. 9575–9578, Jan. 2001, doi: 10.1016/B0-08-043152-6/01732-0.

[80] K. Liu, Z. Jiang, and J. Li, "Study on troostite structures of grey cast iron processed by heat treatment," *Procedia Engineering*, vol. 15, pp. 4387–4391, 2011, doi: 10.1016/J.PROENG.2011.08.824.

[81] T. Maurizi-Enrici, "Development, metallurgical and tribological characterization of complex alloys and metal matrix composites obtained from manufacturing processes under non-equilibrium conditions," Tommaso Maurizi Enrici [Applied Science], Liège, Belgium, 2022.

[82] S.-J. L. Kang, "INITIAL STAGE SINTERING," *Sintering*, pp. 39–55, Jan. 2005, doi: 10.1016/B978-075066385-4/50004-2.

[83] H. W. Kerr, J. Cisse, and G. F. Bolling, *Acta Metall*. 1974.

[84] "Decomposition_of_Austenite_by_Diffusion".

[85] P. Franke and D. Neuschütz, "C-Si," in *Binary systems. Part 2: Elements and Binary Systems from B – C to Cr – Zr*, Berlin/Heidelberg: Springer-Verlag, pp. 1–3. doi: 10.1007/10757405_45.

[86] J. Gröbner, H. L. Lukas, and F. Aldinger, "Thermodynamic calculation of the ternary system Al-Si-C," *Calphad*, vol. 20, no. 2, pp. 247–254, Jun. 1996, doi: 10.1016/S0364-5916(96)00027-2.

[87] A. Marabi, G. Mayor, A. Burbidge, R. Wallach, and I. S. Saguy, "Assessing dissolution kinetics of powders by a single particle approach," *Chemical Engineering Journal*, vol. 139, no. 1, pp. 118–127, May 2008, doi: 10.1016/j.cej.2007.07.081.

[88] G. Lesoult, M. Castro, and J. Lacaze, "Solidification of spheroidal graphite cast irons—I. physical modelling," *Acta Materialia*, vol. 46, no. 3, pp. 983–995, Jan. 1998, doi: 10.1016/S1359-6454(97)00281-4.

[89] G. L. Rivera, R. E. Boeri, and J. A. Sikora, "Solidification of gray cast iron," *Scripta Materialia*, vol. 50, no. 3, pp. 331–335, Feb. 2004, doi: 10.1016/j.scriptamat.2003.10.019.

[90] V. Ivanov, V. Pirozhkova, and V. Lunev, "Silicon effect on the formation of graphite inclusions in gray cast iron," *Eastern-European Journal of Enterprise Technologies*, vol. 4, no. 12–88, pp. 26–30, 2017, doi: 10.15587/1729-4061.2017.107342.

[91] P. R. Howell, "T he Pearlite Reaction in Steels: Mechanisms and Crystallography Part I. From H. C. Sorby to R. F. Mehl," 1998.

[92] M. C. Rukadikar and G. P. Reddy, "Influence of chemical composition and microstructure on thermal conductivity of alloyed pearlitic flake graphite cast irons," *Journal of Materials Science*, vol. 21, no. 12, pp. 4403–4410, 1986, doi: 10.1007/BF01106563.

[93] B. Black, G. Burger, R. Logan, R. Perrin, and R. Gundlach, "Microstructure and Dimensional Stability in Si-Mo Ductile Irons for Elevated Temperature Applications," 2002. [Online]. Available: https://www.jstor.org/stable/44718728

[94] R. González-Martínez, U. de la Torre, J. Lacaze, and J. Sertucha, "Effects of high silicon contents on graphite morphology and room temperature mechanical properties of as-cast ferritic ductile cast irons. Part I – Microstructure," *Materials Science and Engineering A*, vol. 712, pp. 794–802, Jan. 2018, doi: 10.1016/j.msea.2017.11.050.

[95] M. Górny, M. Kawalec, B. Gracz, and M. Tupaj, "Influence of cooling rate on microstructure formation of si–mo ductile iron castings," *Metals (Basel)*, vol. 11, no. 10, Oct. 2021, doi: 10.3390/met11101634.

[96] M. Gó and E. Tyrała, "Effect of Cooling Rate on Microstructure and Mechanical Properties of Thin-Walled Ductile Iron Castings", doi: 10.1007/s11665-012-0233-0.

[97] R. M. German, "Prediction of sintered density for bimodal powder mixtures," *Metallurgical Transactions A*, vol. 23, no. 5, pp. 1455–1465, 1992.

[98] G. Yablokova *et al.*, "Rheological behavior of β-Ti and NiTi powders produced by atomization for SLM production of open porous orthopedic implants," *Powder Technology*, vol. 283, pp. 199–209, Oct. 2015, doi: 10.1016/J.POWTEC.2015.05.015.

[99] J. Fitzpatrick, "Powder properties in food production systems," in *Handbook of Food Powders: Processes and Properties*, Elsevier Inc., 2013, pp. 285–308. doi: 10.1533/9780857098672.2.285.

[100] G. I. Tardos, S. Mcnamara, and I. Talu, "Slow and intermediate flow of a frictional bulk powder in the Couette geometry." [Online]. Available: www.elsevier.com/locate/powtec

[101] H. Shi, G. Lumay, and S. Luding, "Stretching the limits of dynamic and quasi-static flow testing on cohesive limestone powders," *Powder Technology*, vol. 367, pp. 183–191, May 2020, doi: 10.1016/j.powtec.2020.03.036.

9. ANNEXES

Annex 1: Datasheet SiC powders

KYOCERA

STARCERAM® S UF GRADES

2021.05.17

SPECIFICATIONS

▶ Chemical formula: SiC
▶ Chemical name: Silicon carbide
▶ Description of product: Alpha Phase SiC
▶ Colour: Grey

CHEMICAL CHARACTERISTICS (TYP.) [1,2]

		UF 05	UF 10	UF 15	UF 25
C	[%]	29.50 - 30.50	29.50 - 30.50	29.00 - 30.00	28.50 - 29.50
O	[%]	max. 0.70	max. 1.10	max. 1.50	max. 2.50
Al	[%]	max. 0.03	max. 0.03	max. 0.03	max. 0.04
Ca	[%]	max. 0.01	max. 0.01	max. 0.01	max. 0.01
Fe	[%]	max. 0.05	max. 0.05	max. 0.05	max. 0.05

[1] Mass fraction in % [cg/g]; ppm [μg/g]
[2] Information on testing methods on request

PHYSICAL CHARACTERISTICS (TYP.)

		UF 05	UF 10	UF 15	UF 25
α-SiC Acheson type mainly 6 H polytype					
Specific surface area [3]	[m²/g]	4 - 6	9 - 11	14 - 16	23 - 26
Green density [4]	[g/cm³]	1.70 - 1.90	1.65 - 1.80	1.60 - 1.80	1.50 - 1.70
Particle size distribution (TYP.) [5]					
D90 %	[μm]	6.0	2.2	1.5	1.0
D50 %	[μm]	2.2	0.9	0.75	0.65
D10 %	[μm]	0.6	0.45	0.4	0.35

[3] AREAMETER II by BET DIN 66 132
[4] 10³ kg/cm²
[5] MASTERSIZER 2000 by laser light diffraction per ISO 13320, deagglomeration with high energy ultrasonic before analysis

SANDVIK

SANDVIK OSPREY LTD.,

S2 (x SLM)

osprey

RED JACKET WORKS,
MILLAND ROAD,   Telephone: 01639.634121
NEATH SA11 1NJ,   Fax: 01639.630100
UNITED KINGDOM.   E-Mail: powders.osprey@sandvik.com

CERTIFICATE OF ANALYSIS: 32344
Revision: 1

Customer:	LIEGE UNIVERSITE
Customer Order:	ULG20/1935072/R
Customer Alloy Name:	S2
Osprey Order Number:	201127/02 CALL:01
Osprey Alloy Name:	S2
Dispatch Number:	21D0265
Weight:	50.10Kg (110lb)
Powder Size:	-45micron +10micron
Atomise Gas:	Nitrogen

Physical Test Data

	Minimum	Actual	Maximum
Tap Density, g/cc		5.00	
Hall Flow, s/50g		18.0	25.0

Particle Size Data

Sieve Analysis

+45µm	1.80%
-45µm +10µm	98.20%
-10µm	0.00%

Laser Diffraction Analysis
Malvern 2000 Instrument

	Minimum	Actual	Maximum
d10 µm		20.6	
d50 µm		31.0	
d90 µm		47.5	
-10.0 µm =			%

Chemical Analysis (wt %)

El	Minimum	Actual	Maximum
Si	0.9	1.2 %	1.2
Mn	0.3	0.6 %	0.5
Mo	0.3	0.6 %	0.6
C	0.40	0.49 %	0.55
Ni	0.0	0.0	0.3
V	0.0	0.0	0.5
Fe		BALANCE	

103